UNIVERSAL RELATIONS FOR THE MASSES AND RADII OF ROTATING NEUTRON STARS

by

ANDREAS KONSTANTINOU

A thesis submitted in partial fulfillment of the requirements for the degree of

Master of Science

Department of Physics
University of Alberta

Abstract

Neutron stars are interesting due to their extremely large densities ($\sim 10^{15}$ g cm^{-3}), and also because the accretion of matter from a companion star can spin them up to very high frequencies (∼716 Hz based on observations (Hessels et al. (2006))).

When we study black holes (BH), the only thing that we have to worry about is the value of their mass, charge and angular momentum (non-hair theorem). Given these three parameters we can find all the properties that describe the black hole. On the other hand, neutron stars' properties are strongly related to the structure of the equation of state (EOS). Unfortunately, the cold nuclear matter EOS remains unknown. Therefore, the solutions of the general relativistic equations are impossible to be found without this information. Fortunately, it has been discovered that the way that some parameters are related to each other are not strongly related to the EOS choice (i.e. the relation between the normalized moment of inertia, quadrupole moment and love number). We call these relations "universal" and we can think that as a similar property as the

BH's non-hair theorem. The discovery of such universal relations can be helpful, as they can help us understand many properties of the rotating neutron stars without worrying about the structure of the EOS.

In this thesis, we provide new empirical approximations for the Kepler frequency and the spin corrections to the total mass (M), the equatorial radius (R_e) and the equatorial compactness (C_e). These relations depend on the initial compactness of a sequence (C_*) and the normalized frequency Ω_n. These corrections are universal and can describe our data very well, until the neutron stars reach approximately 95% of the Kepler frequency.

Preface

This thesis is an original work of Andreas Konstantinou, under the supervision of Dr. Sharon Morsink.

Results presented in Chapters 3, 4, and 5 will be included in a paper (under preparation) that will be submitted to a refereed journal.

"I can live with doubt and uncertainty and not knowing. I think it is much more interesting to live not knowing than to have answers that might be wrong."

Richard P. Feynman

Acknowledgements

First of all, I would like to express my sincere appreciation to Dr. **Sharon Morsink**, as without her supervision the present thesis would not be completed. Moreover, I would like to thank **Jorge Calderon Noguez** who shared with me the NSSS code and its code for the plot-creation based on the NSSS data. Also, I would like to thank the **University of Alberta Department of Physics**, the astrophysics research group, my mother **Olga Rouvim**, my father **Kostas Konstantinou**, my brother **Nikolas Konstantinou** and all of my friends who supported me during my graduate studies. Furthermore, I would like to thank **Evelyn Toumazou** who created the drawing with the springs.

Contents

List of Tables

List of Figures

Chapter 1

Introduction

Neutron stars (NS) are one of the most fascinating types of objects that exist in our universe. Their high central density (up to $10^{15} g/cm^{-3}$) is one of the characteristics that denotes their interesting structure. If you want to achieve such high densities at home, you have to uniformly distribute the mass of the Earth inside a sphere with a radius equal to the size of your neighborhood ($\sim$ 113 m). However, what my brain's neurons find really exciting is that if we want to have a better understanding of these stars, we need to use theories such as general relativity, electromagnetism, quantum mechanics etc.. Which means that we have to use almost all the theories of physics that humans have introduced. So, let's start this trip by introducing the basic background knowledge that we are going to need for this thesis.

1.1 A brief journey through a neutron star's history

Baade & Zwicky (1934), inspired by the discovery of the neutron one year before, introduced to the world for the first time the possibility of the existence of stars with small radius, but very high density. Also, they stated that supernovae are the mechanism that transforms ordinary stars into neutron stars.

Even if initially the scientific community was not convinced of the existence of such objects, there were scientists who modeled these stars. Firstly, Oppenheimer & Volkoff (1939) suggested that a NS can be modelled as an ideal gas of free neutrons. By using this assumption they also suggested that the NSs have a maximum limit on their masses and they calculated that this value is roughly 0.7 $M_{\odot}$. Today, we know that there is actually an upper limit on the mass but this is not the correct value. Why?

To understand this disagreement we have to introduce at this point the equation of state (EOS). This equation is a relation between the pressure, the density and the temperature. When the EOS of a gas is known, someone can find all the microscopic parameters that describe the system. (We are going to give a more detailed description of the NS's EOS in section 1.4). For their prediction, Oppenheimer & Volkoff (1939) assumed that the neutrons do not interact with each other and they also assumed that even if they do, this interaction is not going to change their results. However, Cameron (1959) showed that we can not neglect the nuclear forces as they actually lead to a more stiff EOS. The term "stiff EOS" means that the pressure at a given density is relatively large compared to the other EOS models. A soft EOS corresponds to the opposite case. Also, it is known that a stiff EOS predicts a larger maximum mass value compared to a soft EOS. As a result, we expect that in reality the maximum mass limit takes place somewhere between 2 $M_{\odot}$ and 3 $M_{\odot}$ (Haensel et al. (2007)).

Later research by Zeldovich (1961), suggested that the core of a NS is not as simple as it was previously expected. In the center of these stars, beyond the existence of electrons, protons and neutrons, we can find muons, mesons, and/or hyperons.

The discovery of the first pulsar by Bell[1] in 1967 led to the general acceptance by the scientific community that neutron stars exist. After more than half a century of observations with telescopes at all wavelengths we are now gaining a better understanding of neutron stars.

[1]February 1968: The Discovery of Pulsars Announced `https://www.aps.org/publications/apsnews/200602/history.cfm`

1.2 Neutron star evolution

A NS is created during a supernova explosion. This happens at the end of a massive star's "life". After the explosion (Foglizzo et al. (2015), Prakash et al. (2000)), the stellar envelope is removed and the remnant is a proto-neutron star (PNS). There are two possible ways that the PNS will evolve: a) either it is going to cool and form a neutron star, b) or its mass is going to exceed the upper limit and contract to a black hole. Here, we are going to focus only on the first case.

Once the core of the massive star collapses (Foglizzo et al. (2015)) inward, the material in the core is compressed to high densities allowing for protons and electrons to combine into neutrons and neutrinos:

$$p + e^{-} \longrightarrow n + \nu_e. \tag{1.2.1}$$

These neutrinos are trapped inside the core and only after the supernova explosion do they escape from the star (Janka (2017)) carrying away energy making the PNS cool down, forming a smaller NS with a temperature somewhere between $10^5 K$ - $10^6 K$ which is much less than the Fermi temperature ($\sim 10^{11}$ K). A typical NS is expected to have a mass equal to 1.4 $M_\odot$ and a radius $\approx$ 12 km.

At the center of the core the value of the density is 3 to 9 times larger than the nuclear saturation density $\rho_0 = 2.28 \times 10^{14}$ g cm^{-3} (the density of an atomic nucleus). Therefore, we expect that exotic matter could be formed and the EOS will become softer.

In the next section we are going to take a look at the NS's "anatomy". The internal structure of these stars can provide us with more information about the evolution and the fundamental laws that govern the system.

1.3 The internal structure

The combination of high densities and cool temperatures found in neutron stars are unique in the Universe. Nowhere else in the Universe does the density change from $\sim 10^4$ g cm^{-3} to $\sim 10^{15}$ g cm^{-3} within 10 km.

You can imagine NSs as onions. Their structure is composed of a number of layers (Kutschera (1998)), and they can make you cry if you spend enough time with them. Each layer has different properties depending on its density (see Figure 1.3.1), so in this section we are going to describe the layers from the least dense outer layers to the densest inner regions.

1.3.1 The atmosphere

For an isolated NS the outermost layer is a very thin atmosphere (scale height $\sim$ 10 cm) (Zavlin & Pavlov (2002), Haensel et al. (2007)). To be more specific, the atmosphere is actually a slim plasma envelope and it can be the source of thermal electromagnetic radiation. The atmosphere of the isolated star is mainly composed of heavy elements, such as iron for example.

For a NS in a binary system its composition depends on the accretion history of the star. In the case where accretion took place in the past, we can have a Hydrogen or Helium atmosphere (in the case where the donor was a He white dwarf). This is a result of the gravitational settling which makes the lightest elements that have been accreted to rise quickly to the top of the atmosphere (Brown & Bildsten (1998)).

1.3.2 The outer crust

From the bottom of the atmosphere and until the density goes up to roughly 4×10^{11} g cm^{-3}, we can find the outer crust (Baym et al. (1971)) which is composed of nuclei and free electrons. To be more specific, below $\sim 10^4$ g cm^{-3} we have mainly Iron nuclei. These nuclei were produced by the nuclear fusion process that took place in the massive star before the SN explosion. The

Coulomb force is significant enough that a Coulomb lattice is created (this is why we call it a crust).

The electrons in the cool NSs are degenerate, as the temperature of the system is much less than their Fermi temperature. This means that the number density is going to be proportional to p_F^3, where p_F is the Fermi momentum. As a result, the momentum of the electrons will increase as the density does. Therefore, we expect that at densities larger than $\sim 10^7$ g cm^{-3} the electrons will become fully relativistic. As a consequence the electrons are going to have enough energy that they can combine with protons in the nuclei to produce neutron-rich nuclei. When the density increases up to $\sim 10^{11}$ g cm^{-3} the neutrons can exist outside of nuclei. This effect is known as neutron drip.

1.3.3 The inner crust

The inner crust (Baym et al. (1971)) is the region with densities ranging from $\sim 10^{11}$ to $\sim 10^{14}$ g cm^{-3}. As the density becomes larger than 10^{11} g cm^{-3} neutron drip takes place. This means that some neutrons get free from their nuclei. Therefore the inner crust is composed of a free electron and neutron gas which coexists with the Coulomb lattice. As we pass 10^{14} g cm^{-3} no more nuclei can be found in the NS and the core of the NS begins after this point.

1.3.4 The outer core

The core is separated into two parts. The outer core and the inner core. The outer core starts when the density is $\approx 1 \times 10^{14}$ g cm^{-3} and goes up to the point where the density is $\approx 4.5 \times 10^{14}$ g cm^{-3} (Haensel et al. (2007)). Its composition is more complicated than the outer layers. The nuclear interaction among neutrons and protons begins to affect the system, so they act as a superfluid-Fermi liquid. Also, the electron and muon (μ) gases obey the equations that describe the ideal Fermi gases.

The existence of protons, neutrons and electrons in the outer core makes sense, since these are the particles that exist in an atom. The question now is

"where do the muons came from?". To answer this question we have to go back in time (a short time after the supernova explosion). When the NS cools down to $\sim 1 \times 10^{10} K$, the energy of the nucleons (neutrons or protons, denoted N) is high enough to lead to strong reactions producing hadrons with strange quarks such kaons, K and lambdas Λ

$$N + N \longrightarrow N + \Lambda + K. \tag{1.3.1}$$

The Λ is an example of a Hyperon, which is a baryon containing a strange quark, and will be discussed in more detail in the next section. The kaons, which are mesons that include one strange quark, could decay as follows

$$\begin{aligned} K^0 &\longrightarrow 2\gamma, \\ K^- &\longrightarrow \mu^- + \overline{\nu}, \\ \mu^- + K^- \longrightarrow \mu^- + \mu^+ + \nu &\longrightarrow 2\gamma + \nu. \end{aligned} \tag{1.3.2}$$

The photons (γ) and neutrinos (ν) will escape from the system leading to a further decrease of the temperature. This process is going to stop when the energy of the system becomes less than the critical energy where Kaons are able to be created (or in other words, strong reactions can not take place any more). After this point hyperons can be produced by weak interactions, until the system reaches equilibrium (Glendenning (1997)).

1.3.5 The inner core

The densest region of the neutron star is called the inner core and is the area where the density becomes larger than 4.5×10^{14} g cm^{-3}. Although many models give some hypothetical composition for this region, its real structure remains unknown. The contents of this mysterious region might be some other exotic matter (such as new fermions or bosons). (Haensel et al. (2007))

The inner core is a region in the NS that is not fully understood yet. For this reason, I believe it would be a good idea to say a few things more, as it is an area that might lead to the discovery of new laws of physics. Keep in mind that

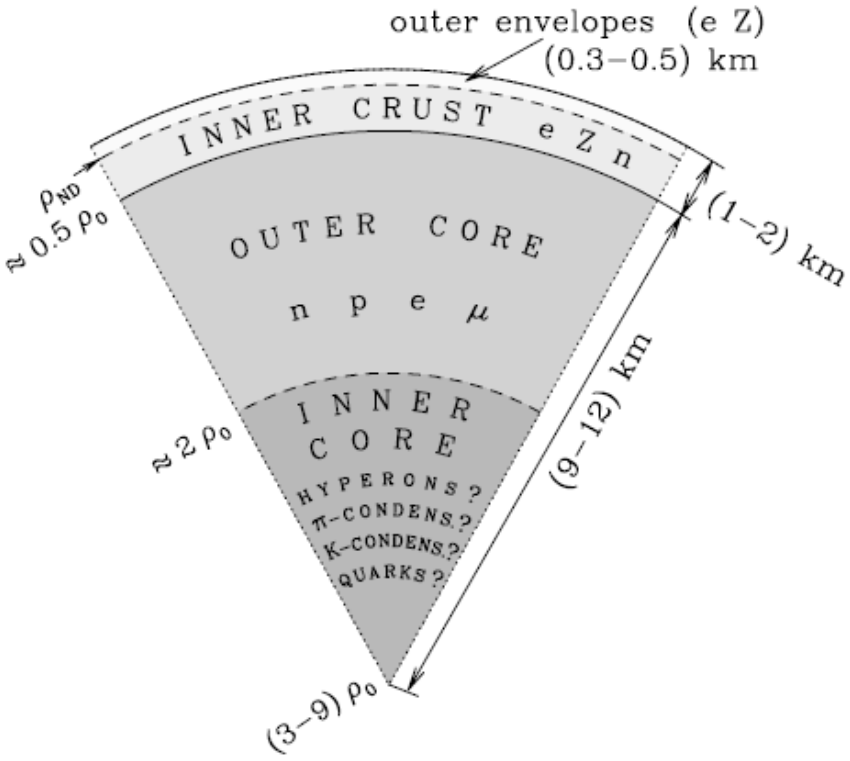

FIGURE 1.3.1: Internal structure of a neutron star ($\rho_0 = 2.28 \times 10^{14}$ g cm^{-3}). This figure is an original work of Haensel et al. (2007)

all the following subsections are hypothetical scenarios and not experimentally proved theories.

1.3.5.1 Hyperons

In the case where the inner core's density takes a value between 2-3 ρ_0, hyperons could be formed (suggested by Ambartsumyan & Saakyan (1960) for the first time). The rate that NS cools can be affected by the existence of these particles. Furthermore, the creation of hyperons leads to the decrease of the nucleons' number and as a consequence the Fermi pressure will decrease, leading to a softer EOS. As a result, the upper limit of the mass decreases. Unfortunately, the predicted maximum mass value disagrees with the mass measurements determined through radio observations of pulsars. In order to find a solution for this problem, physicists are trying to create models that could

stiffen the EOS and lead to an agreement of theory with observations. This will happen if for some reason we have extra repulsive forces in the system. More details about the models that provide this extra repulsive force in the existence of hyperons can be found in Vidaña (2016).

1.3.5.2 Hybrid and Quark stars

Another possible description of the neutron star's inner core might come from a better understanding of the quark matter at such high densities. It is believed that at such extreme environments (the core of the NS) quark matter may exist (Burgio et al. (2002)), and as a first approximation the quarks could move as free particles (Witten (1984)).

This is why some people believe that neutron stars are in reality hybrid stars. By the term hybrid stars, we define the stars that are composed of a stiff quark matter core, and by nuclear matter at the low density region. The stiffness of the core comes from the repulsive forces among the quarks (Zdunik & Haensel (2013)). It is difficult to model the crossover from nuclear matter to quark matter inside these stars. In some cases, simple assumptions are used in order to model them, as for example the continuity of the pressure, the baryon number density and the susceptibility (Kojo et al. (2021)). Also, we can force these parameters to match the boundary conditions at the regions where we have pure quark matter and pure nuclear matter.

Another hypothesis is that bare quark stars without a hadronic crust could exist in nature (Alcock et al. (1986)). Quark stars can work as laboratories for the study of the cold quark matter. However, for this thesis we are not going to get into a more detailed description of quark stars, since our main goal is the study of NSs.

1.4 Equation of state (EOS)

For our research we assume that enough time has passed after the supernova explosion, allowing the neutron star to quickly cool down due to neutrino and

photon emission. In this case the temperature falls below the Fermi temperature. This means that the EOS is temperature independent and an equation that relates the pressure with the energy density is sufficient for us to solve the problem. Observations place some constraints on the cold EOS, but there is still a wide range of possible EOSs. Even the theoretical definition of the EOS is still unknown due to the difficulty of many-body quantum chromodynamics calculations.

The EOS is strongly related to the interior structure of the NSs. So, we can understand that despite the fact that the mathematical prediction of the EOS is not simple at all, it is essential for someone in order to model a NS. This comes from the fact that the Tolman-Oppenheimer-Volkoff (TOV) equations are two equations with three unknown functions that depend on the value of the radial distance (coordinate mass (m), pressure (P) and energy density (ϵ)). Therefore, in order to solve this problem and find the Mass - Radius relation we need a third equation that relates two of these four parameters. This is why the EOS is so important (Özel & Freire (2016)). We are going to talk more about the TOV equations in the next chapter.

1.4.1 Finding the EOS

Despite our difficulty to solve the QCD equations that describe the cold nuclear matter, many hypothetical models have been created and many scientists are trying to find the EOS which is closer to reality. For example, figure 1.4.1 shows a variety of EOS models. The x-axis takes values from 0.1 ρ_0 to 8 ρ_0.

Figure 1.4.2 shows the Mass-Radius relations for some of the models that are included in the first plot. The grey curves in Figure 1.4.2 represent the models that can not exceed the 2 $M_\odot$ limit. It can be seen that the maximum mass value varies as it depends on the structure of the NS.

Also, the majority of these models predict that in the case where a significant amount of mass is added into the system, the change of the radius is very small (which can be seen as the vertical part of the Mass-Radius curves shown in Figure 1.4.2). This comes from the fact that at this point the density at the

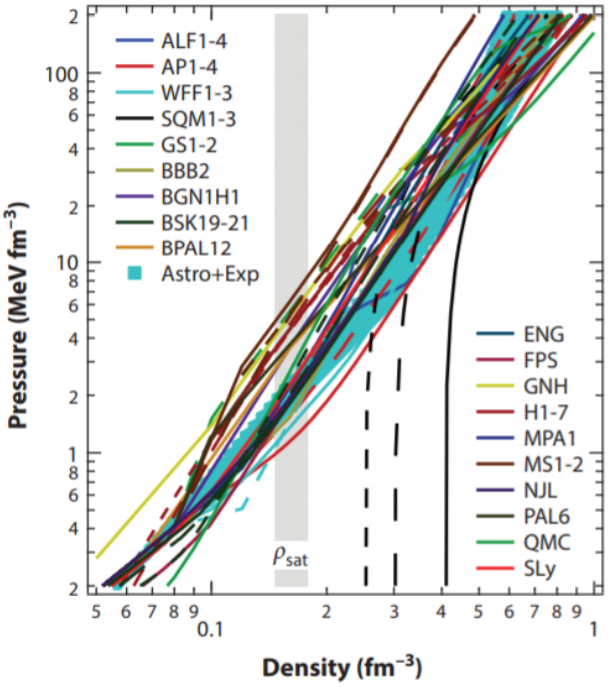

FIGURE 1.4.1: Pressure vs density for different EOSs This figure is an original work of Özel & Freire (2016).

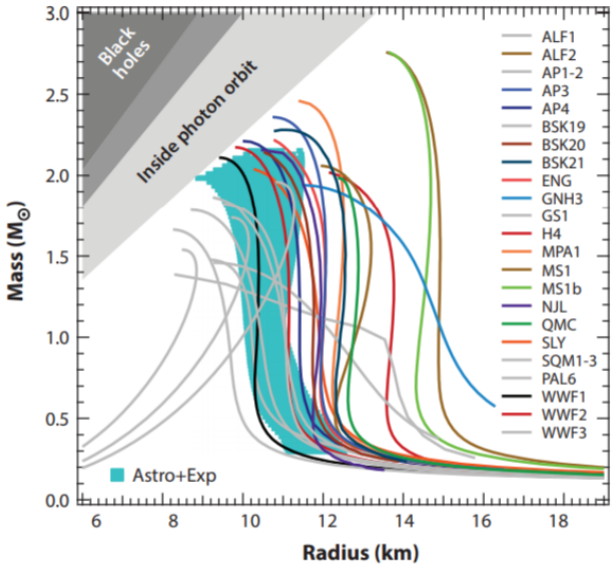

FIGURE 1.4.2: Mass - Radius curves for different EOSs This figure is an original work of Özel & Freire (2016).

center is larger than the saturation density. As a result, the pressure from the nuclear repulsion can balance the additional gravitational force and this leads to

a very small change to the radius. On the other hand, at the "tail" of the Mass-Radius curve (small mass and large radius), the density at the center is less than the saturation density. This means that we don't have this extra pressure, and by adding more mass into the system the radius changes significantly. There is no known mechanism for forming NS with masses < 1 Msun. However, very low mass stars are included on this diagram since a theoretical prediction of the structure is still possible.

Furthermore, it is worth mentioning that the quark star (labelled SQM (Strange Quark Matter)) models have a counter-intuitive structure, since their radius increases as their mass is getting larger. This comes from the fact that these EOSs are "self-bound", which means that the pressure vanishes at a finite density. This is going to change the behavior of the TOV solution as it can be seen in the Figure 1.4.2 (Özel & Freire (2016)).

The blue area shows our expectations based on the observations and experiments (Özel & Freire (2016)).

1.5 Pulsars

Pulsars are magnetized spinning neutrons stars, that emit electromagnetic radiation from their magnetic poles. This radiation is detected as a pulse once every spin period when the radiation beam intersects our line of sight. Observations of these pulses of radiation give very precise measurements of the spin periods of pulsars. At present we have 3319 pulsars recorded in the catalogue of the Australia Telescope National Faculty (ATNF)[2], from which the 530 are millisecond pulsars[3]. White dwarf can be also pulsars, but in this thesis we will only consider NS pulsars (Marsh et al. (2016)).

Pulsations are seen in energy bands ranging from gamma-rays to radio. Using our telescopes, pulsar spin periods and period derivatives are measured precisely. Pulsars that are not accreting matter from a companion have negative intrinsic period derivative. This means that their spin decreases as the time

[2]ATNF Pulsar Catalogue `https://www.atnf.csiro.au/research/pulsar/psrcat/`

[3]Millisecond Pulsar Catalog `https://blacksidus.com/millisecond-pulsar-catalogue/#Millisecond_Pulsar_Catalog`

passes, due to the emission of magnetic dipole radiation. It is very important to point out that the pulses of these old and cold neutron stars are incredibly stable. Such stable pulses can be described by the assumption that the angular velocity is uniform within the star. For this reason in the present thesis we are going to assume rigid rotation. Even if it is believed that differential rotation characterizes systems such as the proto-neutron stars and the remnants of NS binary mergers (Morrison et al. (2004)), the study of these systems is beyond the goal of this thesis. It is worth mentioning that differential rotation can make the mass of a rotating neutron star to increase up to 1.5 times of its maximum static mass (these stars are called hypermassive NSs (Kaplan et al. (2014))).

The magnitude of the electric field in the magnetosphere is so high that it attracts electrons from the atmosphere of the pulsar and fills the magnetosphere with plasma.

Two important regions outside of a neutron star are the light cylinder radius and the corotation zone. The light cylinder is located at a distance that is equal to $cP/(2\pi)$, where P is the spin period of the star. On object that rotates around the star with the star's spin period will travel at the speed of light. The co-rotation zone, is the region between the light cylinder radius and the pulsar's surface. (Haensel et al. (2007))

1.5.1 Pulsar masses

The detection of pulsars that are a member of a binary system is very important, since their mass values can be used in order to place restrictions to the neutron stars' EOS. For compact stars in a binary system, their masses can be calculated by using the post-Keplerian equations, which are the Kepler's equations with the consideration of the small general relativistic effects.

Such an example is the binary pulsar PSR B1913+16. The mass of these two neutron stars has been calculated by using Hulse & Taylor (1975) measurements of the binary period P_b and the high orbital period eccentricity e, the Taylor et al. (1979) measurements of the orbital period decay $\dot{P}_b$ and the "Einstein delay" γ and the post-Keplerian equations (more about the post-Keplerian

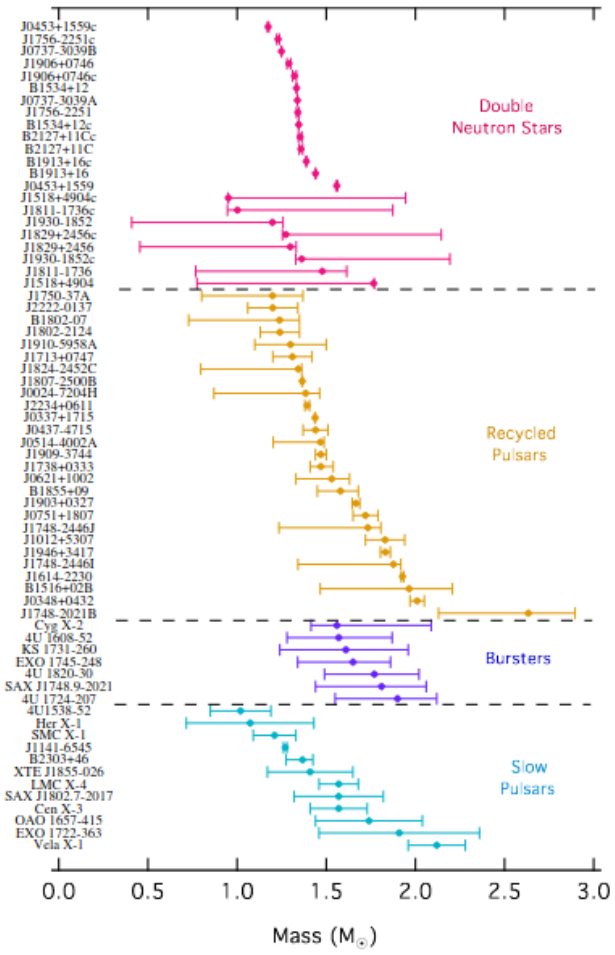

FIGURE 1.5.1: Neutron stars mass measurements. This figure is an original work of Özel & Freire (2016).

equations and these parameters can be found in section 2 of Özel & Freire (2016)). In the case where the NS has a non-compact star as a companion, then Kepler's law without relativistic corrections can be used.

1.6 Evolution of neutron stars and pulsars in a binary system

As the main goal of this thesis is the study of rapidly rotating NSs, we are going to focus on a type of binary system called a Low Mass X-ray Binary, which is where neutron stars are spun up to rapid rotation rates. There is still some uncertainty about the details of how a binary system evolves into a LMXB, which could include complications such as common envelope events (Nelson & Rappaport (2003)). One possible evolutionary scenario is a binary system with a massive star (the primary) and a lower-mass star (the secondary). It is well known that more massive stars evolve faster than those with smaller mass. The primary will evolve, expand, and eventually explode in a supernova, producing a neutron star. If the supernova does not disrupt the binary system, a binary system composed of a neutron star and another star will result.

Eventually the secondary star will evolve. Depending on the orbit and the secondary star's mass, when the secondary evolves into a giant, it can overflow its Roche lobe, sending material to the neutron star. For the LMXB the star 1 is a NS and the star 2 is a white dwarf (Börner, G. (1978)).

This is just a brief explanation for the binary system "behavior", but let's comment a little bit more on the period when the second mass transfer happens. It is known that after this phase we could have a pulsar that spins with a frequency larger than 100 Hz. This is what we define as a **millisecond pulsar**. The mass that is transferred from the one star to the other can also transfer angular momentum. This is going to spin-up or spin-down the NS. The accreted mass stops at the magnetospheric radius and matter is going to be transmitted if this radius is smaller than the light-cylinder and the corotation radius (accretion phase). This will increase the spin frequency and the corotation radius will become smaller.

On the other hand, if the magnetic radius is larger than the corotation radius but smaller than the light-cylinder radius the accretor will not gain mass. Instead, it is going to lose angular momentum (propeler phase). So now, the spin frequency decreases and the corotation radius will become larger. As

a result, after some time the magnetic and the corotation radius become equal and the NS spins with a characteristic equilibrium frequency (Bhattacharyya (2021)), which can be on the order of 100's of Hz. This is one example of how a millisecond pulsar can be created.

1.7 Looking into the sky for neutron stars

Personally, I believe that theoretical physics have a wonderful way making our brains travel along the universe. However, no theory is valid until the observations say so. For this reason, in this section we are going to make a brief tour to the observational astronomy of the past, the present and the future.

1.7.1 The past

The detection of the X-ray emission from Sco X-1 and Cyg X-2 (Giacconi et al. (1964)) was the first indirect clue that a star can accrete mass from its companion. This observation changed the way that X-ray astronomers understand nature. The next step that helped us to understand that in a binary system, one of the stars can be a NS, was the observation of the Cen X-3 (Giacconi et al. (1971)). In this observation the signal was generated by a NS with a large-magnitude magnetic field, that accreted mass from a companion star Santangelo et al. (1998). This NS, spins with a period of 4.8 s and orbits with its companion with a period of 2.1 days. As a result, the signal had delays and by some of its characteristics, scientists understood that the companion was a massive star. This is an example of what is called a high-mass X-ray binary (HMXB). With the same logic, the low-mass X-Ray binaries (LMXB) are the systems with a low mass companion. However, the observation of the orbital period of LMXBs was not as simple as for the HMXBs (J.E Ventura (1991)). So, the use of modern telescopes was essential for the detection of more LMXBs.

1.7.2 The present

As the technology evolves, larger telescopes are available and their use makes the detection of the NSs much easier. The telescope listed in this section observe the X-Ray spectrum. The reason that we are interested in X-rays is that the energy emitted from the surface of a NS has a range from 100 eV to 100 keV (X-Rays).

An example is the **NICER** (Neutron-star Interior Composition ExploreR) (Gendreau et al. (2016)) telescope which accurately measures the arrival times and energies of X-ray photons emitted from the surfaces of NS (and other high energy emission sources). The gravity of the NS acts like a lens and changes the direction of a light beam that is emitted from the NS's surface. From the properties of the pulsed x-rays, we can infer the bending of the light and the mass and the radius of the star (Bogdanov et al. (2019), Riley et al. (2019), Miller et al. (2019)).

The **NuStar** (Nuclear Spectroscopic Telescope Array) (Harrison et al. (2013), Tsuji et al. (2019)) looks for high energetic events (3 - 78 keV) for example, the observation of a young pulsar associated with the gamma-ray source HESS J1640-465, located in a supernova remnant (Gotthelf et al. (2014)).

Chandra's (Weisskopf et al. (2000)) specialty is imaging X-rays as well as spectroscopy. Also, is very useful for the study of X-Ray emitters such as the observation of the millisecond pulsar PSR B1821-24 (Becker et al. (2004)). Chandra observations have been used to measure the emitting areas of a few neutron stars, leading to some constraints on their masses and radii (Heinke et al. (2014)).

XMM-Newton (Jansen et al. (2001)) observes energies from 0.15keV to 12 keV and is the largest European telescope. XMM is at present the best X-ray telescope for X-ray spectroscopy, and also has the ability to time the arrivals of photons, although not with the accuracy of NICER. XMM observations were used to place the earliest constraints on the mass and radius of PSR J0437–4715 (Bogdanov (2012)), which will be improved by NICER observations soon.

1.7.3 The future

These are the telescopes that we use at present and they take the place of our past equipment (for example EINSTEIN and ROSAT telescopes). Similarly, we expect that eXTP, STROBE-X and ATHENA are going to replace these ones and open the door to new discoveries.

eXTP[4] , which its initials stand for "enhanced X-ray Timing and Polarimetry", is expected to be launched in 2027. The main goal of the mission is the observation of the effects that are caused by extremely high magnetic fields, gravitational fields and densities. Its equipment is going to allow scientists to detect phenomena that could happen in energies from 0.5 keV to higher than 30 keV, with timing resolution similar to NICER, but better spectral resolution and collecting area.

We expect that **STROBE-X**[5] is going to observe within a similar energy range as the eXTP (0.2 - 30 keV). The mission is expected to start after 2030. Not only it is going be used for the study of NSs, BHs and their accretion disks. It is expected that both STROBE-X and eXTP will measure the masses and radii of many neutron stars with much better precision than is possible with NICER Ray et al. (2019).

ATHENA (Advanced Telescope for High ENergy Astrophysics) [6] is an X-ray telescope which is expected to be launched in the early 2030s. As its name says, the purpose of this telescope is to be used for the observation of high energetic astrophysical phenomena. This telescope is going to be useful for the study of compact stars' accretion phase. The development of such telescope is important as their equipment is going to provide a high effective area and a high spectral resolution.

[4]The eXTP Mission `https://www.isdc.unige.ch/extp`

[5]STROBE-X Mission Overview `https://gammaray.nsstc.nasa.gov/Strobe-X`

[6]Advanced Telescope for High Energy Astrophysics`https://www.the-athena-x-ray-observatory.eu/`

1.8 The thesis goal

The goal of this thesis is to computationally study the equations governing the change of the mass and radius due to the star's spin frequency. We achieve this by computing sequences of rigidly rotating NSs with constant central energy density. The motivation is to find a way to improve the accuracy of the EOS inference methods given mass and radius measurements of rotating neutron stars.

There is no consensus on the correct EOS of cold matter at densities above saturation. In our calculations, we require an EOS in order to solve the stellar structure equations. In order to allow for a wide range of physics, we created two sets of random EOS that are allowed by current astronomical observations and nuclear theory. The first one is based on the assumption that the core can be approximated as a piecewise polytrope (Read et al. (2009), Hebeler et al. (2013)). The second one is based on the assumption that the square of the speed of sound has a gaussian behavior, and approaches $\frac{c^2}{3}$ from below at very high densities (Greif et al. (2019)). By using the two EOS families we expect to obtain a realistic range of possible values of mass, radius, and spin and correctly model the way that these parameters are related to each other.

We used these two sets of EOSs to create sequences of rotating NSs with constant central energy density. The first star in each sequence is a non-rotating NS and the last one is a NS with a frequency a little bit smaller than the Kepler frequency (the limit where the centrifugal force becomes larger than the gravitational force at the surface) or the point where the star becomes unstable to quasi-radial perturbations. These sequences are created by the use of the RNS code (Stergioulas & Friedman (1995)). This code calculates all the macroscopic parameters that describe a NS for a given EOS, central density and ellipticity. Such macroscopic parameters include the total mass (M in $M_\odot$), the equatorial radius (R_e in km) and the frequency of the star (Ω in Hz). Also, the notation for the mass and the radius of the first non-rotating NS in a sequence is M_* and R_* respectively.

The main outcomes of this thesis are: (a) a new approximation for the Kepler frequency, that is used for the frequency normalization. (b) New empirical

approximations for the total mass, the equatorial radius, and the compactness for rapidly rotating neutron stars that only depend on the properties of non-rotating neutron stars with the same central density. Our equation for the equatorial radius deviates from the data by less than 1.5% when the frequency is less than the 98% of the Kepler frequency, and the mass deviation is less than 4.6% in general. These two equations are independent of the EOS properties and therefore they are universal. By using these two best-fit equations we can calculate the mass and the equatorial radius values of the rotating stars up to 95% Ω_K, much faster than the RNS code does. This provides a computationally-inexpensive method for including corrections due to rotation in EOS-inference codes which may require computing many hundreds of thousands of different neutron star models. (c) For frequencies larger than 95% Ω_K our best fit equations (in part (b)) are not accurate enough. For this reason we provide two empirical approximations for the mass and the equatorial radius changes at the Kepler limit. We use these approximations to construct the Mass-Radius curve for the stars that spin with the Kepler frequency. (d) Finally, we investigated the inverse process in order to construct a mapping from rotating neutron stars to equivalent non-rotating neutron stars with the same central density. We did that in order to find the non-rotating NS with the same central energy density for given values of Ω, M and R_e of a rotating NS. In the future, when telescopes with larger collection area are able to measure the radii and masses of rapidly rotating neutron stars more precisely, it will be possible to use these best-fit equations to recreate the Mass-Radius curve of non-rotating NS.

1.9 What follows

This thesis is organized as follows. Initially, in Chapter 2 we are going to introduce the basic equations of general relativity that are required to compute the structure of rotating neutron stars assuming hydrostatic equilibrium. This chapter includes a review of some of the macroscopic properties of neutron stars and some empirical approximations developed by previous authors. Chapter 3 introduces the computer code and numerical methods used to compute the random EOS families and to solve the equations of relativistic stellar structure. In Chapter 4, we are going to give the empirical equations for the mass, equatorial

radius and compactness changes. Also, we provide some useful applications for them and a path for further research in the future. In Chapter 5, we provide a possible explanation for our results. Finally, in Chapter 6 we are going to conclude with a discussion of these results.

Chapter 2

General relativity in neutron stars

In the Newtonian limit and in the absence of mass, Euclidean geometry is used to describe the 3D geometry of the Universe. However, special and general relativity take place in a 3+1 dimensional world. Here, "3" stands for the 3 space dimensions and "1" stands for the time dimension. In order to describe the empty and flat space-time we must use the Minkowski metric. In spherical coordinates the metric is given as follows

$$ds^2 = -c^2dt^2 + dr^2 + r^2(d\theta^2 + sin^2\theta d\varphi^2). \tag{2.0.1}$$

Here the negative sign separates the time parameter from the space parameters.

However, we know that in the existence of mass, space-time is going to be curved. For systems with high densities, general relativistic effects play an important role (i.e. gravitational wave emission, curved photon paths and gravitational red-shift). Hence, Newtonian theory can not be accurate anymore and we must use the general relativistic (GR) equations in order to make predictions.

In general, $x_g = r_g/R$ is the parameter that denotes the importance of the GR corrections. Here r_g is the Schwarzschild radius and is equal to $2GM/c^2$. Newtonian equations are accurate at the limit where $x_g << 1$. If a star with mass M has a radius smaller than r_g, this means that the photons that are at a radial distance less than r_g can not escape and therefore this object is a BH. In this case the r_g is the event horizon of the BH. (Potekhin (2010))

In this chapter, we are going to see how the space-time is curved in the existence of mass, give a brief overview of these effects and take a look at the GR equations needed to solve in order to model the rotating NSs.

2.1 Perfect fluid

It has been mentioned earlier that some parts of the NS's interior act as a perfect (or super) fluid. But what does this mean? Theoretically, if we could have a perfect fluid in a bowl and stir it, the fluid would rotate forever. This happens because there is no friction among the particles (no viscosity) and no heat losses (no heat conduction). Although neutron star matter does have viscosity and finite thermal conductivity, these aspects do not affect the large scale properties such as the neutron star's mass and radius.

The energy-momentum tensor for a perfect fluid in the absence of gravity is (the equations in this section come from chapter 4 in Schutz (2009))

$$T^{\mu\nu} = (\epsilon + P)u^{\mu}u^{\nu} + P\eta^{\mu\nu}, \tag{2.1.1}$$

where u^{μ} is the four-vector velocity, ϵ is the energy density, P is the pressure and $\eta^{\mu\nu}$ is the Minkowski metric

$$\eta_{\mu\nu} = \begin{pmatrix} -c^2 & 0 & 0 & 0 \\ 0 & 1 & 0 & 0 \\ 0 & 0 & r^2 & 0 \\ 0 & 0 & 0 & r^2 sin(\theta) \end{pmatrix}. \tag{2.1.2}$$

Note that P and ϵ could depend on all 4 coordinates (t, r, θ, ϕ).
The equation of the energy conservation $T^{\mu\nu}_{,\nu} = 0$, provides relations between the energy density, the pressure and the number density (n). In the rest frame of the particles, the time component of the conservation equation is

$$\frac{d\epsilon}{d\tau} - \frac{\epsilon + P}{n}\frac{dn}{d\tau} = 0. \tag{2.1.3}$$

The spatial components (denoted with the index "i") give the equations

$$(\epsilon + P)\alpha_i + P_{,i} = 0, \tag{2.1.4}$$

where α_i is the i^{th} component of the four-acceleration vector. This is very similar to the non-relativistic limit where $\rho\vec{a}+\nabla P = 0$, but now we have $(\epsilon+P)$ instead of ρ.
In the next section we are going to show how this concept changes in the existence of gravity.

2.2 General relativistic equations for a spherical symmetric star

In the existence of matter, space-time is going to curve. So, in the case where we have a spherical symmetric mass (or energy) distribution, the Minkowski metric will be replaced by (the equations in this section come from chapter 10 of Schutz (2009))

$$ds^2 = -e^{2\Phi(r)}c^2dt^2 + e^{2\Lambda(r)}dr^2 + r^2(d\theta^2 + sin^2\theta d\varphi^2). \tag{2.2.1}$$

Φ(r) and Λ(r) are called the metric potentials and depend on the distance from the axis origin r. $\Phi(r)$ is the quantity that reduces to the gravitational field in the Newtonian limit and $\Lambda(r)$ is related to the curvature of the space along the radial direction. Also, at the limit where both functions are 0 we have again the Minkowski metric.
The distance between two different points along the radial direction (where dt = dθ = dϕ = 0) is given by

$$l_{12} = \int_{r_2}^{r_1} e^{\Lambda(r)}dr. \tag{2.2.2}$$

Using the metric equation, the energy-momentum tensor of a perfect fluid in the existence of gravity

$$T^{\mu\nu} = (\epsilon(r) + P(r))u^{\mu}u^{\nu} + P(r)g^{\mu\nu}. \tag{2.2.3}$$

Here instead of the $\eta^{\mu\nu}$, we used $g^{\mu\nu}$ which is the metric in the existence of gravity (2.2.1)

$$g_{\mu\nu} = \begin{pmatrix} -e^{2\Phi(r)}c^2 & 0 & 0 & 0 \\ 0 & e^{2\Lambda(r)} & 0 & 0 \\ 0 & 0 & r^2 & 0 \\ 0 & 0 & 0 & r^2 sin(\theta) \end{pmatrix} \tag{2.2.4}$$

By using the conservation law $T^{\mu\nu}_{;\nu} = 0$, we can find out that

$$(\epsilon(r) + P(r))\frac{d\Phi(r)}{dr} = -\frac{dP(r)}{dr}. \tag{2.2.5}$$

This equation is the relativistic generalization of the equation of hydrostatic equilibrium. The solution of this equation shows how pressure must change with the radius, so a fluid can remain static in the existence of gravity.

Furthermore, from the Einstein field equations (see chapter 10 in Schutz (2009)) we can extract the Newtonian-like mass gradient

$$\frac{dm(r)}{dr} = 4\pi r^2 \epsilon(r)/c^2, \tag{2.2.6}$$

where in the GR case we use $\epsilon(r)$ instead of $\rho(r)$.

From the Einstein field equations we can take also that

$$\frac{d\Phi(r)}{dr} = \frac{G(m(r) + 4\pi r^3 P(r)/c^2)}{rc^2[r - 2Gm(r)/c^2]}. \tag{2.2.7}$$

It can be seen that we have 4 unknown functions but only 3 equations. For a given EOS we can find how the pressure changes with respect to the energy density. Therefore, if we know the EOS, the problem reduces to 3 unknown functions. This means that we can use the three equations above in order to find the pressure, the gravitational potential and the mass coordinate as a function of the radial distance.

We can use these equations to describe the region outside the star (when r>R, where R is the outer radius of the star), if we just set $\epsilon(r)$ and P(r) to zero. As a result, we get the Schwarzschild metric,

$$ds^2 = -(1 - \frac{2MG}{rc^2})c^2dt^2 + (1 - \frac{2MG}{rc^2})^{-1}dr^2 + r^2(d\theta^2 + sin^2\theta d\varphi^2). \quad (2.2.8)$$

Birkhoff's theorem proves that there is no other solution for Einstein's equations in a spherically symmetric space-time. As a result, independently of the interior properties, if spherical symmetry is satisfied, the gravitational field of the space-time outside the star can be described by Schwarzschild's metric.

On the other hand, inside the star $\epsilon(r)$ and P(r) are not zero. So, by using equations 2.2.5 and 2.2.7 we can get the Tolman–Oppenheimer–Volkov (TOV) equation

$$\frac{dP(r)}{dr} = -\frac{G(\epsilon(r) + P(r))(m(r) + 4\pi r^3 P(r)/c^2)}{rc^2[r - 2Gm(r)/c^2]}. \quad (2.2.9)$$

By using equations 2.2.6 and 5.2.7, the EOS, and a value for the central energy density, the equations can be integrated outwards until the radius R, where the pressure vanishes. This procedure yields the star's total mass and outer radius. This procedure can be repeated for all possible central densities, giving the mass-radius curve for the EOS.

2.2.1 Relativistic enthalpy

You might already know that enthalpy is defined as H = E + PV. Here we are going to talk about relativistic enthalpy (N), which is a quantity that hasn't been introduced yet.

If we go back to equation 2.2.5 we can define a new quantity as follows

$$dN(r) = \frac{1}{\epsilon(r) + P(r)}dP(r). \quad (2.2.10)$$

So, equation 2.2.5 becomes

$$\frac{d\Phi(r)}{dr} + \frac{1}{c^2}\frac{dN(r)}{dr} = 0. \tag{2.2.11}$$

Therefore, $\Phi(r)c^2 + N(r) =$ constant. The parameter N(r) vanishes on the surface of the star, so in the case of a spherical symmetric non-rotating NS we can find that

$$c^2\Phi(r) + N(r) = \frac{c^2}{2}\ln\left(1 - \frac{2M}{R}\right). \tag{2.2.12}$$

This quantity is very useful, as we can use it to find the gravitational potential inside the star. Also, we can rewrite the hydrostatic equilibrium equation as

$$\frac{dN(r)}{dr} = -\frac{G(m(r) + 4\pi r^3 P/c^2)}{rc^2(r - 2Gm(r)/c^2)}. \tag{2.2.13}$$

By using this relation we can solve the TOV equations with respect to the parameter N instead of using the radial distance.

An additional useful quantity to find is the specific enthalpy. This comes from the fact that for isentropic stars, Bernoulli's equations are expressed with respect to enthalpy. So, by dividing H with ρV we can find the specific enthalpy (h)

$$h(r) = \frac{\epsilon(r) + P(r)/c^2}{\rho(r)}. \tag{2.2.14}$$

After some calculations we can easily show that

$$N(r) = c^2\ln\big(h(r)/c^2\big). \tag{2.2.15}$$

This relation is going to be useful in the case where we have a picewise polytrope. In the case where we can not find h(r) we can find N(r) just by integrating equation 2.2.10.

2.3 GR effects outside the star

GR predicts that light bends when it passes near massive objects. NSs can not only curve the light that comes from an external source, but they also curve the light that they emit from their surface. As a result, part of the light emitted from the backside of a NS is going to be visible to an observer who stands in front of the NS. Hence, the size of this star is going to seem larger than it is in reality (Figure 2.3.1). The denser the NS, the greater the light bending is. (Pechenick et al. (1983)). In the case of a pulsar, there are times where the two polar caps are visible from the one side.

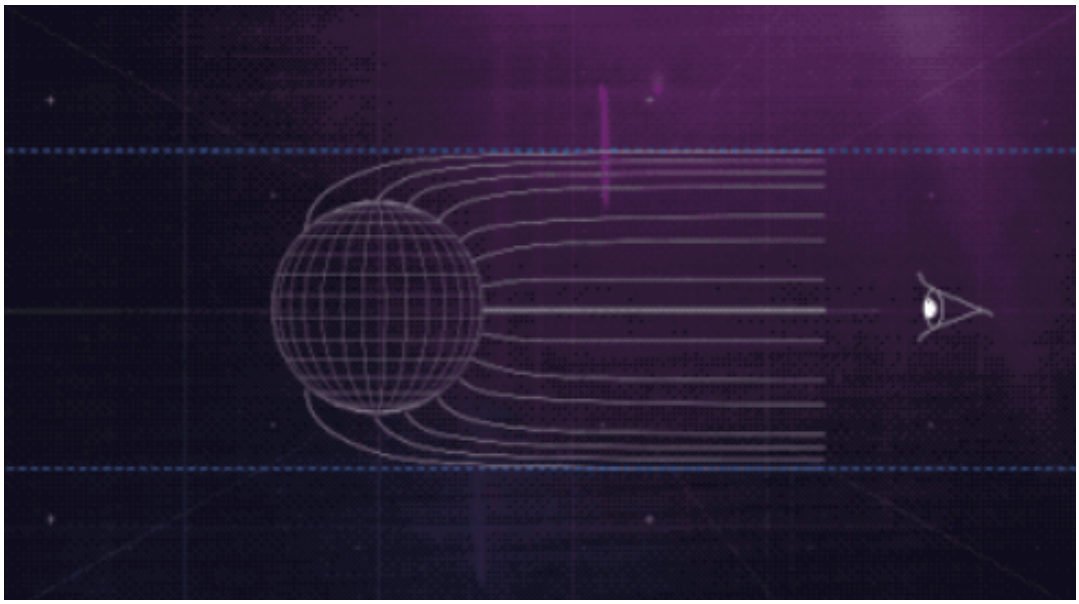

FIGURE 2.3.1: Light curvature. This figure is an original work of NASA's Goddard Space Flight Center/Chris Smith (USRA/GESTAR)[1]

The apparent size of the NS is not the only thing that changes. Gravity can also decrease the light frequency (red-shift). By using the Schwarzschild metric 2.2.8 we can find that the frequency of a source on the surface of the star (ω_0), is going to be measured by an observer far away from it, as follows (the equations in this section come from Potekhin (2010))

$$\omega_\infty = \omega_0 \sqrt{1 - x_g}. \tag{2.3.1}$$

[1]NASA's NICER Probes the Squeezability of Neutron Stars `https://www.nasa.gov/feature/goddard/2021/nasa-s-nicer-probes-the-squeezability-of-neutron-stars`

We can also define the red-shift parameter as

$$z_g = \omega_0/\omega_\infty - 1 = (1 - x_g)^{-1/2} - 1. \tag{2.3.2}$$

And we can write the apparent radius of the NS, as measured by an observer at infinity (R_∞) as

$$R_\infty = R(1 + z_g). \tag{2.3.3}$$

Furthermore, the effective temperature that is been measured far away from the source changes as follows

$$T_{eff}^\infty = T_{eff}/(1 + z_g) \tag{2.3.4}$$

As the luminosity is proportional to $R^2 T_{eff}^4$, the relation between the luminosity at the surface and at the infinity is going to be

$$L^\infty = L/(1 + z_g)^2. \tag{2.3.5}$$

Shaw et al. (2018), used Chandra and XMM to observe flux coming from NS and used this equation in order to define the R_∞. They assumed that the surface emits radiation uniformly and they found R_∞ assuming a hydrogen or a helium atmosphere. They found that a helium atmosphere leads to a larger R_∞ compared to the hydrogen one.

2.4 Rapidly spinning neutron stars

However, many neutron stars rotate rapidly, with millisecond periods. The rotation will change the spherical shape of these stars to an ellipsoid. As a result, we can not use the spherically symmetric metric anymore.

Komatsu et al. (1989) introduced the self-consistent field method to solve the Einstein field equations for an oblate axisymmetric rotating neutron star.

The spacetime metric has the general form

$$ds^2 = -e^{\gamma+\lambda}dt^2 + e^{2\alpha}(dr^2 + r^2 d\theta^2) + e^{\gamma-\lambda}r^2 sin^2\theta(d\varphi - \omega dt)^2, \tag{2.4.1}$$

where λ ,γ , α and ω are called metric potentials and depend on r and θ.

In the self-consistent field method introduced by Komatsu et al. (1989), the Einstein field equations take the form of partial differential equations for the metric potentials that are similar in structure to Poisson's equation. This leads to the introduction of Green functions, allowing the four metric potentials to be solved using an integral equation.

Making use of the numerical solution of this axisymmetric metric, the energy-momentum tensor and the conservation law someone can find the equations that give all the macroscopic parameters that describe the system. Cook et al. (1992) introduced a number of improvements to this method, including the introduction of dimensionless variables. In the next group of equations, we define their dimensionless variables with bars over the variable symbols, while symbols without bars have regular dimensions (the equations in this section come from Cook et al. (1994))

$$\bar{\mathrm{r}} \equiv \kappa^{-1/2} r, \tag{2.4.2}$$

$$\overline{\mathrm{M}} \equiv \kappa^{-1/2} \frac{G}{c^2} M, \tag{2.4.3}$$

$$\overline{\rho} \equiv \kappa \frac{G}{c^2} \rho, \tag{2.4.4}$$

$$\overline{\epsilon} \equiv \kappa \frac{G}{c^2} \epsilon, \tag{2.4.5}$$

$$\overline{\mathrm{P}} \equiv \kappa \frac{G}{c^4} P, \tag{2.4.6}$$

$$\overline{\Omega} \equiv \kappa^{1/2} \frac{1}{c} \Omega, \tag{2.4.7}$$

where $\kappa \equiv \frac{c^2}{G\epsilon_0}$ is used to convert between dimensionless and dimensionful variables, with ϵ_0 to be equal to 10^{15} g cm^{-3}. Ω is the angular velocity of the star as measured by an observer at infinity in rad/s. In our computations, we are modelling rigidly rotating neutron stars, so Ω has a constant value inside of the star.

Cook et al. (1992) also transformed from the r and theta coordinates to μ and s defined as follows

$$\mu \equiv cos\theta, \tag{2.4.8}$$

$$s \equiv \frac{\bar{\mathrm{r}}}{\bar{\mathrm{r}} + \bar{\mathrm{r}}_e}, \tag{2.4.9}$$

where μ and s take values from 0 to 1 (inclusive). Here $\bar{\mathrm{r}}_e$ is the equatorial coordinate radius.

By taking all these into account, the first thing that we want to do is to find the total mass of the system. As its name says, it's the sum of all the mass and energy that is included in the star. This means that we have to use not only the mass of the baryons that compose the neutron star (baryon mass M_0) and their internal energy (E), but also the gravitational binding energy (W) and the rotational kinetic energy (T) of the system. So, the total mass is defined as follows

$$M = M_0 + \frac{W}{c^2} + \frac{T}{c^2} + \frac{E}{c^2}. \tag{2.4.10}$$

Therefore, the total mass of the system when the NS rotates is given by

$$\begin{aligned} M = \frac{4\pi\kappa^{1/2} c^2 \bar{\mathrm{r}}_e^3}{G} \int_0^1 \frac{s^2 ds}{(1-s)^4} \int_0^1 d\mu e^{2\alpha+\gamma} \{ \frac{\overline{\epsilon} + \overline{\mathrm{P}}}{1-v^2} \\ [1 + v^2 + \frac{2sv}{1-s}(1-\mu^2)^{1/2} \hat{\omega} e^{-\lambda}] + 2\overline{\mathrm{P}} \}, \end{aligned} \tag{2.4.11}$$

and the circumferential equatorial radius is

$$R_e = \kappa^{1/2}\bar{\mathrm{r}}_e e^{[\gamma_e-\lambda_e]/2}, \tag{2.4.12}$$

where γ_e and λ_e are the values of γ and λ at the equator.
Also, we can calculate the value of the baryon mass by

$$M_0 = \frac{4\pi\kappa^{1/2}c^2\bar{\mathrm{r}}_e^3}{G}\int_0^1 \frac{s^2ds}{(1-s)^4}\int_0^1 d\mu e^{2\alpha+(\gamma-\lambda)/2}\frac{\overline{\rho}}{(1-\upsilon^2)^{1/2}}. \tag{2.4.13}$$

Here $\overline{\rho}$ is the rest mass density, υ=(Ω-ω)rsin$\vartheta e^{-\lambda}$ and $\hat{\Omega} = \bar{\mathrm{r}}_e\overline{\Omega}$.
We can also calculate the total rotational kinetic energy

$$T = \frac{2\pi\kappa^{1/2}c^2\bar{\mathrm{r}}_e^3}{G}\int_0^1 \frac{s^3ds}{(1-s)^5}\int_0^1 d\mu(1-\mu^2)^{1/2}e^{2\alpha+\gamma-\lambda}(\overline{\epsilon}+\overline{\mathrm{P}})\frac{\upsilon\hat{\Omega}}{1-\upsilon^2}. \tag{2.4.14}$$

The relation between the rotational kinetic energy and the angular momentum is given from the next equation

$$T = \frac{\hat{\Omega}}{2c\kappa^{1/2}\bar{\mathrm{r}}_e}J. \tag{2.4.15}$$

If we subtract from the total energy the gravitational energy and the rotational kinetic energy, what remains is what we define as the proper mass

$$M_p = \frac{4\pi\kappa^{1/2}c^2\bar{\mathrm{r}}_e^3}{G}\int_0^1 \frac{s^2ds}{(1-s)^4}\int_0^1 d\mu e^{2\alpha+(\gamma-\lambda)/2}\frac{\overline{\epsilon}+\overline{\mathrm{P}}}{(1-\upsilon^2)^{1/2}}. \tag{2.4.16}$$

The gravitational energy of the system is

$$W = (M_p + \frac{T}{c^2} - M)c^2. \tag{2.4.17}$$

Moreover, the value of the total angular momentum can be found by

$$J = \frac{4\pi\kappa c^3\bar{\mathrm{r}}_e^4}{G}\int_0^1 \frac{s^3ds}{(1-s)^5}\int_0^1 d\mu(1-\mu^2)^{1/2}e^{2\alpha+\gamma-\lambda}(\overline{\epsilon}+\overline{\mathrm{P}})\frac{\upsilon}{1-\upsilon^2}. \tag{2.4.18}$$

Finally, the hydrostatic equilibrium for a barotropic fluid is given by

$$h(\overline{\mathrm{P}}) - h_p = lnu^t - lnu^t_p, \tag{2.4.19}$$

where u^t_p is the four-vector velocity at the poles. By using the u^μ of a zero angular momentum observer we get that

$$h(\overline{\mathrm{P}}) - h_p = \frac{1}{2}[\gamma_p + \lambda_p - \gamma - \lambda - ln(1 - v^2)], \tag{2.4.20}$$

where γ_p and λ_p are the values of γ and λ at the pole.

2.5 Kepler frequency

We know from classical mechanics that there is an upper limit to the frequency that a rotating object can have. This limit is the Kepler frequency and can be found as follows: Imagine that we want to keep a test particle in a circular orbit around some other non-rotating heavy object (i.e. planet, stars). In order to do that, the centrifugal force must be equal to the gravitational force (Glendenning (1997)). So, in the Newtonian case we can easily find that in order to have a stable orbit around a star with mass M, on the equatorial plane at distance $r = R$, the rotational frequency Ω of the test particle has to be

$$\Omega = \sqrt{\frac{GM}{R^3}} \tag{2.5.1}$$

If a star rotates faster than this angular velocity, mass will be shed from its equator. This upper limit on angular velocity is called the Kepler frequency.

When we refer to the Kepler frequency (Ω_K) in the next chapters, we refer to the point where the orbit of the material on the equator of the star becomes unstable. Interestingly, the same relation stands for the Kepler frequency of a particle that is orbiting a non-rotating star, in general relativity. For the case where we have a rotating NS, the problem becomes much more complicated.

In this scenario, the Kepler instability takes place when (Cook et al. (1994))

$$\frac{1}{2}\frac{\partial}{\partial r}(\lambda+\gamma)-\frac{v}{1-v^2}\frac{\partial v}{\partial r}=0, \tag{2.5.2}$$

at the surface of the star. Since v depends on the star's angular velocity, this condition is only met for one angular velocity given a particular EOS and central density.

It is understandable that the use of such a relation in observational astronomy is not useful. As a result, simple empirical equation have been developed. For example Friedman et al. (1989) approximate the maximum value of the Kepler frequency ($\Omega_{K,max}$) as follows (Friedman et al. (1989))

$$\Omega_{K,max}=7.7\times10^3\times(\frac{M_{max}}{M_\odot})^{1/2}\times(R_{Mmax})^{-3/2}\frac{rad}{s}, \tag{2.5.3}$$

where M_{max} is the maximum mass of the NS and R_{max} is the radius of the neutron star with the maximum mass, for a given EOS. Such approximations are very useful since the observation of a neutron star spinning faster than this limit would rule out some proposed EOS.

2.6 Mass limit of neutron stars

2.6.1 Maximum mass of the non-rotating neutron stars

It has been mentioned that Oppenheimer and Volkoff (O-V) calculated an upper limit to the NS's mass close to 0.7 $M_\odot$, using the assumption that NSs are composed of neutrons that behave like a degenerate Fermi gas. Modern EOSs include more accurate physics, and result in maximum masses that are larger than the OV limit by a factor of 2-4, depending on the assumptions made by the EOS. Rhoades & Ruffini (1974), without taking into account any information from the astronomical observations, found a theoretical maximum possible value of 3.2 $M_\odot$ that is independent of the EOS. At the present date, the highest accurately measured mass is for the pulsar J0740+6620 with a mass of $2.08^{+0.07}_{-0.07}M_\odot$ (Fonseca et al. (2021)). Therefore, the real maximum mass value

must be larger or equal to this value and less than 3.2 $M_{\odot}$. Future observations might reveal larger mass neutron stars, which will allow us to discard all the EOSs that do not reach the measured mass. (Horvath et al. (2020))

2.6.2 Maximum mass of the rotating neutron stars

The maximum mass given an EOS given by the TOV equations (for a non-rotating star) is not the true maximum, if the star rotates. It is known that as a NS spins up, its total mass increases. This can be caused due to the increase of the kinetic energy, the decrease of the magnitude of the gravitational binding energy and the increase of the baryon mass (if the star accretes matter from its combanion star). In some cases their baryon mass can take values larger than the static maximum baryon mass limit (Cook et al. (1992)). This means that stars with such masses can not exist in the absence of rotation. These stars are called "supramassive" NSs.

The NSs can not spin-up forever. Above some spin frequency the NSs will become unstable. In this thesis we are going to take into account two instabilities. The first one happens when we reach the Kepler frequency (this is discussed in section 2.5), but we also have to take into account the case where the star becomes unstable to quasi-radial perturbations (Friedman et al. (1988)). This instability takes place when

$$\frac{\partial M}{\partial \epsilon_c}|_J = 0. \tag{2.6.1}$$

Breu & Rezzolla (2016) used the quasi-radial perturbations in their paper in order to find the maximum mass of the rotating NSs. A star that fulfills the above criterion becomes unstable. Therefore, the authors studied the case where we have a sequence of rotating neutron stars along this critical limit. Their mass is symbolized as M_{crit}. The authors provide an empirical approximation for the M_{crit}/M_{TOV} as a function of J/J_{Kepler}. Here M_{TOV} is the static maximum mass, for a given EOS, J is the normalized angular momentum and J_{Kepler} is the maximum normalized angular momentum (or the angular momentum at the Kepler limit). By using this equation, and setting J=J_{Kepler} they provide an approximation for the maximum mass of a rotating NS with a given EOS

with respect to M_{TOV} (Breu & Rezzolla (2016))

$$M_{max} := M_{crit}(J = J_{Kepler}) \approx (1.203 \pm 0.022) \times M_{TOV}. \tag{2.6.2}$$

A more simple approximation is given by Lasota et al. (1996). Here we have a linear relation between the maximum mass of the non-rotating neutron star (M_{max}(stat)) and the the maximum mass of the neutron star that rotates with the maximum Kepler frequency (M_{max}(rot)) (Lasota et al. (1996))

$$M_{max}(rot) = \mathscr{Y}_M \times M_{max}(stat), \tag{2.6.3}$$

where $\mathscr{Y}_M$ is just a coefficient and is equal to 1.18. This relation describes their data better than 3%. Also, we can find a similar relation between the radius of the star with mass equal to M_{max}(stat) and the one which is equal to M_{max}(rot). Below we give this empirical relation. $\mathscr{Y}_R$ is again just a coefficient, and is equal to 1.34 (Lasota et al. (1996))

$$R_{max}(rot) = \mathscr{Y}_R \times R_{max}(stat). \tag{2.6.4}$$

The deviation of their data from this best fit equation is less than 4%.

2.7 I-Love-Q

Along with the empirical relations for the maximum values of the mass (and their radius) and the Kepler frequency, we can also find similar relations for some other useful quantities. For example Ravenhall & Pethick (1994) in their paper give an approximate relation for the moment of Inertia (I) of a NS, as a function of its mass and radius

$$I \approx 0.21 \times \frac{MR^2}{1 - 2GM/Rc^2}. \tag{2.7.1}$$

Breu & Rezzolla (2016) also provide an approximate relation for the moment of inertia with respect to $C = M/R$

$$\bar{\mathrm{I}} := I/M^3 = \overline{\mathrm{a_1}} \times C^{-1} + \overline{\mathrm{a_2}} \times C^{-2} + \overline{\mathrm{a_3}} \times C^{-3} + \overline{\mathrm{a_4}} \times C^{-4}. \tag{2.7.2}$$

It is been observed that the coefficients $\overline{\mathrm{a_1}}$–$\overline{\mathrm{a_4}}$ change with respect to the angular momentum. For this reason, the authors give the values of these coefficients for different angular momentum values in Table 2 of their paper.

A more interesting result has been published by Yagi & Yunes (2013). In this paper the authors found out that the moment of inertia (I), the tidal deformability (λ^{tid}), known as the Love number, and the quadrupole moment (Q) are related to each other, and independent of the EOS choice. This means that if we know one of these three parameters we can find the others, without worrying about the nature of the EOS. The empirical relations, which the authors named "I Love Q" have the follow form (Yagi & Yunes (2013))

$$ln(y_i) = a_i + b_i \times ln(x_i) + c_i \times (ln(x_i))^2 + d_i \times (ln(x_i))^3 + e_i \times (ln(x_i))^4, \tag{2.7.3}$$

where i=1,2,3. When i=1 $y_1 = \bar{\mathrm{I}}$ and $x_1 = \overline{\lambda}^{tid}$, when i=2 $y_2 = \bar{\mathrm{I}}$ and $x_2 = \overline{\mathrm{Q}}$, and when i=3 $y_3 = \overline{\mathrm{Q}}$ and $x_3 = \overline{\lambda}^{tid}$. The coefficients can be found in Yagi & Yunes (2013) (keep in mind that we have different coefficient for neutron stars and quark stars). The line above I, Q and λ^{tid} means that we use the non-dimensional quantities which are defined as follows (Yagi & Yunes (2013))

$$\begin{aligned} \bar{\mathrm{I}} &= \frac{I}{M^3}, \\ \overline{\mathrm{Q}} &= -\frac{Q}{M^3\chi}, \\ \overline{\lambda}^{tid} &= \lambda^{tid}/M^5, \end{aligned} \tag{2.7.4}$$

where $\chi = \frac{J}{M^2}$.

One possible explanation for this universality is that during the mathematical calculation of these three parameters, the region that affects our results the most is the one which is outside the inner core. As we said before, the inner

core is the region where we have the most uncertainty and the main differences among the EOS models. Therefore, the equation that gives these parameters is mainly affected by the region that is almost similar among the different EOSs. This leads to this universality.

Furthermore, the fact that we can not distinguish two BHs with the same mass, spin frequency and charge (no-hair theorem) is introduced by the authors as an alternative way to explain these results. They are saying that the creation of NSs with similar properties like the BHs leads to these universal relations.

2.8 Binding energy

Another useful quantity is the binding energy (E_b). The E_b represents our cost of energy that we have to "pay", in order to remove all the baryons from the NS. E_b is defined as follows

$$E_b = M_0 - M. \tag{2.8.1}$$

Lattimer & Prakash (2001) make a discussion about the universality of the binding energy and they provide an approximation for its non-dimensional form

$$BE/M = \frac{0.6 \times \beta}{1 - 0.5 \times \beta}. \tag{2.8.2}$$

Here $\beta = GM/Rc^2$ and the deviation from their results is less than 20%.
Breu & Rezzolla (2016) give an improvement of this relation.

$$BE/M = d_1 \times \beta + d_2 \times \beta^2. \tag{2.8.3}$$

Here d_1 and d_2 are the coefficients of the best fit equation and can be found in their paper. Furthermore, they are saying that in the case where we have a rotating NS we can generalize this approximation by assuming that the two coefficients are second order polynomials of the non-dimensional angular momentum.

In section 3.5, we compute the binding energy, moment of inertia, and maximum masses and compare with the results shown in the preceding sections as a consistency check on our results.

2.9 Oblate shape

Morsink et al. (2007) showed that the shape of the NSs is also universal. By knowing the non-dimensional equatorial compactness $\zeta := \frac{GM}{R_e c^2}$ and the non-dimensional squared frequency $\epsilon_\Omega := \frac{\Omega^2 R_e^3}{GM}$, someone can find a simple approximate relation between the equatorial radius and the radius at an angle θ from the rotational axis

$$\frac{R(\theta)}{R_e} = 1 + \sum_{n=0}^{2} \alpha_{2n}(\zeta, \epsilon_\Omega) P_{2n}(cos\theta), \tag{2.9.1}$$

where $P_n(cos\theta)$ is the n order Legendre Polynomial and $\alpha_{2n}(\zeta, \epsilon_\Omega)$ are the best fit coefficients and they can be found in table 1 of their paper. Keep in mind that these coefficients are different in the case where we have a rotating quark star.

For the case where the R_e is not known Morsink et al. (2007) give a similar empirical relation for $\frac{R_e}{R(\theta)}$ but by changing the R_e dependence of ζ and ϵ_Ω to $R(\theta)$.

These relations are useful as they can be used in order to define the oblateness of the NSs shape. By knowing this information we would be able to better understand the Doppler effects due to the rotation of the star and the way that light bends.

2.10 Gravitational waves

September 14, 2015,[2] was an important day when humankind detected, for the first time, gravitational waves (GW) with the LIGO (Laser Interferometer

[2]Gravitational Waves `https://www.ligo.caltech.edu/page/gw-sources`

Gravitational-wave Observatory) detector (Abbott et al. (2016)). These waves were predicted by Einstein's theory of general relativity in 1916. For GW, it is not points in a transmitting medium that are oscillating, but the space-time itself. The main source of the GW that can be detected by LIGO are binary systems with black holes and/or neutron stars that inspiral and merge. Every system with mass and a non-zero, time-changing quadrupole moment can radiate gravitational waves. Even you and your friend, when you are dancing around one another emit GW! However, the amplitude of these waves are extremely small and they can only be measured if the moving objects are very dense and accelerating.

GWs travel with the same speed as the Electromagnetic waves do. However, GW can travel through a region with dense matter without scattering, unlike photons. This means that observations of GW give us additional information about sources beyond what can learn from their electromagnetic signals.

August 17, 2017, was the first time that GWs have been detected by a binary neutron star system (GW170817 Abbott et al. (2017)). Such events are very important to our research, as the GW signal contains information that can be used in order to place limits to the tidal deformability and indirectly to the NS radius. Of course, this allows us to discard all the EOSs that do not agree with these restrictions.

GW emission is a really fascinating scientific area, however we are not going to study it in this specific thesis. Nevertheless, it is worth mentioning as it is a new way for us to observe the Universe.

Chapter 3

Rotating neutron star sequences

The equations for the macroscopic parameters of a rotating NS can't be solved analytically, as can be see from section 2.4. The only remaining option is to use our computational knowledge in order to solve them numerically.

In our research we used the RNS code (Stergioulas & Friedman (1995)) (written in C) which numerically solves these equations for a given EOS, its central energy density and a value of the $R_{pole}/R_{equator}$. The authors use $R_{pole}/R_{equator}$ instead of the frequency of a NS. This choice has been made in order to avoid worrying about the case where the Maclaurin spheroids can allow two possible solutions (more information about the Maclaurin spheroids can be found in chapter 1 of Chandrasekhar (1969)). The RNS code uses the equations and computational methods that have been suggested by Komatsu et al. (1989). The equations are in the improved form that Cook et al. (1994) suggested (equations in section 2.4).

A brief explanation of the techniques that have been used in Komatsu et al. (1989) follows: First, the authors make an initial guess for the values of the metric potentials, the energy density and the angular velocity. Then they integrate the Einstein field equations to find the values for each potential (for more details, see their paper). The new potentials are used to find new values for the energy density and the angular velocity. They repeat this process until the values of the parameters do not have any significant change. For the integration they use the Simpson's method. Next, by using Newton-Raphson method

they solved the equations that are given in their paper, in order to find the frequency at the equator, the pole and the center, the point with the maximum density, the equatorial radius and the enthalpy. These parameters are essential, since though integration over the whole space they calculate the macroscopic parameters introduced in section 2.4.

Calderon Noguez (2019) in his thesis, modified the RNS code to create sequences of rotating NSs by keeping the baryon mass constant. The modified code has the name NSSS (Neutron Stars Spin Sequences). In this thesis we modified NSSS and we created different types of rotating NSs by keeping constant the central energy density.

The equations that Cook et al. (1994) provide are with respect to s and μ coordinates, therefore in section 3.1 we give a brief description of the s - μ space. Next, in section 3.2, we are going to show how we modified the NSSS code in order to serve our purpose[1]. In section 3.3 we talk about the EOSs that have been used in this thesis. Finally, in section 3.4 we give detailed examples showing the properties of one of the EOSs and show that our results agree with the empirical approximations that have been introduced in the previous chapter.

The table 3.0.1 gives the notations we use in the next chapters. We also define the non-dimensional equatorial compactness as

$$C_e = \frac{M}{R_e}\frac{km}{M_\odot}, \tag{3.0.1}$$

and the non-dimensional initial compactness as

$$C_* = \frac{M_*}{R_*}\frac{km}{M_\odot}. \tag{3.0.2}$$

[1]The code that we used for this thesis can be found at `https://github.com/rns-alberta/RNS_Sequences_with_constant_ec.git`

TABLE 3.0.1: Table of Symbols notation

ϵ_c	Central energy density divided by c^2 (g/cm^3)
M	Total mass (in $M_\odot$)
M_0	Rest mass, also known as baryonic mass (in $M_\odot$)
M_*	Mass of the first nonrotating NS in a sequence (in $M_\odot$)
R_e	Equatorial radius of the NS (in km)
R_{ratio}	Ratio of the polar radius (r_p) and the equatorial radius (r_e)
R_*	Equatorial radius of the first nonrotating NS in a sequence (in km)
P	Spin Period (in s)
ν	Spin frequency (1/P) (in Hz)
Ω	Frequency of the star ($2\pi \times \nu$) (in Hz)
Ω_K	Kepler limit for rotation (in Hz)
J	Angular momentum (in cm^2 g/s)
T	Rotational kinetic energy divided by c^2 (in $M_\odot$)
W	Gravitational binding energy divided by c^2 (in $M_\odot$)
E	Internal energy energy divided by c^2 (in $M_\odot$)

3.1 The μ - s space

Instead of coordinates θ ($0 \leq \theta \leq \pi/2$) and r ($0 \leq r \leq \infty$), we use the new coordinate system μ ($0 \leq \mu \leq 1$) and s ($0 \leq s \leq 1$). The main problem of this transformation is that it is impossible to transfer from s to r, when s=1 ($r \to \infty$) inside the code. So, instead of going to infinity, we define a number SMAX (SMAX<1) which denotes a distance far away from the star. This is also the maximum possible value for s. Now, the code is ready to divide the μ - s space in small pixels.

The number of the pixels is given by the user, as he or she has to define the values SDIV and MDIV, which correspond to the number of intervals that we split the s-axis and μ-axis respectively. We give a suggestion for the values of these parameters in our code (i.e. for SMAX we can use 0.9999 and by default MDIV×SDIV=201×401), but of course someone can choose something else.

This can happen by changing these values in the "Makefile", but remember that every time that something is changed in this file, the object files must be erased (the files with ".o" at the end). After you type the command "make" in a terminal window, the code is prepared to run with the new values that have been chosen.

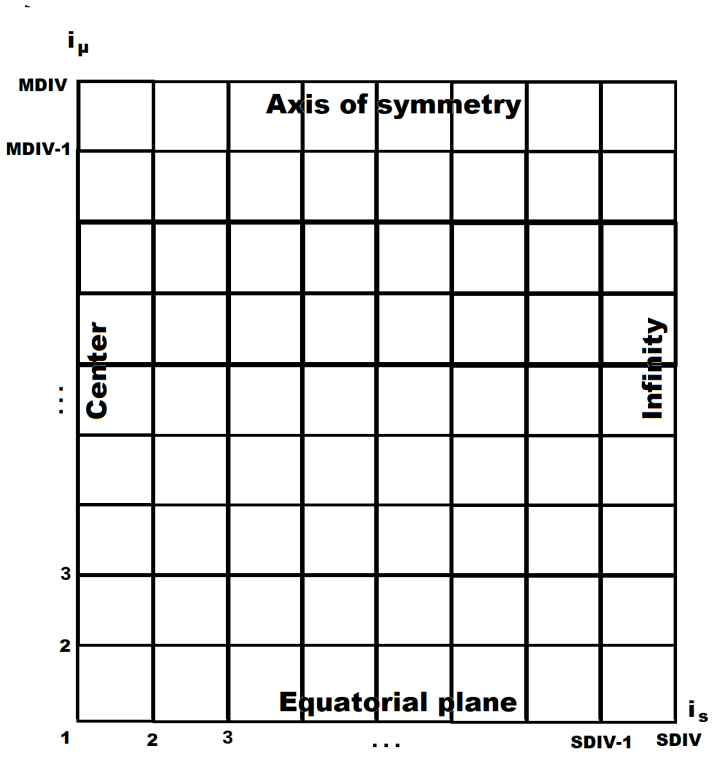

FIGURE 3.1.1: μ - s space

We can find the value of s and μ for the point (i_μ,i_s) from the following equations

$$\mu(i_\mu) = \frac{i_\mu - 1}{MDIV - 1}, \tag{3.1.1}$$

$$s(i_s) = SMAX \frac{i_s - 1}{SDIV - 1}, \tag{3.1.2}$$

where i_s=1,2,3....SDIV and i_μ = 1,2,3...MDIV. Keep in mind that $i_s = 1$ corresponds to the center of the star, i_s = SDIV corresponds to infinity, $i_\mu = 1$ corresponds to the equatorial plane and i_μ = MDIV corresponds to the polar direction. Also, the equatorial radius is represented by the point s = 0.5, μ = 0. The figure 3.1.1 represents this μ - s space.

3.2 Sequences of rotating neutron stars with constant central energy density

For purposes that are going to be explained in the next chapter, we want to investigate the case where we have a sequence of neutron stars with constant central energy density. To do that we modified a little bit the NSSS code.

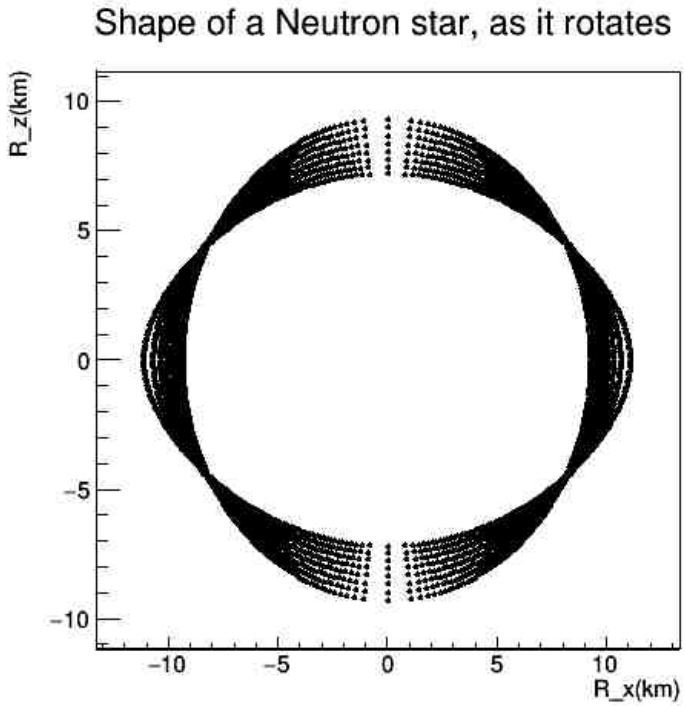

FIGURE 3.2.1: Example for the change of NSs' shape in a sequence

The **first star in each sequence** must be non-rotating. This means that we start from a star where its $R_{ratio} = 1$, as for a non-rotating star the polar radius is equal to the polar radius. As the spin value increases in a sequence,

the polar radius decreases and the equatorial radius increases, so the shape of the NS changes from sphere to an ellipsoid (Figure 3.2.1 shows us how the shape of a NS changes in a sequence). This means that the R_{ratio} value has to be less or equal to the unity, and of course larger than 0. So, the change of the R_{ratio} value is equivalent to the change of the frequency.

The next stars are created, and their R_{ratio} changes by 0.005. This value has been chosen just for the purpose of this thesis. The user can choose a different value by changing the `ratio_ch` parameter in the *"nsss.c"* file.

The **last star in each sequence** rotates with a frequency a little bit smaller than the Kepler frequency. The sequence stops after the creation of this star.

The first sequence created has a central energy density chosen by the user (we talk about this choice in the following paragraphs). When the first sequence reaches the Kepler frequency the whole process is repeated with a new value for ϵ_c that is `e_ch` = 0.05 $\times 10^{15}$ g/cm^3 smaller than before. Sequences are created until their central energy density becomes smaller than `energy_min` = 0.22 $\times 10^{15}$ g/cm^3 in the case where we use the Polytropic EOSs, and `energy_min` = 0.32 $\times 10^{15}$ g/cm^3 in the case where we use the speed of sound model (again `energy_min` and `e_ch` can be modified by the user). These values represent the point just before the crust EOS or the chiral effective field theory (cEFT) band is used (we are going to give more information for the crust EOS and the cEFT band in sections 3.3.1 and 3.3.3.1).

After we choose the values of `ratio_ch`, `energy_min` and `e_ch` we must run the makefile and the code is ready. We can run the code by writing the command *"./nsss"* plus other information that is necessary for the code to solve the problem. Such information is the EOS that we want to use and the central energy density that is going to remain constant in the sequence.

To choose the EOS that is going to be used by the program, *"-f eos_file_name"* has to be included in the command line that runs the code. Also, an error message is given in the case where the EOS file is not included in the same directory as the NSSS files. The structure of these files is described in subsection 3.3.2.

By including -e in the command line we can choose the value of the energy density of the NS at the center. Now, we can run our modified code by using the command *"./nsss -f eos_file -e ϵ_c"*.
On the screen the following parameters are printed out: ϵ_c, M, M_0, M_*, R_e, R_{ratio}, R_*, Ω, Ω_K for each step. The screen looks as follows:
NS_data_eos_file_name.txt
NS_data_eos_file_name.txteos_file_name_table.txt

ϵ_c	Mass	M_0	M_*	Radius	Rratio	R_*	Omega	Omega_K
1.02	1.40539	1.54508	1.40539	11.89613	1.000	11.89612	0.000	1675.12580
1.02	1.40861	1.54872	1.40539	11.92191	0.995	11.89612	138.841	1664.81679
1.02	1.41174	1.55219	1.40539	11.94916	0.990	11.89612	198.264	1658.95479
.	.	.	.	.	.	.	.	.
.	.	.	.	.	.	.	.	.
.	.	.	.	.	.	.	.	.

A file with the name "NS_data_eos_file_name.txt" has been created in the same directory. Each column in this file represents the following values:
ϵ_c, M, M_0, Mstat, R_e, R_{ratio}, Rstat, ν, ν_{kepler}, J, T, W, R_{ratio}_S
in the units that have been stated before. R_{ratio}_S is the same as the R_{ratio} but by using the Schwarzschild-like metric instead of the isotropic one. This parameter is useful for reasons that are going to be clarified later on.

3.2.1 EOS file structure

Before we move forward let's say a few things about the proper structure that an EOS file must have in order to be accepted by the RNS code. On the **first line** an EOS file must have the number of different values of density that are included in the file. In the **next lines** we have four columns. Each column represents a specific quantity. The first column is the energy density in g/cm^3, the second one represents the pressure in $dynes/cm^2$, the third one is the relativistic enthalpy N in $(cm/s)^2$ and the fourth one is the baryon number density in cm^{-3}.

3.3 EOSs used in this thesis

To run the NSSS code we need an EOS file. But how can we be sure that the EOS that we are using is the closest to reality? At present, the correct EOS for the NS core is unknown. There is a wide range of nuclear EOS models that agree with astronomical observations and the nuclear physics experiments. In order to take into account the uncertainty on all these three fields we can create a set of randomly generated EOSs by taking into account the restrictions provided with experiments. Using a randomly generated basis of EOS, we avoid being prejudiced by specific choices of nuclear theories which have yet to be proven correct. At the end of the day, we might not get the correct values for the macroscopic parameters of the system, however we expect to correctly find the way that these parameters change in a sequence and the range of their possible values.

Below, we discuss two possible ways to generate random EOSs[2]. The first method is based on the assumption that the core behaves as a piecewise polytrope. The second one comes from assumptions that have been made about the speed of sound profile of the core. All the parameters that describe our generated EOS can be found in the Appendices (Tables A.0.1, A.0.2, A.0.3 and A.0.4).

3.3.1 The crust EOS

A possible way to model a NS is by splitting its structure into two separate regions. The first one is the crust (the low density region) and the second one is the core (where the densities are extremely large). For the crust EOS we can use some pre-existed EOSs, as the eosNV (Negele & Vautherin (1973)), the eosFPS (Lorenz et al. (1993)), or the eosBPS (Baym et al. (1971)). The physical assumptions made in these different crust EOSs are not very different, so the choice of crust EOS does not affect our results. For this thesis we are going to use eosNV for the polytropic EOS and eosBPS for speed of sound model. More details about the crust can be found in their papers.

[2]The code that we used to create the two EOS sets can be found at `https://github.com/rns-alberta/EOSGenerator.git`

3.3.2 Piecewise Polytrope

For this model we assume that the core is separated into three polytropic regions (Read et al. (2009)) and their "borders" can be defined by two baryon mass density values ρ_1 and ρ_2 (see figure 3.3.1). A polytropic equation is the equation where the pressure and density are related to each other by the following expression (the equations in this section come from Read et al. (2009))

$$P(\rho) = K\rho^{\Gamma}. \tag{3.3.1}$$

Here K is a constant and Γ is the adiabatic index. In piecewise polytropic case the pressure is

$$P(\rho) = K_i\rho^{\Gamma_i}, \tag{3.3.2}$$

where i denotes the three separate areas (i=1 is the outer part, i=2 is the middle part and i=3 is the inner part of the core).

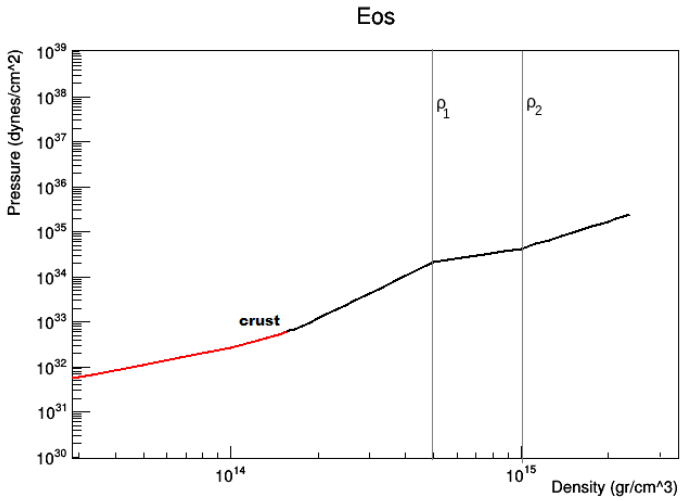

FIGURE 3.3.1: EOS PP structure

To find the energy density ϵ in the core we can use the first law of thermodynamics

$$d\frac{\epsilon}{\rho} = -pd\frac{1}{\rho}. \tag{3.3.3}$$

Keep in mind that here we set the speed of light c to be equal to 1. Therefore, in reality in this section ϵ = (energy density/c^2).

By using the first law of thermodynamics and the polytropic equation, we can find that the energy density inside region i is

$$\epsilon(\rho) = (1 + \alpha_i)\rho + \frac{K_i}{(\Gamma_i - 1)}\rho^{\Gamma_i}, \tag{3.3.4}$$

where continuity of the energy density at the lower energy boundary of the region defines α_i as

$$\alpha_i = \frac{\epsilon(\rho_{i-1})}{\rho_{i-1}} - \frac{K_i}{(\Gamma_i - 1)}\rho_{i-1}^{\Gamma_{i-1}}. \tag{3.3.5}$$

When $\alpha \to 0$ at the limit where $\rho \to 0$ and $\frac{\epsilon}{\rho} \to 1$.
We said that the specific enthalpy is defined as

$$h = \frac{\epsilon + P}{\rho}. \tag{3.3.6}$$

By replacing ϵ with the equation above and P with the polytropic equation we can find that specific enthalpy is related to ρ based on the following expression

$$h(\rho) = (1 + \alpha_i) + \frac{\Gamma_i K_i}{(\Gamma_i - 1)}\rho^{\Gamma_i - 1}. \tag{3.3.7}$$

Finally, we can find the relativistic enthalpy by taking the logarithm of the specific enthalpy

$$N = \ln(h). \tag{3.3.8}$$

Now, we have an equation for each parameter that is necessary for the creation of an EOS file. The last thing that we have to do is to define the values of Γ_1, Γ_2, Γ_3, the values of ρ_1, ρ_2 and the pressure at ρ_1 (or the higher value of the Pressure and density of the crust). If we know these 6 parameters we can "match" the crust with the core and create a single catholic EOS.

3.3.2.1 Restrictions

We could start now taking random values for our parameters and create random EOSs. However, we have to remember that our EOS must obey the same restrictions as nature does. For example, the principle that nothing can travel faster than the speed of light. Or with its fancy name "causality".
Also, the EOS that we are going to use has to agree with our observations. For instance, an EOS that can not support the heaviest observed NS is useless, as it does not correspond to reality.
Based on these two restrictions, Hebeler et al. (2013) give a possible range of values for the previous parameters. This range is given below

- $1.5 \leq \Gamma_1 \leq 4.5$,
- $0 \leq \Gamma_2 \leq 8$,
- $0.5 \leq \Gamma_3 \leq 8$,
- $1.5\ \rho_0 \leq \rho_1 \leq 7.3\ \rho_0$,
- $\rho_1 \leq \rho_2 \leq 7.8\ \rho_0$,
- $\rho_2 \leq \rho_{center} \leq 8.3\ \rho_0$.

Where $\rho_0 = 2.28 \times 10^{14}$ g cm^{-3} and 8.3 ρ_0 is the maximum possible value of the central energy, based on the Hebeler et al. (2013) paper. Moreover, the authors provide the minimum central density that can support a 1.97 $M_\odot$ NS, and it is 2.0 ρ_0. From the crust EOS we can choose the border between the crust and the core (P_{crust}, ρ_{crust}). So, the EOS now is

$$P(\rho) = \begin{cases} P_{eosNV} & \rho \leq \rho_{crust}, \\ K_1\rho^{\Gamma_1} & \rho_{crust} \leq \rho \leq \rho_1, \\ K_2\rho^{\Gamma_2} & \rho_1 \leq \rho \leq \rho_2, \\ K_3\rho^{\Gamma_3} & \rho_2 \leq \rho. \end{cases} \tag{3.3.9}$$

By using these restrictions we can randomly choose a value for each parameter and create a set of random EOS files. Also, we can solve the TOV equations for a non-rotating NS and find the Mass-Radius curves.

3.3.3 The speed of sound model

An alternative way to create a set of random EOSs is based on some assumptions for the speed of sound inside the star (Greif et al. (2019)).
The speed of sound is defined as follows

$$c_s = \sqrt{\frac{dP}{d\epsilon}}. \tag{3.3.10}$$

This means that if we know the relation of c_s^2 with respect to the energy density, we can solve the equation above and find the connection among pressure and energy density

$$P(\epsilon) = \int_0^{\epsilon} (c_s(\epsilon')/c)^2 d\epsilon'. \tag{3.3.11}$$

3.3.3.1 Low density region

We start by using the BPS EOS for the crust up to 0.5 n_0 (where $n_0 = 0.16$ fm^{-3}). After this point, we add a chiral Effective Field Theory (cEFT) band that is provided by Hebeler et al. (2013). The cEFT band takes place from 0.5 n_0 up to 1.1 n_0.

When the baryon density takes values from 1.1 n_0 up to 1.5 n_0 the matter behaves as a Fermi liquid. Based on the Landau Fermi liquid theory we can find that the speed of sound in this region is (Baym & Pethick (1991))

$$(\frac{c_s}{c})^2 = \frac{1+F_0}{m_N^*/m_N} \frac{1}{3m_N^2} (3\pi^2 n)^{\frac{2}{3}}. \tag{3.3.12}$$

According to Schwenk et al. (2003) and Lorenz et al. (1993), F_0 is approximately -0.5(2) and m_N^*/m_N is roughly 0.9(2). Greif et al. (2019) in their paper state that $1 + F_0$ and m_N^*/m_N have an order of magnitude of one. Based on that

they make the conservative assumption that

$$\frac{1+F_0}{m_N^*/m_N} <= 3. \tag{3.3.13}$$

Therefore the speed of sound in this region has to be less or equal to $\sqrt{0.163}$ c. This number has been found by using n = 1.5 n_0 and the conservative assumption in the Landau Fermi liquid theory. In the case where the speed of sound of an EOS that has been created passes this critical value in the low density region, we just discard it.

3.3.3.2 Core restrictions

Again, in order to define the core EOS we have to take into account the restrictions that come from the laws of physics.
As before, we require that the speed of sound is less than c.
Also, we expect that the pressure is going to increase as the energy density rises. Which means that we want the c_s to be positive.
In addition, we have to keep in mind that based on the perturbative quantum chromodynamics (pQCD), the speed of sound at large densities (10^{16} g/cm^3) converges to $\frac{c}{\sqrt{3}}$ from below. The explanation for this limit can be found in the appendices of the paper by Kojo et al. (2021).

Furthermore, Bedaque & Steiner (2015) showed that an EOS can support a NS with a mass larger than two solar masses only in the case where the c_s becomes larger than $\frac{c}{\sqrt{3}}$ in the region between the crust and the center of the core. This means that the speed of sound is going to be almost zero close to the crust, then increases until a maximum value (larger than $\frac{c}{\sqrt{3}}$) in the middle region), and finally take the value $\frac{c}{\sqrt{3}}$ from below at very high densities (Figure 3.3.2 illustrates this behavior).

This behavior, takes place when the baryon density becomes larger than 1.5 n_0 and it can be expressed by a Gaussian function plus some terms that are going to force $(c_s/c)^2$ to approach 1/3 from below at very high densities (Greif

et al. (2019))

$$(\frac{c_s}{c})^2 = \alpha_1 \times \exp\{-0.5 \times (x-\alpha_2)^2/\alpha_3^2\} + \alpha_6 + \frac{1/3 - \alpha_6}{1+\exp(-\alpha_5 \times (x-\alpha_4))}. \tag{3.3.14}$$

Here x $\equiv \epsilon/(m_N n_0)$ and m_N is the nucleon mass and is equal to 939.565 MeV.

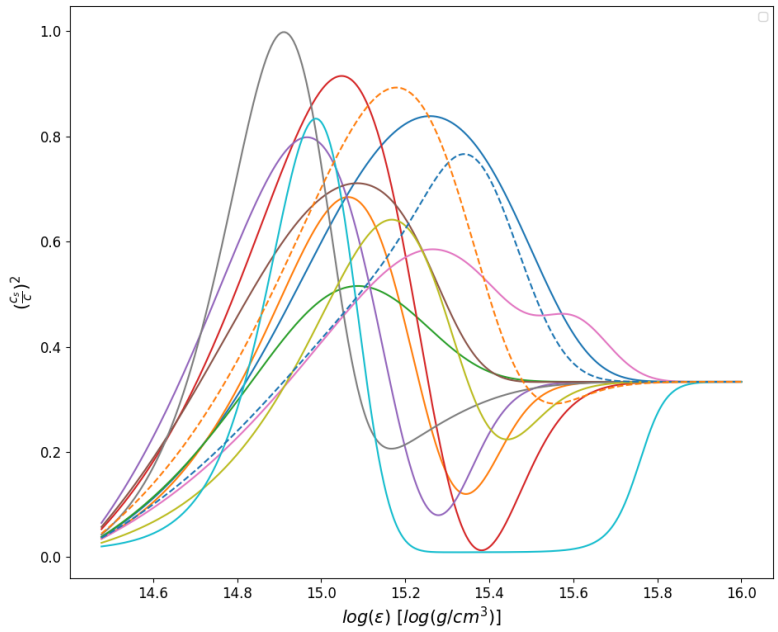

FIGURE 3.3.2: c_s^2 profile of a number of random EOSs.

Greif et al. (2019) give a range of possible values for the α coefficients

- $0.1 \leq \alpha_1 \leq 1.5$,
- $1.5 \leq \alpha_2 \leq 12$,
- $0.05 \leq \alpha_3/\alpha_2 \leq 2$,
- $1.5 \leq \alpha_4 \leq 37$,
- $0.1 \leq \alpha_5 \leq 1$.

These ranges have been created by taking into account the three restrictions that we have introduced in the previous paragraphs. α_6 can be found by matching the c_s at low densities (1.5 n_0) to the c_s of the upper or the lower point of the cEFT band (we choose randomly with 50% chance for each case).

3.3.4 Choice of the number of the EOSs

At this point we have described two methods for computing sets of random EOSs[3]. But, what is the minimum number of EOSs that should be created? For this thesis the choice is based on the coefficients of the best fit surfaces that are going to be discussed later. We choose enough EOSs in such a way that the coefficients will not change significantly if we include additional EOSs. We find out that this number is 28, but for this thesis we used 32. 19 of them are Piecewise Polytropes and the 13 of them came from the speed of sound model. We chose to use a larger number of piecewise polytropes than the c_s ones, since EOS PPs cover a larger area in the Mass-Radius space. This comes from the fact that the c_s model creates much softer EOSs, as we forced the square of speed of sound to approach 1/3 from below at very high densities, and also as we forced the speed of sound to be less than $\sqrt{0.163}$ c at very small densities. These two restrictions can guarantee that an initially soft EOS will remain soft for all the energy density values (Greif et al. (2019)). Figures 3.3.3 and 3.3.4 show the EOSs and the resulting mass-radius curves that we chose for this thesis.

3.3.5 Hadronic, hybrid and quark EOSs

Lastly, we want to be sure that our results agree with other EOSs that are based on some nuclear or quark matter restrictions, that might not be modelled by one of the random EOS. For this reason we use an additional eight EOS models, chosen because their physical description might lead to different properties than any of the randomly generated EOS. Firstly, there are two

[3]The data that we used for this thesis can be found at `https://github.com/rns-alberta/NS_Sequence_constant_ec_Data.git`

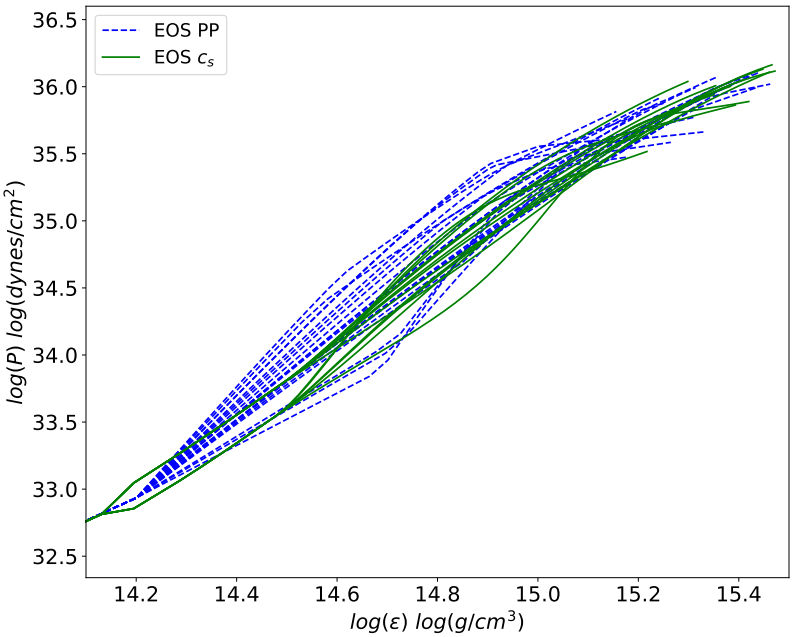

FIGURE 3.3.3: Random EOSs

versions of EOS ABPR (Alford et al. (2005)) and one of the EOS QHC21(D) (Kojo et al. (2021)). These three are hybrid EOSs (section 1.3.5.2). Secondly, we have the EOS APR (Akmal et al. (1998)) where it takes into account the three-nucleon interactions. Next, we have two versions of the EOS BBB (Baldo et al. (1997)). Here, the authors used the asymmetric nuclear matter and the three-body forces. We also include two versions of the EOS HLPS (Hebeler et al. (2013)) as an internal consistency check, since the EOS HLPS are generated using the same method as our EOS PP. The EOS H0 is an EOS which includes nuclear matter and hyperons (table 5.8 Glendenning (1997)). Finally, we have the EOS L (Pandharipande & Smith (1975)) where they assume that π^0 condensate exist in the core and the neutron matter is in a solid state.
EOS Q160 (Alcock et al. (1986)) represents a "bare" quark star without a hadronic crust, and we use it in order to see how our results change with more extreme changes to the physical assumptions.
Figure 3.3.5 shows the Mass-Radius curves for these EOSs.

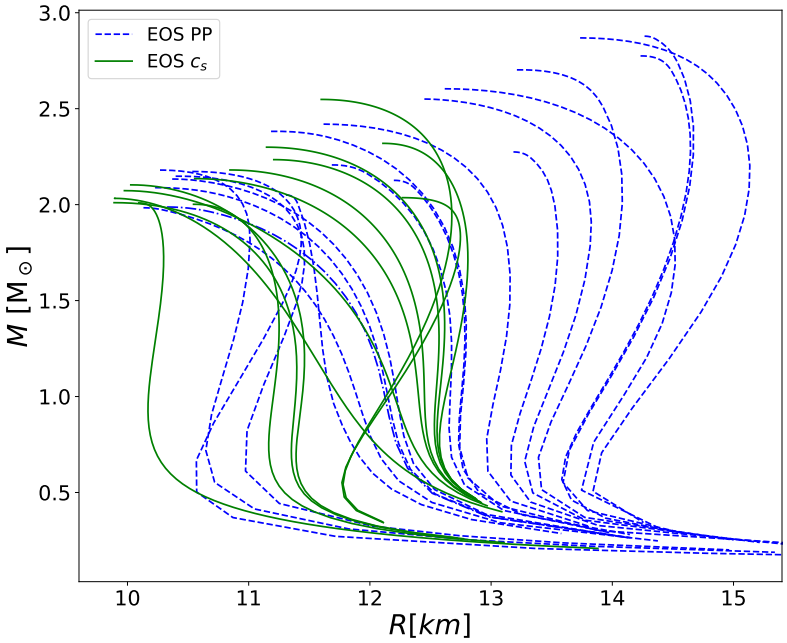

FIGURE 3.3.4: Mass - Radius curves of the two EOS families

3.4 Processing the outputs

The NSSS computer program and the 32 randomly generated EOS described in the previous sections provide all the tools needed to compute sequences of rotating neutron stars that span a realistic range of properties. We used the 32 EOSs, computed sequences with constant central density, and extracted all the macroscopic properties, such as the mass and equatorial radius, that describe a rotating NS. The first thing that makes sense to do, is to investigate how these parameters change with respect to the spin frequency. A useful thing to do is to properly normalize the frequency, since for each EOS we expect different values for the Kepler frequency. Therefore, in the next subsection we introduce a new approximation for the Kepler frequency.

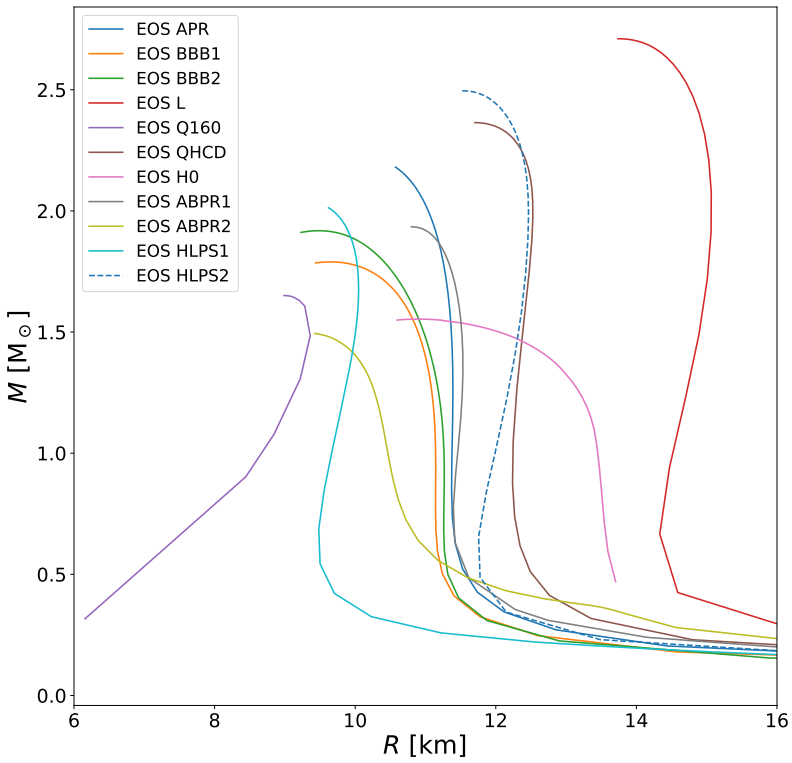

FIGURE 3.3.5: Mass - Radius curves of the hadronic, hybrid and quark EOSs

3.4.1 Our empirical approximation for the Kepler frequency

A first approach to normalize the frequency is by assuming that the Kepler frequency (Ω_K) has the same structure as the Newtonian limit, but multiplied by a coefficient. In this case the normalized frequency is defined as follows

$$\Omega_n := \frac{\Omega}{\Omega_K(empirical)}, \tag{3.4.1}$$

where $\Omega_K(empirical)$ is an empirical approximation of the Kepler frequency. For the present thesis we assume that $\Omega_K(empirical)$ has the following form

$$\Omega_K(empirical) := N_\Omega \times \sqrt{\frac{GM_*}{R_*^3}}, \tag{3.4.2}$$

where N_Ω is just a function of C_*, and $\sqrt{\frac{GM_*}{R_*^3}}$ is the non-rotating neutron star Kepler frequency in the Newtonian limit.

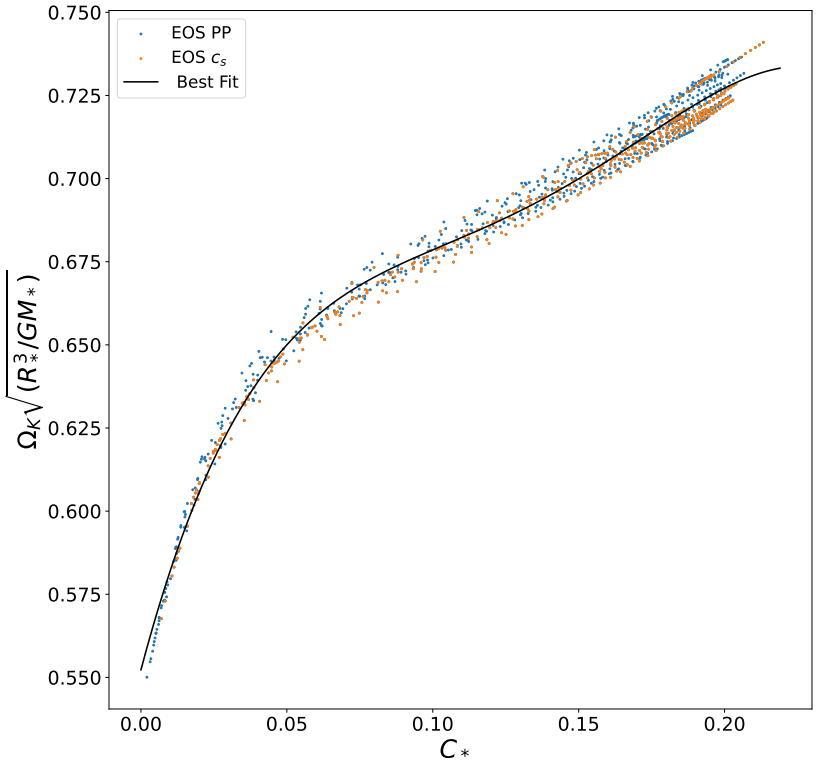

FIGURE 3.4.1: $\Omega_K/\sqrt{\frac{GM_*}{R_*^3}}$ vs C_*

We use figure 3.4.1 to find a polynomial relation [4] between N_Ω and C_*. The new normalized frequency is defined as follows

$$N_\Omega \approx -326.48 \times C_*^4 + 180.61 \times C_*^3 - 35.211 \times C_*^2 + 3.304 \times C_* + 0.552, \tag{3.4.3}$$

with $R^2 = 0.9895$. R^2 is the coefficient of determination and represents the fraction of the variance in the dependent variable (i.e. N_Ω) that is predictable

[4]For our best fit equations we use numpy.polyfit for the polynomial functions `https://numpy.org/doc/stable/reference/generated/numpy.polyfit.html` and scipy.optimize.curve_fit for the more complicated functions `https://docs.scipy.org/doc/scipy/reference/generated/scipy.optimize.curve_fit.html`

from the independent variable (i.e. C_*) (note that R^2=1 means that the equation perfectly fits all the data, and R^2=0 means that the equation gives the same results as if we just used the mean value of our data). Also, keep in mind that our best fit equations are valid for $0.014 \leq C_* \leq 0.22$.
In the worst case, our best fit equation deviates from our data by 1.60%. Here (and in the next sections), we define the deviation of one quantity Z from their best fit equation as

$$Dev(Z) = (Z_{data} - Z_{bestfit})/Z_{data}. \tag{3.4.4}$$

By taking all this into account, $\Omega_K(empirical)$ takes the following form

$$\begin{aligned}\Omega_K(empirical) \approx \sqrt{\frac{GM_*}{R_*^3}} \times (&-326.48 \times C_*^4 + 180.61 \times C_*^3 \\ &-35.211 \times C_*^2 + 3.304 \times C_* + 0.552).\end{aligned} \tag{3.4.5}$$

3.4.2 EOS properties for a rotating NS

In this section we now use one particular EOS in order to provide a detailed example of how the properties of a neutron star change when rotation is added. We chose the first piecewise polytrope in our collection, EOS PP0.

In figure 3.4.2 we show how the total mass changes with respect to the central energy density for all the sequences that have been produced for the EOS PP0. We use this plot to illustrate all the properties of the rotating NSs. For example, we can see all the possible values that the total mass can take.

Also, in figure 3.4.2, the **thick black solid line** corresponds to the curve that describes the non-rotating NS. The **blue dots** that form vertical lines correspond to rotating stars. It can be seen that along each vertical line the central energy density of the rotating stars is constant. As the EOS that we use is a piecewise polytrope, we show in our plots with **yellow line** the case where the central baryon mass density (ρ_c) is equal to ρ_2, and we use a **red line** to illustrate the case where $\rho_c = \rho_1$.

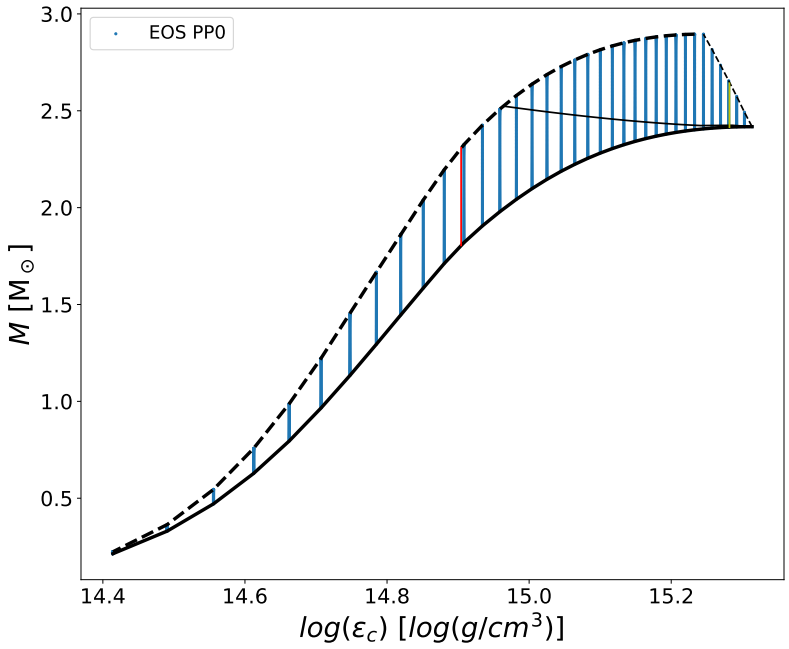

FIGURE 3.4.2: Total mass vs central energy density for EOS PP0

Furthermore, the **thick black dashed line** represents the stars that are rotating very close to the Kepler frequency. Finally, as the RNS code can not provide us with the limit where the stars become unstable to the quasi-radial perturbations, we add "by hand" this limit (the **thin black dashed line**). We did that by taking a look at a similar plot that is provided by Cook et al. (1994). As we said before, in this case they created sequence of rotating NSs with constant baryon mass. We saw that a simple approximation for this limit is a straight line that connects the non-rotating maximum mass point with the overall maximum mass point.

More than that, we can find all the supramassive stars that belong to a supramassive sequence (the region above the thin black solid line). A supramassive sequence, is a sequence of rotating NSs where they can spin-down by radiating angular momentum away, however their baryon mass is kept constant. At the end of the sequence all these NSs are doomed to become unstable to quasi-radial perturbations. This means that these stars are going to form a

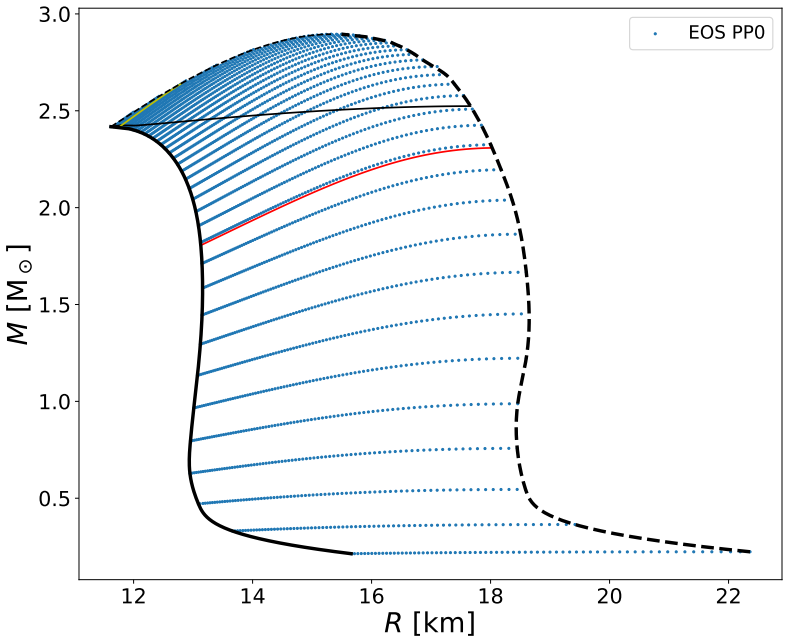

FIGURE 3.4.3: Total mass vs equatorial radius for EOS PP0

black hole at the end of their life. For those who want to learn more about these sequences, they can take a look to Cook et al. (1994) paper.

Figure 3.4.3 shows the possible values that the total mass and the equatorial radius can take for the same sequences of stars. The different curves have the same meaning as in the previous figure.

Furthermore, in figure 3.4.4 we can see how the total mass is related to the frequency. Also, for each sequence we can find its Kepler frequency. Overall, sequences with more massive stars can spin with faster frequencies. To understand that we have to go back to the Mass - Radius curve figure. Remember that for NS EOSs we expect that the radius will decrease as the mass increases. This means that more massive stars are going to have larger compactness values. We know from Newtonian physics that compactness is strongly related to the gravitational binding energy. Therefore, the high gravitational binding energy of the system guarantees that the Kepler instability is going to take place at higher frequencies.

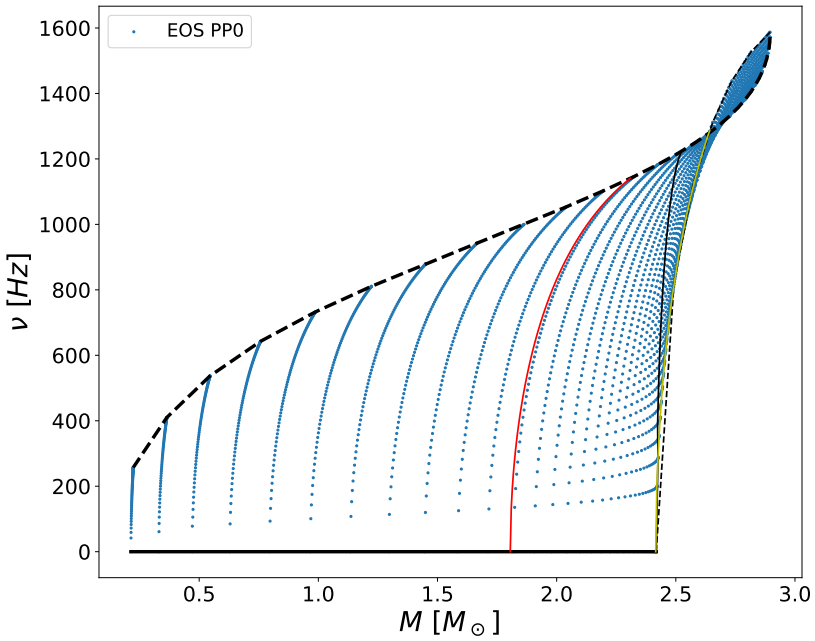

FIGURE 3.4.4: Spin frequency vs total mass for EOS PP0

In figures 3.4.5 and 3.4.6 we show how the normalized total mass (M/M_*) and equatorial radius (R_e/R_*) change with respect to the normalized angular velocity, Ω_n. This plot shows that M/M_* increases almost exponentially with Ω_n^2 (or $M/M_* \propto e^{A_0 \times \Omega_n^2}$). This dependence is slightly different for each sequence. Each sequence has a different constant value of C_*. We made the assumption that along a sequence, M/M_* can be approximated as follows

$$M/M_* \approx 1 + (e^{A_0 \times \Omega_n^2} - 1) \times A_1 + f(\Omega_n), \tag{3.4.6}$$

where A_0 and A_1 are constants and $f(\Omega_n)$ are the additional corrections. For this paper we are going to neglect the contribution of the $f(\Omega_n)$ function. As it can be seen above we forced this equation to give $M/M_* = 1$ when $\Omega_n = 0$.

We have a similar behavior for R_e/R_*, but this changes for spins closer to the Kepler frequency. Near the Kepler frequency, we have a faster increase of the equatorial radius as the centrifugal force becomes comparable to the

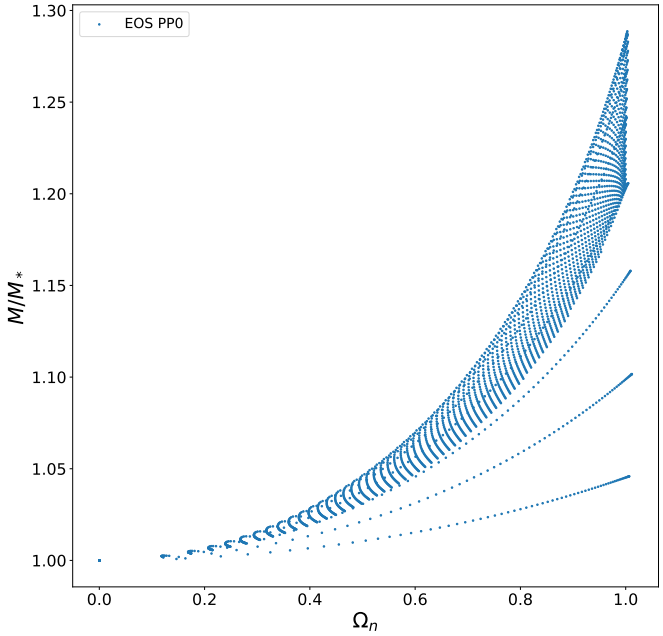

FIGURE 3.4.5: M/M_* vs Ω_n for EOS PP0

gravitational force. So in this case, we use the same equation as before, but we add a function that goes to infinity close to the Kepler frequency. For this thesis we chose the $[ln(1-(\frac{\Omega_n}{1.1})^4)]^2$ function. We divide Ω_n with 1.1 in order to avoid taking the logarithm of a negative number. This is required from the fact that our empirical equation for the Kepler frequency is not perfect, so in some cases Ω_n will be a little bit larger than 1.

Based on the discussion above we assumed that for a sequence (where C_* is constant) the equatorial radius can be approximated as follows

$$R_e/R_* \approx 1 + (e^{B_0 \times \Omega_n^2} - 1 - B_1 \times [ln(1-(\frac{\Omega_n}{1.1})^4)]^2) \times B_2 + g(\Omega_n), \qquad (3.4.7)$$

where B_0, B_1 and B_2 are constants and $g(\Omega_n)$ are the additional corrections. Again, we neglect $g(\Omega_n)$ and we force the equation to give $R_e/R_* = 1$ when $\Omega_n = 0$.

Equatorial compactness is another useful parameter to study. In figures

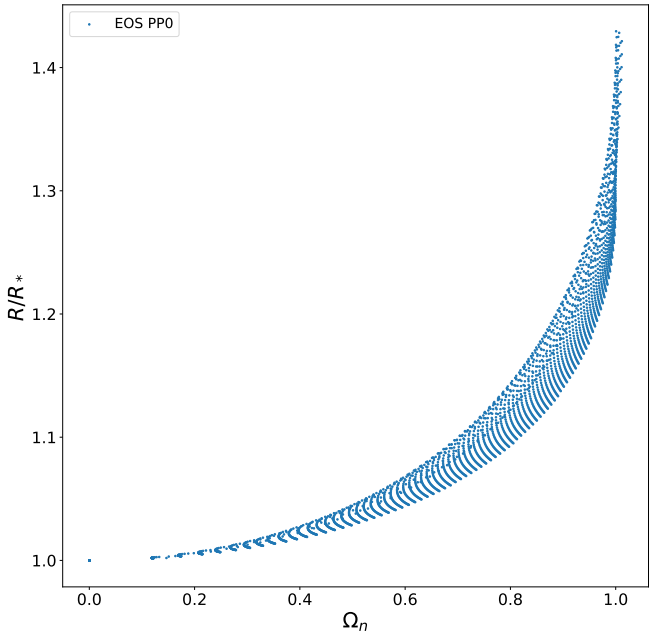

FIGURE 3.4.6: R_e/R_* vs Ω_n for EOS PP0

3.4.5 and 3.4.6 we saw that the mass and the radius change in a very similar way for most of the frequencies. As a result, we expect that compactness will remain almost constant until we get close to the Kepler frequency. Indeed, we can see in Figure 3.4.7 that in the case where Ω_n is less than the 80% of Ω_K, compactness remains approximately constant (a change less than 2%). This is valid for relatively large values of C_* ($C_* \geq 0.08$). For smaller values of C_* this change takes values from 2% up to 13% when $\Omega_n \approx 0.8$. Based on this behavior we use the following equation for compactness

$$C_e \approx C_* + C_0 \times ln(1 - (\frac{\Omega_n}{1.1})^3), \tag{3.4.8}$$

where C_0 is a constant. We forced this equation to give $C_e = C_*$ when $\Omega_n = 0$. Furthermore, in Figure 3.4.7 we can see that compactness decreases with the central energy density. This means that compactness and ϵ_c are strongly related to each other. Therefore, in the next chapter, instead of trying to understand how these parameters depend on ϵ_c, we can investigate their dependence on C_*

(as compactness remains almost constant along a sequence too).

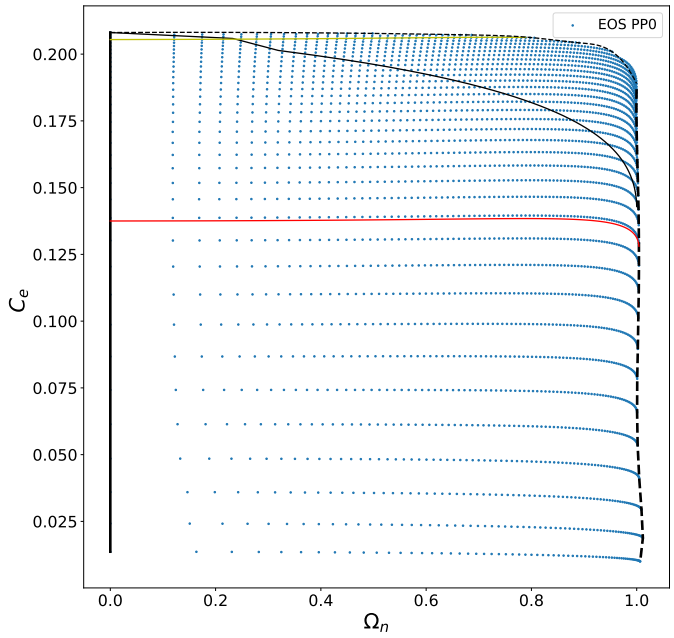

FIGURE 3.4.7: C_e vs Ω_n for EOS PP0

3.5 Satisfaction of other empirical approximations

In Sections 2.6.2 - 2.8 we reviewed some of the approximate relations that other authors have introduced for the moment of inertia, the binding energy and the maximum mass of the rotating NS. In the following subsections we will try to see if our calculations agree with these relations and give some similar expressions based on our data.

3.5.1 Stars with the maximum mass and their radius

Inspired by Lasota et al. (1996), we also find an approximate relation between M_{max}(rot) and M_{max}(stat) (and their radii). In the following plots, the red line denotes the best fit line from Lasota et al. (1996) and the blue line comes from Breu & Rezzolla (2016). Each black dot represents one of our 32 EOS, and the black line is the best fit to these points.

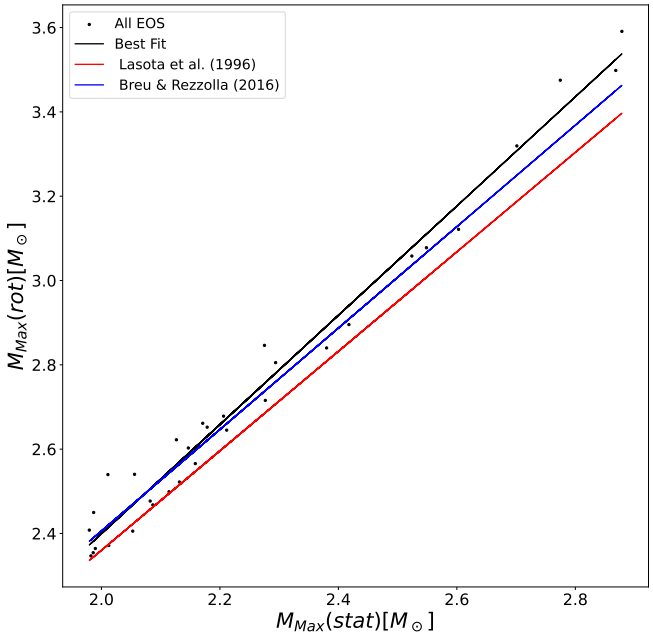

FIGURE 3.5.1: $M_{max}(rot)$ vs $M_{max}(stat)$

The best-fit lines to our data points are

$$M_{max}(rot) = 1.30 \times M_{max}(stat) - 0.19, \tag{3.5.1}$$

$$R_{max}(rot) = 1.3832 \times R_{max}(stat) - 0.7394. \tag{3.5.2}$$

The deviation is less than 4.97% and 5.98% for the mass and radius plots, respectively. These best fit equations are valid for $1.98 < M_{max}(stat) < 2.88$ and $9.87 < R_{max}(stat) < 14.27$.

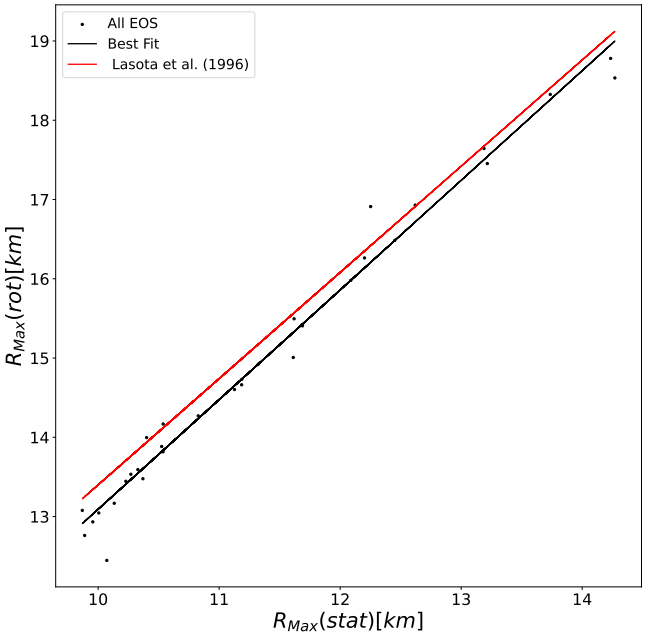

FIGURE 3.5.2: $R_{max}(rot)$ vs $R_{max}(stat)$

It can be seen from Figures 3.5.1 and 3.5.2 that our best fit equations are very similar to the equations that the other authors found.

3.5.2 Moment of Inertia

The RNS code does not provide the moment of inertia directly, as a result we used the relation between the angular momentum and the moment of inertia for our calculations

$$I = J/\Omega. \tag{3.5.3}$$

Here I is in $M_{\odot}km^2$. In the limit of non-rotating NSs I $\rightarrow \frac{0}{0}$, so in the next calculations we excluded these points.

It can be seen from figure 3.5.3 that the normalized moment of inertia goes to infinity as we get closer to the limit of stars with small compactness, since M$\rightarrow$ 0. Therefore, it makes sense to expect that the approximate expression

that gives the normalized moment of inertia will be inversely proportional to the initial compactness. Based on that, and based on the relation that Breu & Rezzolla (2016) provide in their paper, we fit our data using the following equation

$$I/M^3 = \frac{12.94}{(0.0021 + C_*)} - \frac{2.16}{(0.087 + C_*)^2} - \frac{78.90}{(1.24 + C_*)^3}, \tag{3.5.4}$$

with a maximum deviation equals to 10.58%.

In figure 3.5.3 we also show the empirical equations that come from Ravenhall & Pethick (1994) and Breu & Rezzolla (2016) papers. It can be seen that we have a better agreement with the more modern approximation of Breu & Rezzolla (2016). Also, Ravenhall & Pethick (1994) approximation seems to diverges more as we go closer to sequences with smaller values of initial compactness.

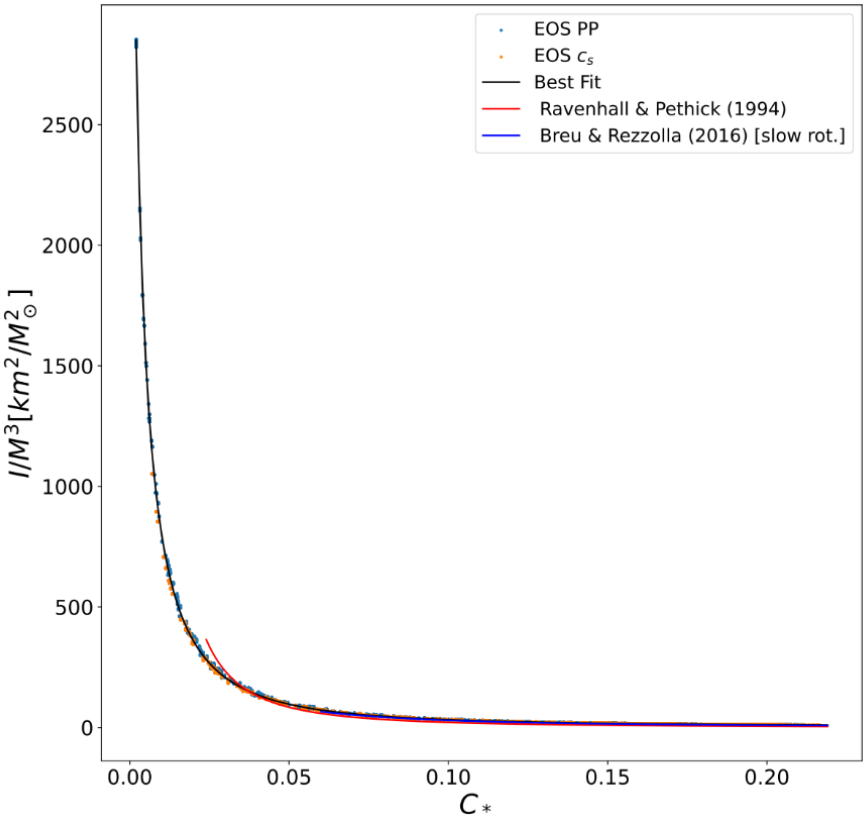

FIGURE 3.5.3: I/M^3 vs C_* for all EOS.

3.5.3 Binding energy

For the Binding energy, we used a similar equation as Breu & Rezzolla (2016) did

$$E_b/M = -0.0121 + 0.685 \times \frac{GM_*}{R_* c^2} + 0.00335 \times (\frac{GM_*}{R_* c^2})^2, \tag{3.5.5}$$

with $R^2 = 0.9827$.

All in all, we can see that the empirical approximations that come from our work agrees with other authors' approximations. We also provided similar empirical approximations that seem to work better at smaller values of compactness.

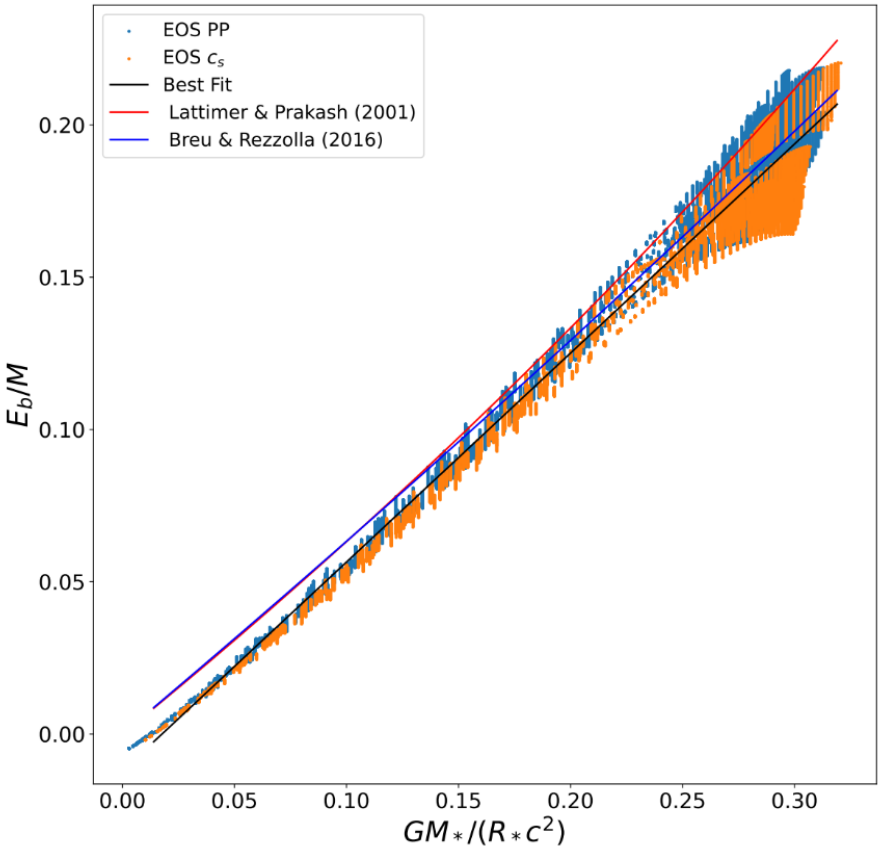

FIGURE 3.5.4: E_b/M vs $GM_*/R_* c^2$ for all EOS. Note that M_* is in g and R_* is in cm.

Chapter 4

Method for adding spin corrections

One major goal in the field of neutron star astrophysics is to determine the correct EOS of matter in the dense core of a NS. The correct EOS could be found if the mass and radius of many NSs are measured (Miller et al. (2020)). For each proposed EOS, the stellar structure equations can be solved yielding a range of masses and radii allowed by the EOS and these values can be compared with the set of measured values. The difficulty with this procedure is that most applications that are used to infer the EOS solve the spherically symmetric TOV equations for non-rotating NS, while many of the measurements are of rapidly rotating neutron stars. Since the mass and radius of a rotating NS will be larger than the corresponding non-rotating NS, this type of procedure could lead to systematic errors. The goal of this thesis is to derive a simple set of correction factors to allow the inclusion of rapid rotation in an EOS inference code.

In Chapter 3, we investigated the dependence of a NS's mass and radius on the normalized spin parameter Ω_n. This spin parameter is the ratio of the star's angular velocity to an approximate expression for the Kepler frequency. It is useful to define the dimensionless quantities M/M_* and R_e/R_*, where M and R_e are the mass and equatorial radius of a rotating NS and M_* and R_* are the corresponding mass and radius of the non-rotating NS. The compactness ratio $C_e = \frac{M}{R_e}\frac{km}{M_\odot}$ is also often used in astrophysics, and we define a non-rotating compactness by $C_* = \frac{M_*}{R_*}\frac{km}{M_\odot}$. In Chapter 3 we found the dependence of M/M_*,

R_e/R_*, and C/C_* on Ω_n given in equations 3.4.6, 3.4.7 and 3.4.8 respectively. The square of Ω_n is approximately the ratio of the centrifugal force to the gravitational force at the equator, and is a measure of the importance of rotation. It is obvious that both M/M_* and R_e/R_* (Figures 4.1.1 and 4.2.1, respectively), depend on both Ω_n and the central energy density (or $C_* = \frac{M_*}{R_*}\frac{km}{M_\odot}$). For this reason, two 2d histograms have been created in order to make the change of mass and radius with respect to C_* and to Ω_n visible. In these graphs we included all the EOSs, in order to see how the mass and the equatorial radius spin corrections are related to the nature of the EOS.

In all the 2D histograms we used a different bin sizes for different Ω_n range of values. This comes from the fact that we have fewer data points at small frequencies. When Ω_n takes values from 0 to 0.2 we used a bin size equal to 0.1. From 0.2 to 0.4 we use a bin size equal to 0.05 and beyond that point the bin size is approximately equal to 0.01. For the C_* we used a bin size approximately equal to 0.007. Finally, for the case where we show the deviation of a quantity from their best fit equation we show the maximum value in each bin. Otherwise we show the mean value of each bin.

In the next sections we are trying to make 3.4.6, 3.4.7 and 3.4.8 more general by trying to determine their C_* dependencies.

4.1 Spin corrections for the mass

Starting from equation 3.4.6 for the dependence of M/M_* on Ω_n, we assume that A_0 is a constant and A_1 is a function that changes with the initial compactness. For simplicity, we use a 4^{th} order polynomial equation. The new approximation for M/M_* becomes

$$\begin{aligned} M/M_* \approx 1 + (e^{A_0 \times \Omega_n^2} - 1) \times (A_1 + A_2 \times C_* \\ + A_3 \times C_*^2 + A_4 \times C_*^3 + A_5 \times C_*^4). \end{aligned} \tag{4.1.1}$$

We fitted our data on this equation and we found that this best fit surface is characterized by an R^2 which is equal to 0.9808. The coefficients of this

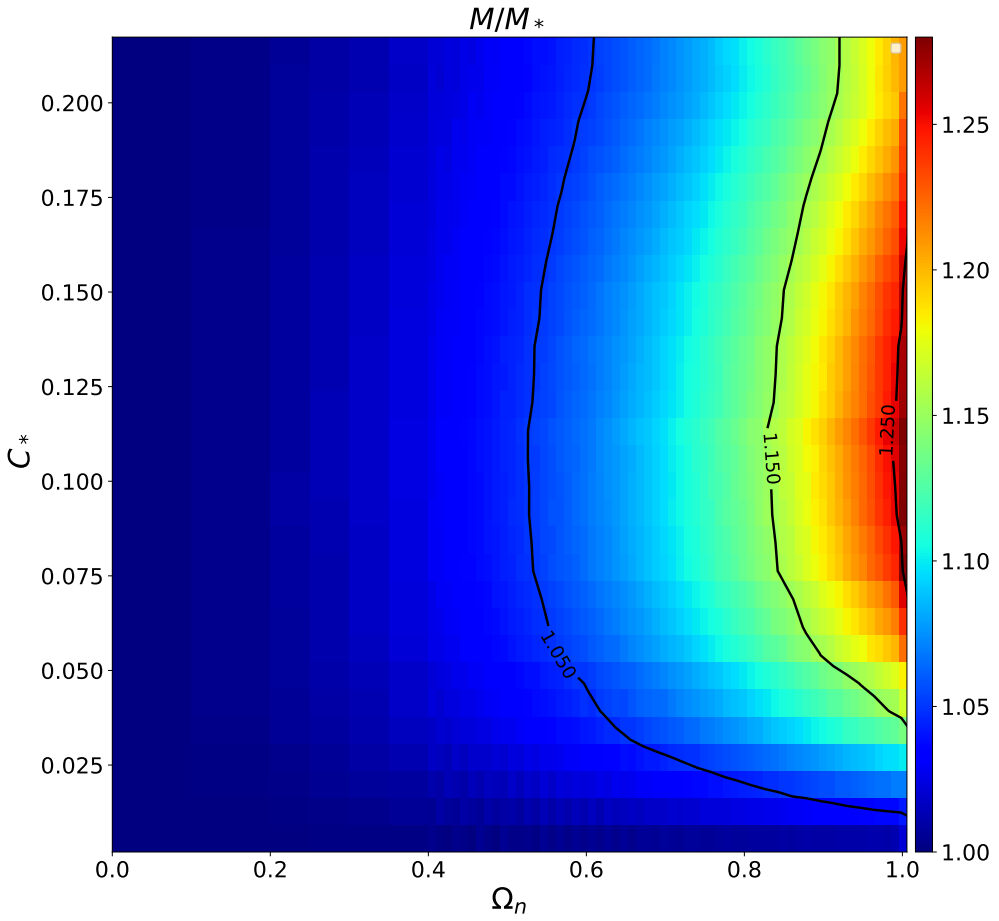

FIGURE 4.1.1: M/M_* vs C_* vs Ω_n. Each bin gives the mean value of the data within it. In figure B.0.1 we show the same plot but in 3 dimensions.

equation can be found below

$$M/M_* \approx 1 + (e^{1.127\times\Omega_n^2} - 1) \times (-0.016 + 3.123 \times C_* \\ -20.721 \times C_*^2 + 41.202 \times C_*^3 - 6.464 \times C_*^4). \tag{4.1.2}$$

In Figure 4.1.2 the deviation of the best fit equation from our data is illustrated. The deviation is less than 2.5%, for frequencies less than 80% of the Kepler frequency. For faster frequencies the deviation increases until it becomes approximately 4.6%.

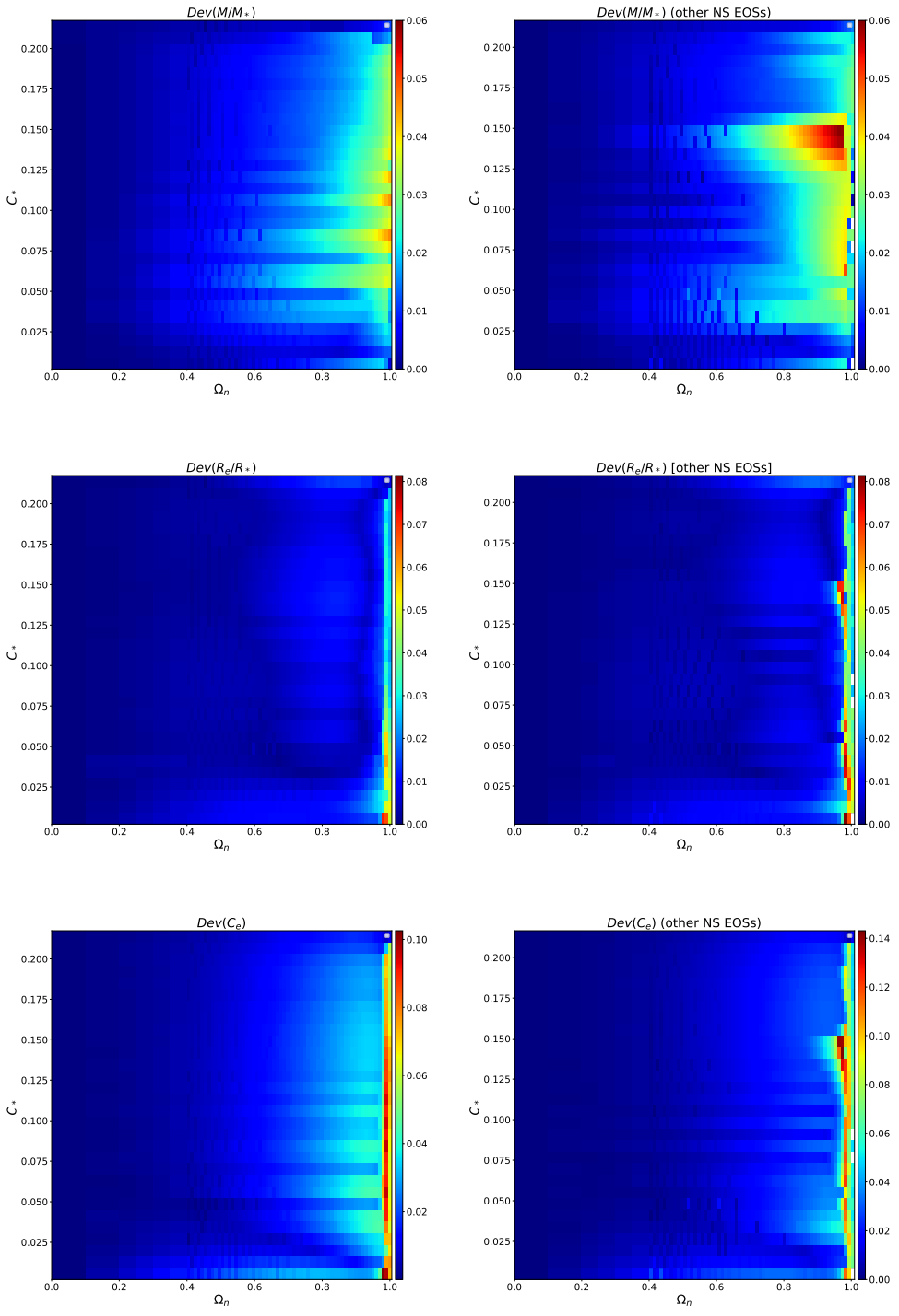

FIGURE 4.1.2: Deviation of each EOS from our best fit surfaces in a 2D histogram. Each bin represents the maximum value of the deviation inside it. On the left side we have the two EOS families, and on the right side we have the other hadronic and hybrid EOSs. Figure B.0.4 shows the same thing but in 3D

It can be seen from figure B.0.4 that at high frequencies the spin corrections to the mass strongly depend on the choice of the EOS.

To be more specific, very stiff and soft EOSs are the ones with the largest magnitude of deviation. Their only difference is that stiff EOSs have a positive value and soft EOSs have a negative value of the deviation. Therefore, we can conclude that the change of the mass is not 100% universal, however as typical measurement uncertainty is larger than 5% we can assume that it is universal.

We can find the value of M/M_* when the NS becomes unstable by only choosing stars spinning at the Kepler limit. In Figure 4.1.3 we show the best fit equation of $\frac{M}{M_*}|_K$ with respect to C_*, where $\frac{M}{M_*}|_K$ is M/M_* at the Kepler limit

$$\frac{M}{M_*}|_K \approx 71.388 \times C_*^3 - 39.56 \times C_*^2 + 6.272 \times C_* + 0.9662, \tag{4.1.3}$$

where the maximum deviation is 5.47% and $R^2 = 0.8698$. The relatively small value of R^2 compared to the other cases, makes clear again the M/M_* dependence on the nature of the EOS at high frequencies.

4.2 Spin corrections for the equatorial radius

We use the same logic for R_e/R_* given in equation 3.4.7. Here we keep B_0 and B_1 constant, and we assume that B_2 is a 5^{th} power polynomial function of C_*. The R_e/R_* equation becomes

$$\begin{aligned} R_e/R_* \approx 1 + (e^{B_0 \times \Omega_n^2} - 1 - B_1 \times [ln(1 - (\frac{\Omega_n}{1.1})^4)]^2) \times (1+ \\ B_2 \times C_* + B_3 \times C_*^2 + B_4 \times C_*^3 + B_5 \times C_*^4 + B_6 \times C_*^5). \end{aligned} \tag{4.2.1}$$

The coefficients of the best fitted surface are given below

$$\begin{aligned} R_e/R_* \approx 1 + (e^{0.203 \times \Omega_n^2} - 1 + 0.1611 \times [ln(1 - (\frac{\Omega_n}{1.1})^4)]^2) \times (1 - 15.496 \times C_* \\ +442.60 \times C_*^2 - 4945.62 \times C_*^3 + 23458.06 \times C_*^4 - 40544.25 \times C_*^5). \end{aligned} \tag{4.2.2}$$

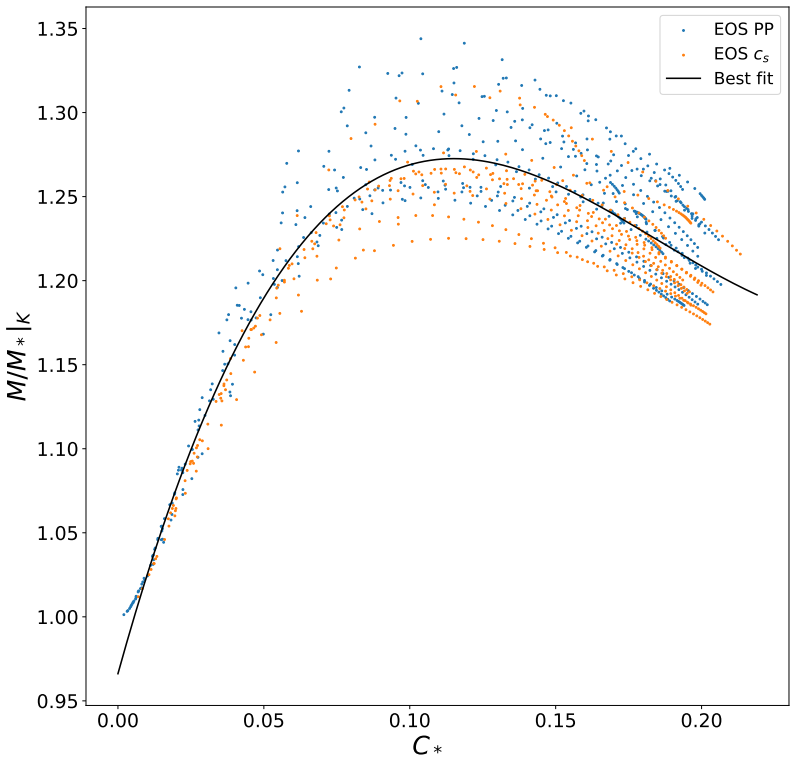

FIGURE 4.1.3: $\frac{M}{M_*}|_K$ vs C_*

The R^2 of our best fit equation is 0.9939. Also, from Figure 4.1.2 we can see that in general the deviation is less than 1.5% for most of the frequencies (i.e. up to 0.98% Ω_K for high compactness values). This only changes when we get really close to the Ω_K. There, the deviation increases up to 4%, except in the cases where the initial compactness is very small and the deviation increases up to 7.2%. Despite the relatively high value of deviation at small compactness values, we have to remember that the existence of such stars in nature is unlikely and that we take into account this limit in our analysis just for completeness.

In this case it seems that the equatorial radius change is truly universal and independent to the EOS choice. This relatively large increase of the deviation comes mainly from the fact that our best fit equation fails to describe the behavior of R_e/R_* close to the Kepler limit.

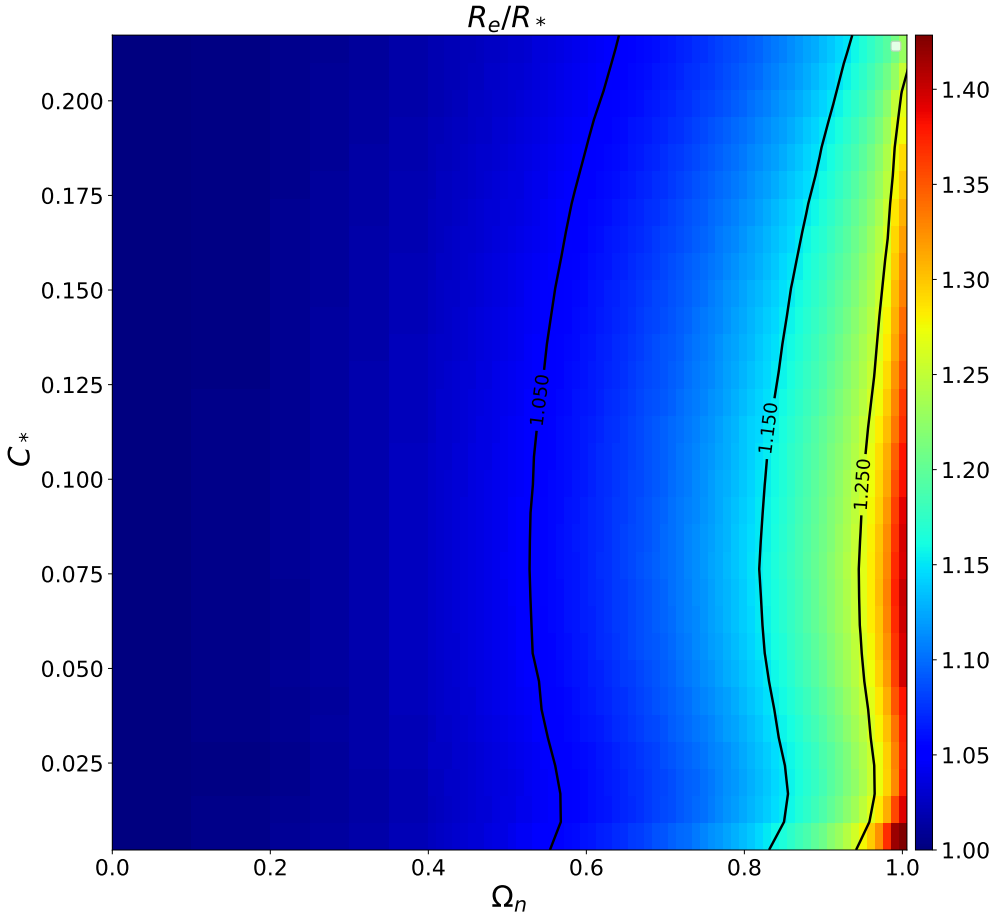

FIGURE 4.2.1: R_e/R_* vs C_* vs Ω_n. Each bin gives the mean value of the data within it. In figure B.0.2 we show the same plot but in 3 dimensions.

Based on Figure B.0.2 we can conclude that the change of the equatorial radius does not strongly depend on the choice of the EOS, therefore the equatorial radius spin corrections are universal for the neutron stars.

We saw that it is very difficult to predict the exact behavior of the R_e/R_* function at the Kepler limit. For this reason, in Figure 4.2.2 we find the best fit

equation of $\frac{R_e}{R_*}|_K$ with respect to C_*, where $\frac{R_e}{R_*}|_K$ is R_e/R_* at the Kepler limit

$$\frac{R}{R_*}|_K \approx -6706.60 \times C_*^5 + 4228.02 \times C_*^4 - 983.53 \times C_*^3 + 97.12 \times C_*^2 - 4.14 \times C_* + 1.48, \tag{4.2.3}$$

where the maximum deviation is 1.65% and $R^2 = 0.9820$.

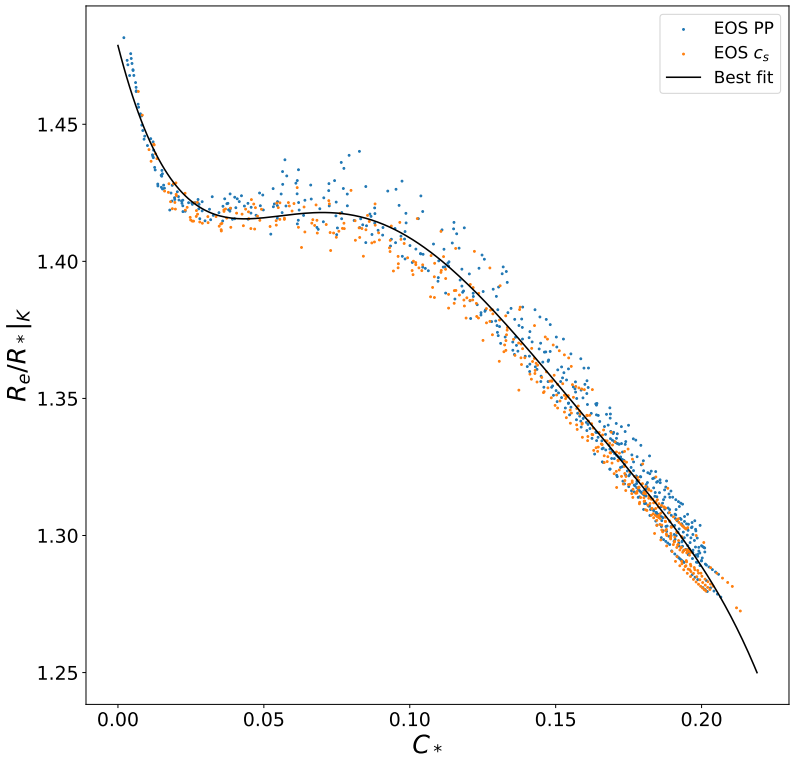

FIGURE 4.2.2: $\frac{R}{R_*}|_K$ vs C_*

4.3 Spin corrections for the compactness

In Figure 4.3.1 we show the dependence of the rotating star's compactness on Ω_n and C_*. Although the mass and radius of a rotating star can increase

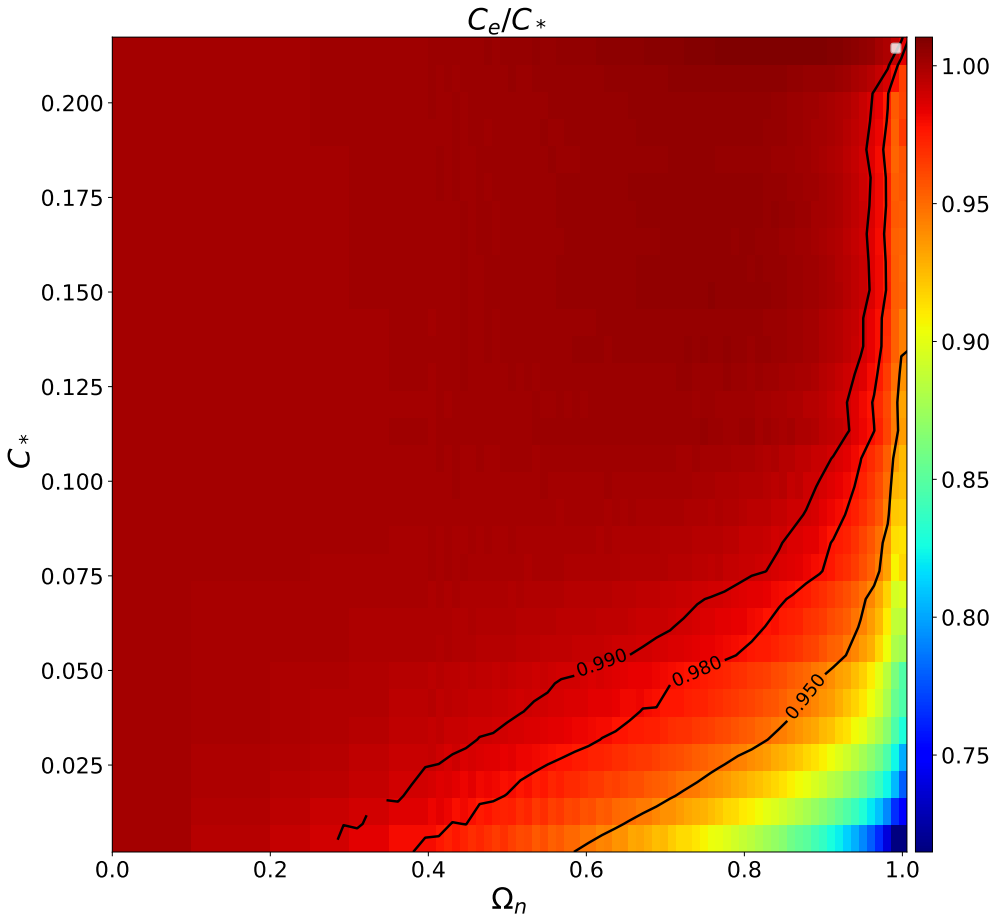

FIGURE 4.3.1: C_e/C_* vs C_* vs Ω_n. Each bin gives the mean value of the data within it. In figure B.0.3 we show C_e vs C_* vs Ω_n in 3 dimensions.

by as much as 20% due to rotation, the changes in the ratio of M/R_e due to rotation are an order of magnitude smaller. This figure shows that for more relativistic stars (larger values of C_e), the compactness is almost constant as the star spins faster.

Despite the fact that we can find the value of compactness by using the M/M_* and R_e/R_* best fit equations (we did that in Figure B.0.5), just for completeness here we introduce a different best fit equation for the equatorial compactness only. However, keep in mind that the compactness from the M/M_* and R_e/R_*

best fit equations give a smaller deviation, so this might be the better way to find C_e.

For the compactness approximation we use

$$C_e \approx C_* + ln(1 - (\frac{\Omega_n}{1.1})^3) \times (0.209 \times C_* - 3.4449 \times C_*^2 + 21.215 \times C_*^3 - 44.427 \times C_*^4), \tag{4.3.1}$$

with $R^2 = 0.9986$. In Figure 4.1.2 we can see that the deviation is less than 2.8% until $\Omega_n \approx 0.8\Omega_K$. This equation fails to describe our data close to the Kepler frequency as the deviation increases up to 10%. Figure 4.3.1 clearly shows that the data from all the EOSs lies on the same surface, independent of the EOS family.

The table A.0.5 gives some values (and their deviations) of M/M_*, R_e/R_* and C_e that are calculated using our best fit equations, for given values of C_* and Ω_n.

4.4 Comparison with other EOSs

Finally, we compute the deviation of our best fit surfaces from the mass and radius values for the tabulated set of hadronic and hybrid NS EOSs that were described in subsection 3.3.5 (shown in the right-hand side of Figure 4.1.2). It is clear that we have a similar behavior with the two EOS families, therefore our fits based on the 32 randomly generated EOS can be used to predict spin corrections for other hadronic and hybrid EOS. The only exception is that we have a larger deviation in the case where we use the hyperons EOS for the M/M_* best fit equation (this causes the red region in the Dev(M/M_*) plot). This comes from the fact that this EOS has a maximum mass $\approx 1.5\ M_\odot$ (very soft) and therefore this EOS is nonphysical. However, it shows again that the M/M_* depends on the stiffness/softness of the EOS.

Interestingly, our equations describing the spin corrections are not as good approximations for the quark star EOS. The QS agrees with our results at relatively high compactness values, but this is not true at smaller compactness

values. This makes sense, because as we get closer to high values of compactness, the NSs and QSs are closer to the point where they are unstable to collapse to form black holes, and from the no-hair theorem we expect that QSs and NSs will behave in the same way. The same result has been found for the I-Love-Q relations (Yagi & Yunes (2013)).

To be more specific, in the table 4.4.1 we give the value of Ω_n that represents the point where the deviation becomes larger than 5% for different compactness values.

TABLE 4.4.1: QS EOS deviation. Each value of Ω_n represents the point where the deviation becomes larger than 5%.

C_*	Ω_n for Dev(M/M_*)	Ω_n for Dev(R_e/R_*)	Ω_n for Dev(C_e)
0.17	0.83	0.97	0.91
0.12	0.62	0.76	0.75
0.046	0.45	0.61	0.60

Unfortunately, we don't have any "proper" plot to show our outcomes for the quark stars, since the accuracy of the RNS code is not as good as for hadronic or hybrid stars. Our results came from a few data sets that are accurate enough. This problem might come from the fact that these stars are self-bound. In the future someone should make changes to the RNS code in order to increase the accuracy for quark stars.

4.5 Find the non-rotating star with same central energy density

Ideally, we expect observational astronomers to be able to measure the mass, the equatorial radius, and the frequency of many NSs. At present, the few measurements of neutron star radius are not very precise. However, longer observations with present-day X-ray telescopes such as NICER will provide better precision for a few NS radii. Planned telescopes such as Strobe-X, eXTP, and Athena have the potential to determine the radii of many neutron stars.

In the previous sections, we provided best fit equations for M and R_e that depend on M_* and R_*. It is also interesting to construct an inverse map from a

rotating star's properties to the properties of a non-rotating star with the same central energy density. But we can not do that by using our previous best fit equations. We can create a similar set of equations for the non-rotating star's mass and radius by repeating the whole process, but now we change $R_* \to R_e$ and $M_* \to M$.
First of all we redefine the new normalized frequency as follows

$$\begin{aligned}\Omega_{K2}(empirical) \approx \sqrt{\frac{GM}{R_e^3}} \times (79.377 \times C_e^4 - 17.907 \times C_e^3 \\ -2.328 \times C_e^2 + 0.4183 \times C_e + 0.9933),\end{aligned} \tag{4.5.1}$$

$$\Omega_{n2} \approx \frac{\Omega}{\Omega_{K2}}, \tag{4.5.2}$$

with maximum deviation equals to 1.48% and $R^2 = 0.9121$. From Figure 4.5.1 it can be seen that when the mass and radius of the NS rotating at the Kepler frequency are used, the formula for the Kepler frequency is within a couple percent of the Newtonian formula.

For the M/M_* and R_e/R_* we use the following best fit equations

$$\begin{aligned}M/M_* \approx 1 + (\Omega_{n2} - 2.924 \times \Omega_{n2}^2 + 15.305 \times \Omega_{n2}^3 - 9.908 \times \Omega_{n2}^4) \\ \times (1.765 \times C_e - 10.985 \times C_e^2 + 11.069 \times C_e^3 + 34.996 \times C_e^4),\end{aligned} \tag{4.5.3}$$

$$\begin{aligned}R_e/R_* \approx 1 + (e^{0.39998 \times \Omega_{n2}^2} - 1 - 0.0058314 \times ln(1 - (\frac{\Omega_{n2}}{1.1})^4)^2) \\ \times (1 - 8.8981 \times C_e + 216.845 \times C_e^2 - 2298.43 \times C_e^3 \\ +10211.976 \times C_e^4 - 16587.60 \times C_e^5).\end{aligned} \tag{4.5.4}$$

Their R^2 is 0.9722 and 0.9980 respectively, and in Figure 4.5.2 we provide their deviations. Comparing figure 4.5.2 to figure 4.1.2, we can see that the R_e/R_* deviation decreases significantly when we change $R_* \to R_e$ and $M_* \to M$. It can be seen that in general the deviation is less than 1% and its maximum value is $\approx 1.8\%$. On the other hand, M/M_* deviation doesn't change significantly as we have a similar structure as before.

Imagine that a rotating neutron star's mass M, equatorial radius R_e, and angular velocity Ω are measured. Then the new normalized frequency Ω_{n2}

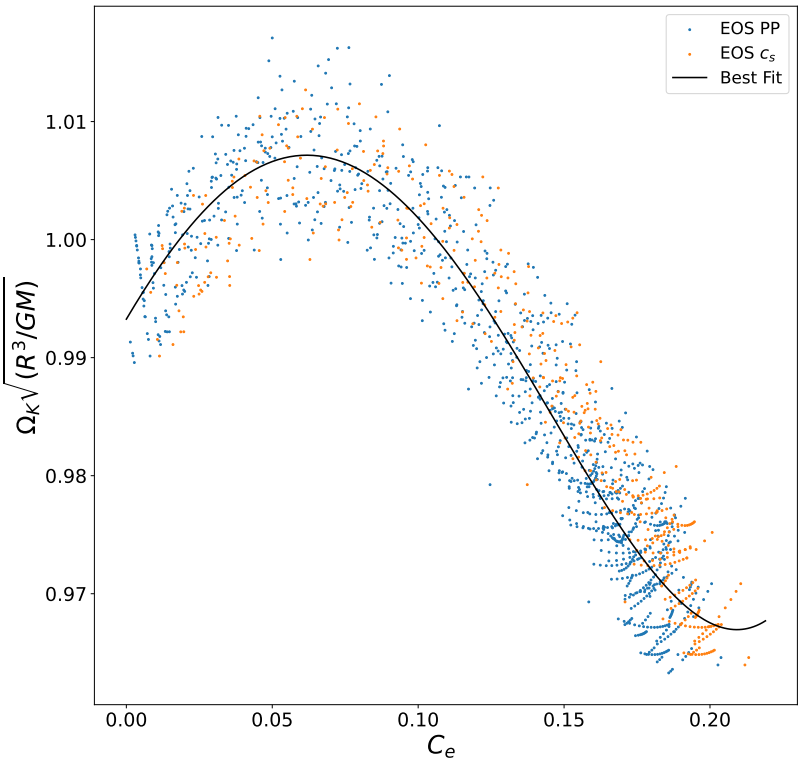

FIGURE 4.5.1: $\Omega_K/\sqrt{\frac{GM}{R_e^3}}$ vs C_e

and the equatorial compactness C_e can be calculated using equations 4.2.2 and 4.1.2. Equations 4.5.3 and 4.5.4 can then be used to solve for the corresponding non-rotating star's mass and radius.

In subsection 4.7.2 we show how these best fit equations can be useful in our observations of many different NS with different spin frequencies.

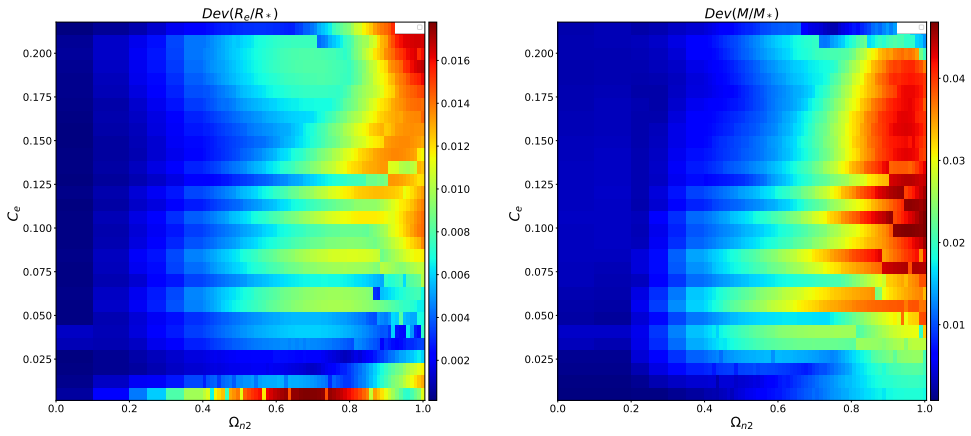

FIGURE 4.5.2: M/M_* and R_e/R_* deviation in a 2D histogram

4.6 Spin corrections for the R_{ratio}

The methods used to measure the equatorial radius of rotating neutron star are based on a previously found universal function for the oblate shape (Morsink et al. (2007)) that depends on the rotating star's mass and radius. We are curious to see if similar relations hold when the corresponding non-rotating star's mass and radius are used. For this reason, we are going to see how the R_{ratio} (the polar radius divided by the equatorial radius) changes with respect to the normalized frequency and the initial compactness.

Figure 4.6.1 shows that R_{ratio} is also universal. The following best fit equation can describe our data with a deviation less 2% for most of the frequencies

$$\begin{aligned} R_{ratio} = 1 + (-0.134 \times \Omega_n^2 + 0.0778 \times ln(1 - (\Omega_n/1.1)^2)) \\ \times (1 + 8.054 \times C_* - 27.495 \times C_*^2), \end{aligned} \tag{4.6.1}$$

where its R^2 is 0.9962.

This equation is useful because RNS code uses R_{ratio} for its calculations instead of the frequency. Therefore, based on this equation someone can understand what Ω_n and C_* represents an R_{ratio} value.

The R_{ratio} is the ratio of the isotropic radial coordinates. We also provide R_{ratio} in the case where we use the Schwarzschild-like radial coordinate (R_{ratio}_S). This parameter is useful for the reconstruction of the NS's shape. The best fit equation for R_{ratio}_S has the same structure as the R_{ratio} does, but with different coefficients

$$R_{ratio}\_S = 1 + (-0.137 \times \Omega_n^2 + 0.0771 \times ln(1 - (\Omega_n/1.1)^2)) \times (1 + 6.481 \times C_* - 28.830 \times C_*^2), \tag{4.6.2}$$

where its R^2 is 0.9950 and figure 4.6.1 gives its deviation. It is worth mentioning the similarity of the coefficients of equations 4.6.2 and 4.6.1. This means that the differences between the Rratio and the Rratio_S values are not extremely large.

We can conclude that the changes of the polar radius (and therefore the NS's shape) are universal and independent of the choice of the EOS.

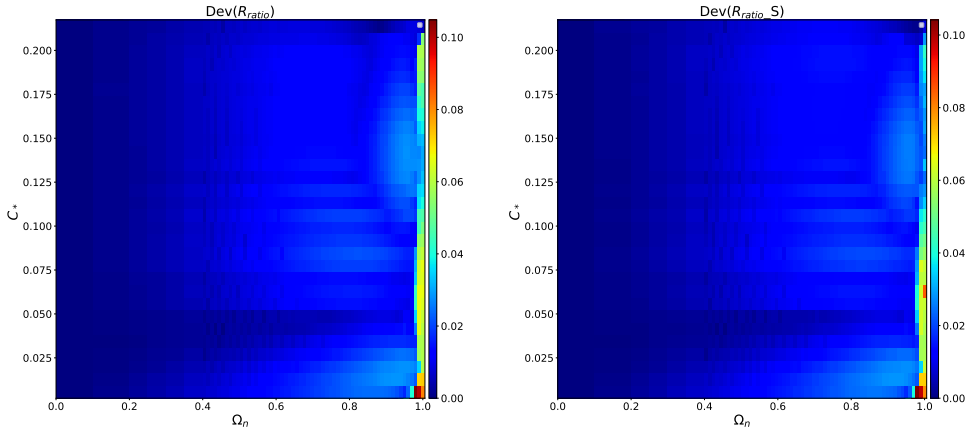

FIGURE 4.6.1: R_{ratio} and R_{ratio}_S deviation in a 2D histogram

4.7 Applications of our results

We now show how our results can be applicable to neutron star modeling and observations. Below, we show how we can recreate the shape of a NS, how

we can use our best fit equations for the rough estimation of the Mass-Radius curves of the rotating stars by starting from the non-rotating stars and vice versa.

4.7.1 From non-rotating to rotating NSs

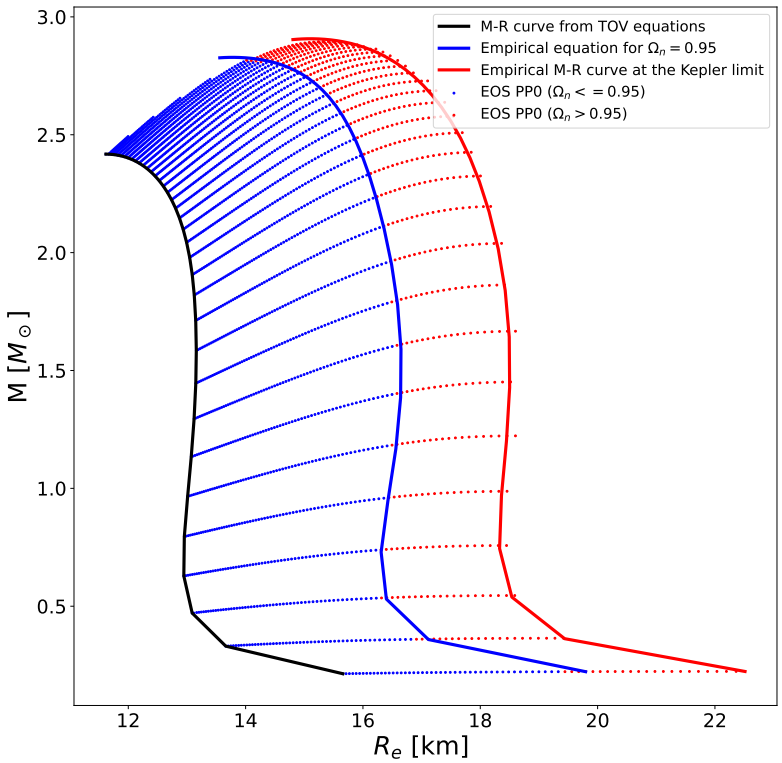

FIGURE 4.7.1: Total mass vs the equatorial radius

Given an EOS, all stable solutions of the TOV equations (the black solid curve shown in Figure 4.7.1) can be computed in a few minutes by the use of a simple code. However, running the RNS code and finding the parameters that define all stable rotating neutron stars (blue and red points on Figure 4.7.1), is more computationally expensive (a couple hours in our case). For this reason, in Figure 4.7.1 we used our best fit equations in order to recreate the region

that is covered in the Mass-Radius space by the rotation, for one example EOS PP0.

As an example for EOS PP0, we can calculate all of the NS spinning at 95% of the Kepler frequency using the two best fit equations 4.1.2 and 4.2.2, setting $\Omega_n = 0.95$. From the TOV solutions we get M_*, R_* and C_* for this EOS. Now, we have all the information that we need in order to recreate the Mass-Radius curve at $\Omega_n = 0.95$ (**Blue curve**). The **blue points** represent the RNS data for the case where $\Omega_n \leq 0.95$.

Unfortunately, we can not use the same best fit equations, in order to describe the regions after $\Omega_n = 0.95$, as the deviation is much larger at the Kepler limit. For this reason, we used the 4.2.3 and 4.1.3 best fit equations. The **red dashed curve** represents the Mass-Radius curve at the Kepler limit and the **red points** represent the RNS data for the case where $\Omega_n > 0.95$.

We can see that the data are in a good agreement with our empirical equations. Therefore someone can use our empirical equations in order to illustrate (immediately) the changes of the mass and the equatorial radius for a specific EOS, instead of using the RNS code. This will be useful in EOS inference codes that typically create and test thousands of EOSs.

4.7.2 From rotating to non-rotating NSs

Now we use 4.5.2, 4.5.4 and 4.5.3 equations in order to find the corresponding mass and radius of a non-rotating NS for given M, R_e and Ω. The blue dots in Figure 4.7.2 represent the masses and radii of rotating NS computed with the RNS code for EOS PP0. The black curve represents the M-R curve from the TOV equations. Each blue dot is mapped to a non-rotating NS (represented with an orange dot) using these equations. If the inverse mapping were perfect, all the blue points in a constant-density sequence would be mapped to the same point on the black curve. It can be seen that our approximation for M_* and R_* (orange dots) are very close to the M-R curve, with the thickness of the orange points representing the error introduced by the approximation. Therefore, by using the three best fit equations we can find the non-rotating star with the same

central energy density. This means that there is no reason for us to compute the values of the mass and the equatorial radius of the rotating neutron stars, as the change of these parameters is universal. As a result, in the future we can recreate the M-R curve by using observations of rotating stars.

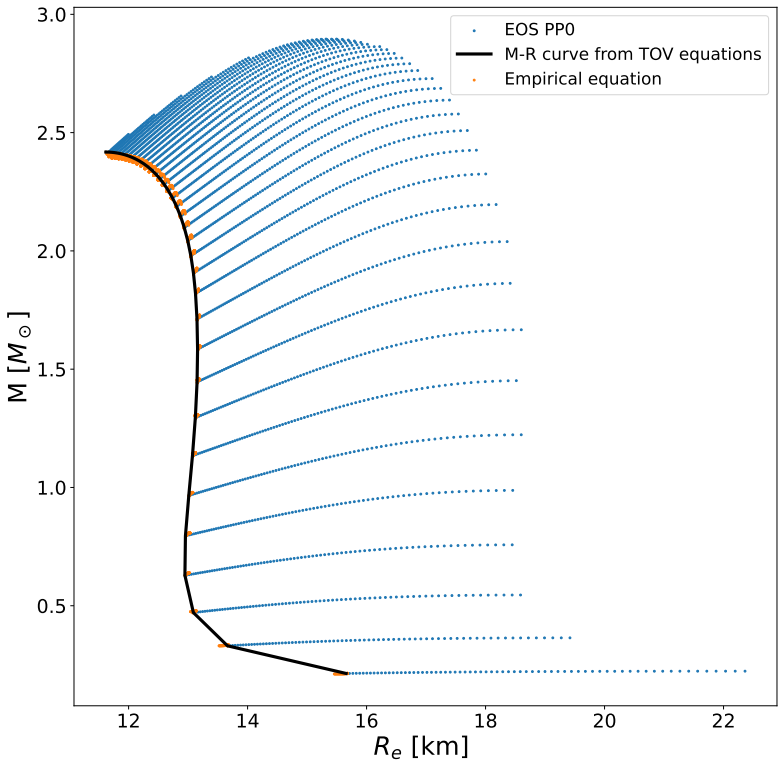

FIGURE 4.7.2: M/M_* vs R_e/R_*

4.7.2.1 Application to real data

Miller et al. (2019) and Riley et al. (2019) in their analysis of data that came from the NICER telescope regarding the millisecond pulsar PSR J0030+0451 (ν = 205.53 Hz), provided an estimation for pulsar's radius and mass.

Miller et al. (2019) suggested that M = $1.44^{+0.15}_{-0.14}$ $M_\odot$ and $R_e = 13.02^{+1.24}_{-1.06}$ km. We used our best fit equations from section 4.5, and find that $M_* = 1.43 M_\odot$ and $R_* = 12.94$ km without worrying about the statistical uncertainty.

It can be seen that the predicted change of the mass (M - $M_* = 0.1$ $M_\odot$) and radius (R_e - $R_* = 0.08$ km) are smaller compared to the error bars coming from these measurements. This means that our spin corrections are going to be useful for this star in the case where the observational uncertainty in mass and radius is less is less than 0.1 $M_\odot$ and 0.08 km, respectively.

By using equations 4.2.2 and 4.1.2, and assuming that $M_* = 1.43 M_\odot$ and $R_* = 12.94$ km, we could find at which value of the frequency, mass and radius changes are larger than these error bars. We find out that the change of mass and radius is simultaneously larger than 0.15 $M_\odot$ and 1.24 km respectively, when $\nu \gtrapprox 740$ Hz.

Riley et al. (2019), based on their analysis, suggested that M = $1.34^{+0.15}_{-0.16}$ $M_\odot$ and $R_e = 12.71^{+1.14}_{-1.19}$ km. Following the same process as before we found very similar values for the change of the mass and radius. In this case they are simultaneously larger than 0.16 $M_\odot$ and 1.19 km respectively, when $\nu \gtrapprox 775$ Hz.

4.7.3 Neutron star shape

In order to reconstruct the shape of the NS we can use the best fit equations for R_e/R_* and $R_{ratio}_$S. This can happen by using the equation of an ellipse as follows

$$\frac{z^2}{R_{pole}^2} + \frac{x^2}{R_{equator}^2} = \frac{1}{R_{equator}^2}\left(\frac{z^2}{R_{ratio}\_S^2} + x^2\right) = 1. \tag{4.7.1}$$

In figure 4.7.3 we recreate the NSs shape by our results. The dots represent the surface that RNS code created and the solid lines represent our attempt. It can be seen that our approximation works until the frequency of the NS gets close to the 90% Ω_k (the red line). Beyond this point, even if our values for the equatorial and polar radius are very close to the RNS values, the shape of the NSs is not an ellipse anymore.

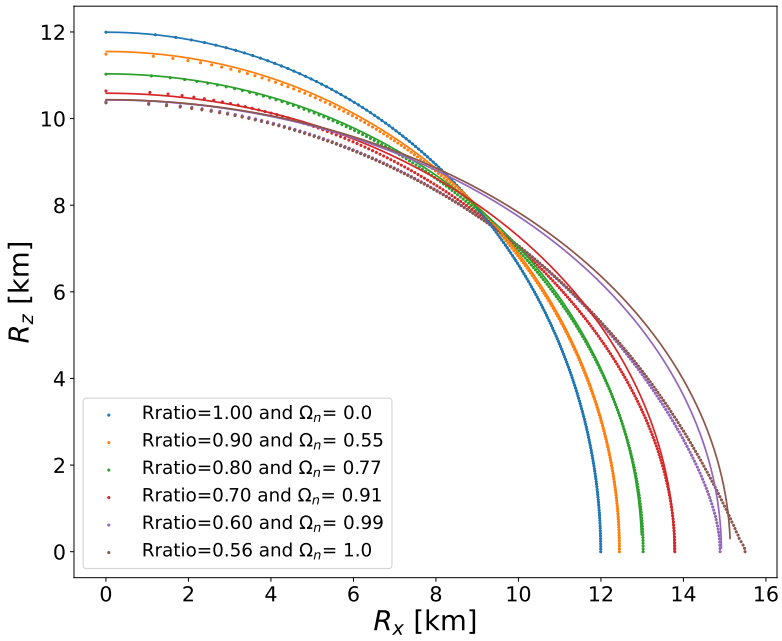

FIGURE 4.7.3: Neutron star's shape

4.8 Motivation for future work

In the previous sections we mainly discussed how mass and equatorial radius change with respect to the rotational frequency in a sequence. We did that because these three quantities are the ones that can be measured by observation. Parameters like the rotational kinetic energy or the gravitational binding energy of the system, even if they can be helpful to understand the fundamental properties of the star, can not be measured experimentally. The purpose of this section is to give some other interesting plots that we got but we didn't have the time to deeply investigate them. Therefore, here we provide some possible directions for future work.

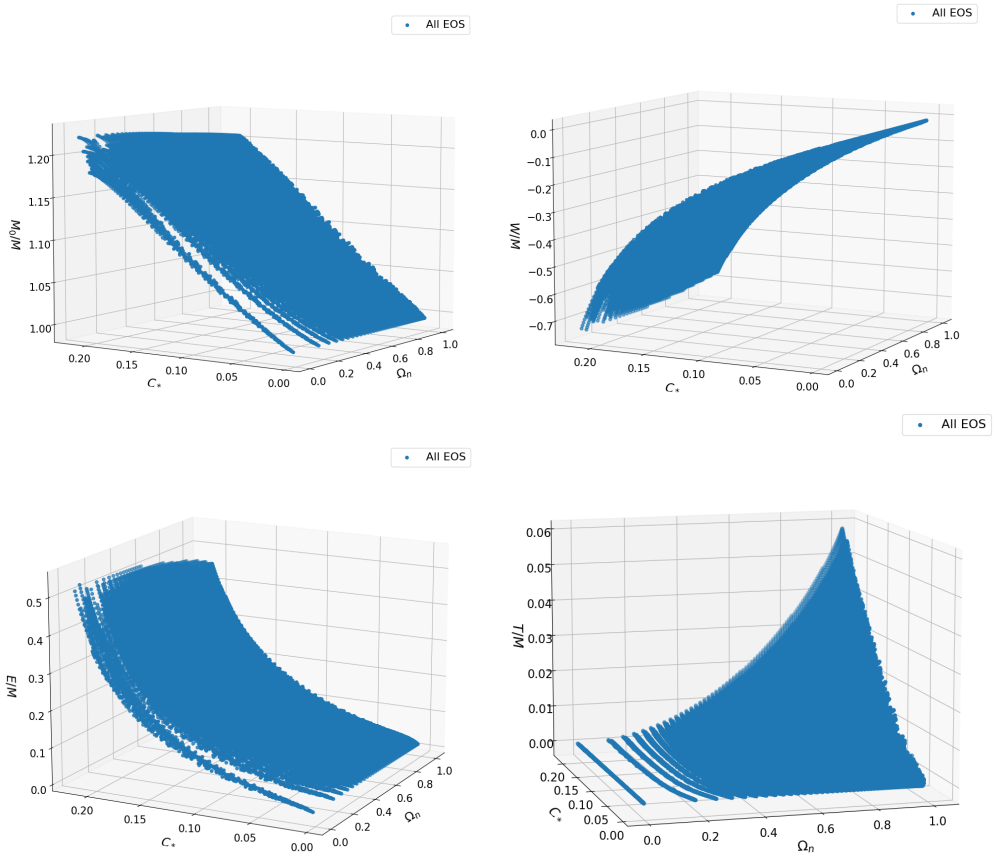

FIGURE 4.8.1: Normalized energies vs C_* vs Ω_n

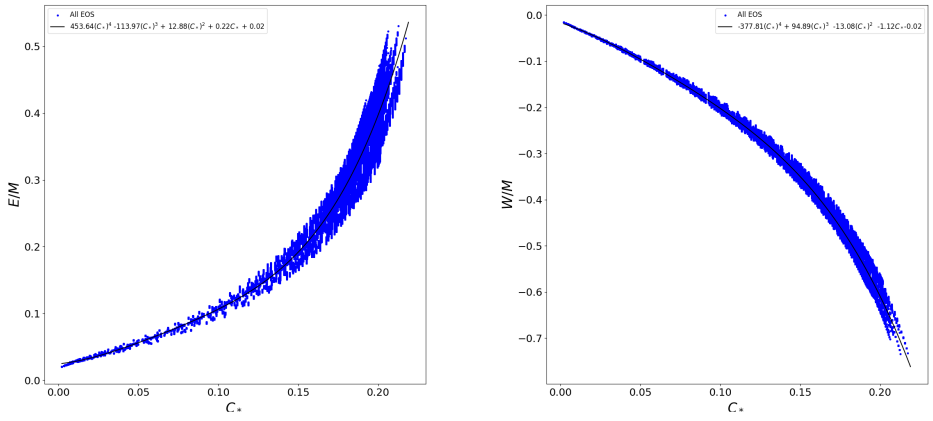

FIGURE 4.8.2: $\frac{E}{M}$ and $\frac{W}{M}$ vs C_*

4.8.1 Energy changes

In order to have a better understanding of the mass universality we could investigate how the baryon mass M_0 the internal energy E, the gravitational energy and the rotational kinetic energy of the system change as the frequency increases. For a better investigation of each component we show how $\frac{M_0}{M}$, $\frac{W}{M}$, $\frac{T}{M}$ and $\frac{E}{M}$ change with respect to Ω_n and C_*. Figures 4.8.1 illustrate the behavior of these parameters.

First of all, the $\frac{M_0}{M}$ changes with the same way as the binding energy does (we don't provide the binding energy plot here).
Furthermore, it is worth mentioning that the value of the kinetic energy is one order of magnitude less than the value of the gravitational binding energy. This is something that was expected, since the energy that keeps the system gravitationally bound should be much larger than the kinetic energy.

Moreover, $\frac{W}{M}$ and $\frac{E}{M}$ have a similar behavior, with the difference that $\frac{W}{M}$ takes negative values. Here, we provide a best fit equation for $\frac{W}{M}$ and $\frac{E}{M}$ vs C_* with maximum deviation equal to 21.37% and 24.00% respectively. Their dependency on frequency can be investigated in future.

4.9 Summary of this chapter

We showed that the change of the mass and the equatorial radius of a neutron star due to the spin rotation is universal. We provided two best fit equations that can predict their values very well up to about 95% of the Kepler frequency. Beyond this point we just provide the M/M_* and R_e/R_* values at the Kepler limit. These best fit equations are very useful as they can be used to calculate approximately the region in the Mass - Radius space that is covered by the rotating NSs, in just a few seconds.

We also showed that it is possible to find the non-rotating neutron star with the same central energy density, for given M, R_e and Ω. This means that we don't expect to learn something new about the structure of the EOS by studying

the change of the mass and radius of the RNSs. All the information that we need will come from the M-R curve at the non-rotating limit.

The tables A.0.6 and A.0.7 summarize all the new best fit equations that we suggest.

Chapter 5

R_e/R_*, M/M_* and C_e universality explained

The fact that these three parameters are universal, (at least up to $\Omega_n < 0.95\Omega_K$) seems to be very interesting. The last and most important question that we have to answer is "Why is this happening?".

5.1 Newtonian explanation

5.1.1 R_e/R_* universality due to low density region similarity

A simple Newtonian model that can help us to understand the universality of R_e/R_* is the horizontal spring which has one end attached on the wall (Figure 5.1.1 upper part). This spring has the following interesting property: the most of its part has a spring constant K1 and the rest (that is not attached on the wall) has a spring constant K2. K1 is much larger than K2 ($K2 << K1$). The first part is called "the high density region" and the second part is called "the low density region". In this case, the spring force is in equilibrium. If we try to push the spring towards the wall the spring will push us back to the equilibrium point. In the NS case this models the pressure from the degenerate neutrons

and the nuclear forces that are going to push back. If we try to pull it away from the wall, the spring again will pull us back to the equilibrium point. In the NS case the gravity is providing the restoring force.

Now, if we pull the spring outwards with a force F, with F playing the role of the centrifugal force in the NS case, the expansion of the spring will mainly depend on the value of the softer spring's spring constant, K2, since $K_{eff} = \frac{K1K2}{K1+K2} \rightarrow K2$, when $K2 << K1$.

Therefore, suppose we have a number of similar spring systems, each with a different stiff spring constants K1, but the same soft spring constant K2. In all of these systems the effective spring constant and the displacement (or increase in equatorial radius) will only depend on the softer spring. This leads to a type of universal displacement that does not depend strongly on the properties of the stiffer spring.

Another way of thinking about this universality is by re-thinking the problem at the extreme case scenario. For example, lets assume that the high density region was a large concrete sphere and the low density region was full of water (Figure 5.1.1 bottom). If there is no rotation, an element on the low density region is going to feel the gravitational force from the material below it (F_G) and the pressure from its surroundings (P(r) and P(r+dr)) . As we rotate the star, we have to take into account the centrifugal force (F_C). As none of the forces depend on the composition of the high density region, we can understand that the equatorial radius depends mainly on the changes of the low density region. Gravity depends on the value of the mass of the high density region, not on its composition.

The randomly generated EOS and the tabulated hadronic and hybrid EOS span a wide range of different properties in their core. But they are all matched to softer, more easily compressed EOS in their crusts. Since the physics of the crust is fairly well constrained by experiments, there is not much variation in the different crust EOS. The result is that the similar crusts for these stars lead to overall radial deformations that are very similar, regardless of the EOS in the core. The one notable exception is the bare quark EOS which does not have a hadronic crust, and is not as accurately described by our formula for the increase in radius due to rotation.

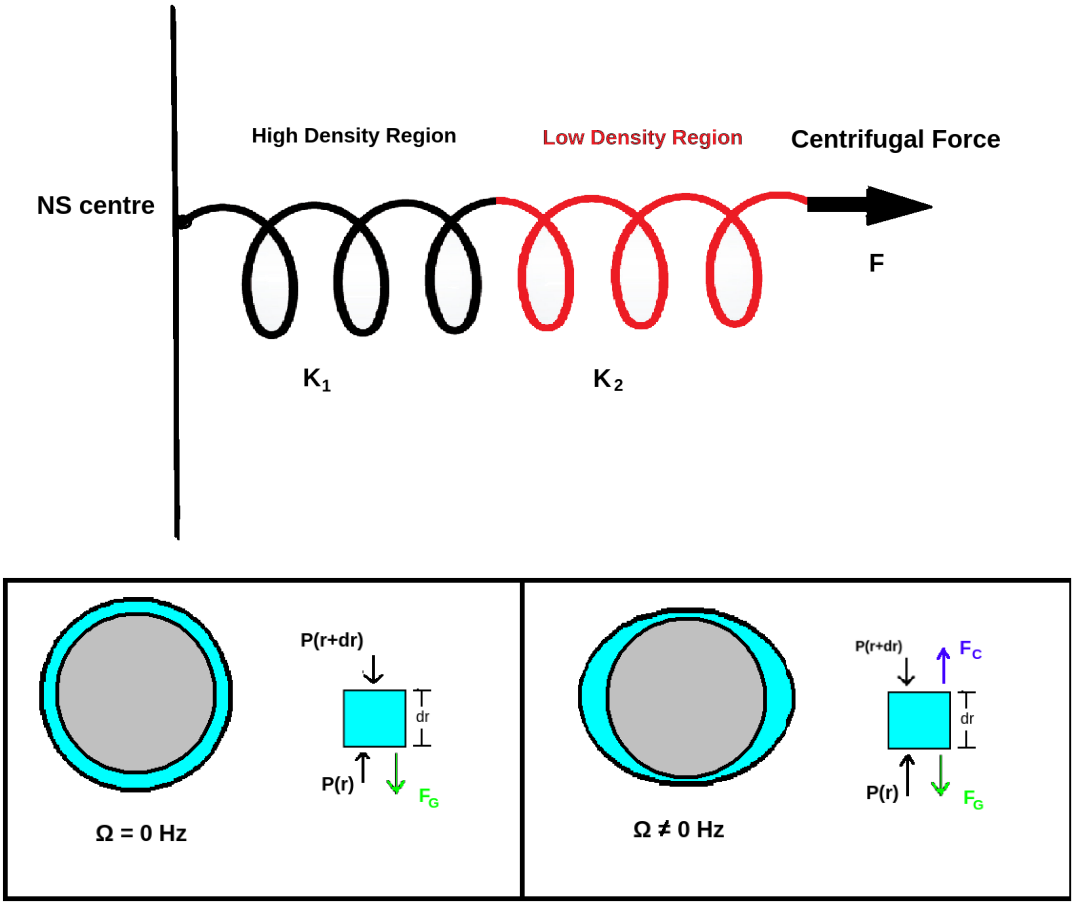

FIGURE 5.1.1: Newtonian approach

5.1.2 Mass change is proportional to the equatorial radius change (uniform density)

Now, let's assume that we have a NS with uniform constant mass density $\rho_{uniform}$. Its mass is going to be equal to $\rho_{uniform} \times V$, where V is the volume. When $\Omega = 0$ Hz, $M = \rho_{uniform} \times \frac{4\pi R^3}{3}$. We saw before that until 90% of the Kepler frequency the shape of the NS is an ellipsoid. Therefore, when $\Omega > 0$ Hz, $M = \rho_{uniform} \times \frac{4\pi R_e^2 R_p}{3}$. In Figure 4.7.3 it appears that the increase in equatorial radius is close to balanced by the decrease in the polar radius for spins up to about 0.9 Ω_K.

If the increase in equatorial radius and decrease in polar radius are exactly balanced, then these radii are $R_e = R_*(1+\alpha(\Omega))$ and $R_p = R_*(1-\alpha(\Omega))$, and the quantity $R_e + R_p = 2R_*$.

In Figure 5.1.2 the fraction $\frac{|2R_*-R_p-R_e|}{2R_*}$ is shown as a function of Ω_n and C_*. In this Figure the value of $\frac{|2R_*-R_p-R_e|}{2R_*}$ represents the relative difference in how the equatorial and polar radii change with spin. The colours show the largest value of the ratio for any of the EOS. It can be seen that up to 70% Ω_k the changes are less than 2.5%, and become significant at higher frequencies. This change is universal, and applies for all the EOSs.

So, if we say that $R_e = R_*(1+\alpha(\Omega))$ and $R_p = R_*(1-\alpha(\Omega))$, where $\alpha(\Omega)$ is a function of frequency and represents the change of the equatorial radius, then we have that

$$M = \frac{4\pi\rho_{uniform}}{3}R_e^2 R_p = \frac{4\pi\rho_{uniform}R_*^2}{3}(1-\alpha(\Omega)^2)R_e. \tag{5.1.1}$$

For $\alpha(\Omega) \leq 0.1$, which stands for a change less than 10%, $0.99 \leq (1-\alpha(\Omega)^2) \leq 1$. As a result, we can say that $(1-\alpha(\Omega)^2) \approx 1$ for $\alpha(\Omega) \leq 0.1$. Interestingly, we can see from Figure 4.2.1 that a 10% change to the equatorial radius is very close to the 80% Ω_k. This means that the mass changes same way as R_e changes, up to very high spins, since

$$M \approx \frac{4\pi\rho_{uniform}R_*^2}{3}R_e. \tag{5.1.2}$$

Based on this, we expect that the volume and therefore the mass are going to be proportional to the equatorial radius, since R_e and R_p will cancel each other in the volume equation. This explains the mass and the compactness universality.

5.1.3 Mass change is proportional to the equatorial radius change (non-uniform density)

We can show that the same proportionality holds in the case where we don't have a constant and uniform density profile. To show this, we assumed that

when the central density (ρ_{center}) is the maximum density, the density profile behaves as follows

$$\rho = \rho_{center}[1 - f(\sqrt{x^2/R_e^2 + y^2/R_e^2 + z^2/R_p^2})], \tag{5.1.3}$$

where $f(\sqrt{x^2/R_e^2 + y^2/R_e^2 + z^2/R_p^2})$ is a function that is zero at the center, and 1 on the surface. The $\sqrt{x^2/R_e^2 + y^2/R_e^2 + z^2/R_p^2}$ dependency represents the distance from the center of the ellipse to the surface of the star. We can integrate within the ellipsoid volume and find the mass of the star

$$\begin{aligned} M = \rho_{center} \int_{-R_e}^{R_e} \int_{-R_e\sqrt{1-\frac{x^2}{R_e^2}}}^{R_e\sqrt{1-\frac{x^2}{R_e^2}}} \int_{-R_p\sqrt{1-\frac{x^2}{R_e^2}-\frac{y^2}{R_e^2}}}^{R_p\sqrt{1-\frac{x^2}{R_e^2}-\frac{y^2}{R_e^2}}} \\ [1 - f(\sqrt{x^2/R_e^2 + y^2/R_e^2 + z^2/R_p^2})]dxdydz. \end{aligned} \tag{5.1.4}$$

We can set $\frac{x}{R_e}$ = u, $\frac{y}{R_e}$ = v and $\frac{z}{R_p}$ = w and rewrite the equation above as

$$M = \rho_{center} R_e^2 R_p [\frac{4\pi}{3} - I] \approx \rho_{center} R_*^2 R_e [\frac{4\pi}{3} - I], \tag{5.1.5}$$

where I=$\int_{-1}^{1} \int_{-\sqrt{1-u^2}}^{\sqrt{1-u^2}} \int_{-\sqrt{1-u^2-v^2}}^{\sqrt{1-u^2-v^2}} [f(\sqrt{u^2+v^2+w^2})]dudvdw$ and is going to be a number.

We can see again that the mass is proportional to the change of the equatorial radius, if R_p and R_e change in the same way. Furthermore, we can see that C_e is strongly related to the value of the central energy density as

$$C_e \approx \rho_{center} R_*^2 [\frac{4\pi}{3} - I]. \tag{5.1.6}$$

5.1.4 R_p and R_e changes

We made the assumption before that for $R_e = R_*(1+\alpha_e(\Omega))$ and $R_p = R_*(1-\alpha_p(\Omega))$, then $\alpha_e(\Omega) \approx \alpha_p(\Omega)$=$\alpha(\Omega)$. We showed that this is true empirically by using the Figure 5.1.2.

Interestingly, we can show that this assumption is valid by using the ellipse equation.

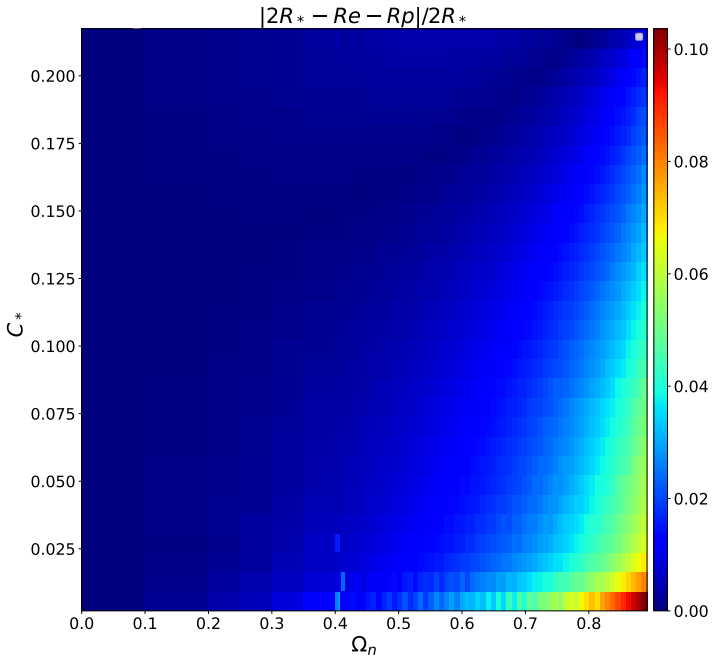

FIGURE 5.1.2: Equatorial and polar radius changes

When the NS doesn't rotate, the equation that describes its shape on the x-z plane is

$$x^2 + z^2 = R_*^2. \tag{5.1.7}$$

In the case where the star rotates we use the equation of an ellipse

$$x^2/R_e^2 + z^2/R_p^2 = 1. \tag{5.1.8}$$

In the previous chapter (Figure 4.7.3) we showed how the shape of a NS changes for a specific EOS. It can be seen that when $R_x \approx 9.3$ km, equations 5.1.7 and 5.1.8 have a common point. The magnitude of the distance of this point from the center of the axis is R_*, as this point belongs to the non-rotating NS too. Therefore, we can say that the coordinates that describe this point are (R_* $\cos(\theta_c)$,R_* $\sin(\theta_c)$), where θ_c is the angle of this crossover from the x-axis.

Replacing this point on equation 5.1.8, and using that $R_e = R_*(1 + \alpha_e(\Omega))$ and $R_p = R_*(1 - \alpha_p(\Omega))$, we have that

$$\alpha_e = \frac{cos(\theta_c)}{\sqrt{1 - \frac{sin^2(\theta_c)}{(1-\alpha_p)^2}}} - 1. \tag{5.1.9}$$

From the Figure 4.7.3 we find out that $\theta_c(R_{ratio} = 0.9) = 40.71°$, and $\theta_c(R_{ratio} = 0.8) = 40.03°$.
Using equation 5.1.9, $\theta_c = 40.71°$, and that $R_{ratio} = \frac{1-\alpha_p}{1+\alpha_e} = 0.9$, we get that

$$\alpha_e + 1 = \frac{0.758}{\sqrt{1 - \frac{0.525}{(1+\alpha_e)^2}}}. \tag{5.1.10}$$

As a result, we get that α_e=0.0487 and α_p=0.05617, which leads to $(1+\alpha_e)(1-\alpha_p) = 0.99$.

Using equation 5.1.9, $\theta_c = 40.03°$, and that $R_{ratio} = \frac{1-\alpha_p}{1+\alpha_e} = 0.8$, we get that α_e=0.110 and α_p=0.112, which leads to $(1 + \alpha_e)(1 - \alpha_p) = 0.986$. This means that the assumption that $(1 + \alpha_e)(1 - \alpha_p) \approx 1$ is acceptable up to this point.

5.1.5 Summary of this subsection

All in all, we showed that the change of the equatorial radius is universal, as it strongly depends on the properties of the low density region.

Furthermore, we showed that the change of the equatorial radius increases approximately with the same way as the polar radius decreases. This leads to the conclusion that mass is proportional to the equatorial radius

$$M \propto R_e, \tag{5.1.11}$$

and the compactness is strongly related to the value of the central density

5.2 GR explanation

To answer the same question in general relativity we have to go back to chapter 2, and remember that the total mass and the equatorial radius depend on ϵ, P, velocity and on the metric potentials. Here, we investigate the way that these parameters change, just for one EOS (EOS PP0 (e_c = 1.70954)). We choose this central energy density in order to be sure that the stars in the sequence are stable to quasi-radial perturbations.

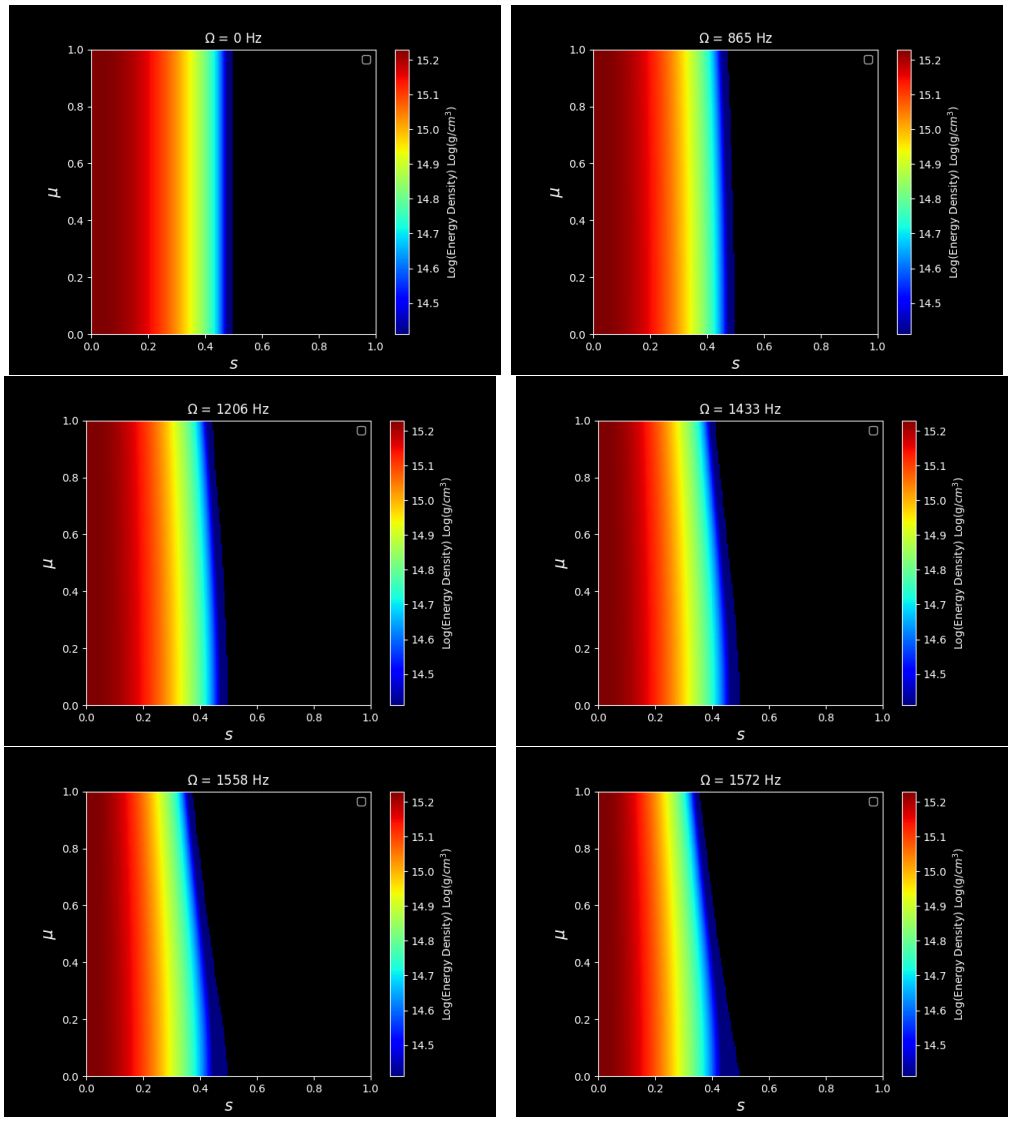

FIGURE 5.2.1: Energy density profile

Figures 5.2.1 and 5.2.2 show how the logarithm of the energy density and the normalized speed v/c change with respect to s and μ. $\Omega = 0Hz$ (R_{ratio}=1) corresponds to the first non-rotating star in the sequence. $\Omega = 865Hz$ (R_{ratio}=0.90) is a star with a frequency close to $\Omega \approx 0.5\Omega_K$, and $\Omega = 1206Hz$ (R_{ratio}=0.80) is a star with a frequency close to $\Omega \approx 0.7\Omega_K$. R_{ratio}=0.80 is also the point where our best fit equations start to diverge significantly from our data. $\Omega = 1433Hz$ and $\Omega = 1558Hz$ represent two NSs with R_{ratio} equal to 0.7 and 0.6 respectively. $\Omega = 1572Hz$ (R_{ratio}=0.56) corresponds to a frequency a little bit smaller than the Kepler frequency. This means that the star is at the point just before it becomes unstable.

We see in these figures that we have a very similar behavior for P, ϵ and h. For this reason, we are going to focus only on the energy density profile, but the same properties stand for the pressure and enthalpy.

For all the cases we can see that ϵ is larger at the center and decreases as we get closer to the surface.
For the case where Ratio=1 it is clear that ϵ is independent of the angle choice. This meets our expectations, since for a non-rotating neutron star we have spherical symmetry. We can see a small angle dependency when R_{ratio} becomes 0.90, but we can still say that the star is approximately spherical. The change of the angle seems to become significant close to the surface, when R_{ratio} becomes larger than 0.8.

The velocity profile is initially zero everywhere (as was expected). As the frequency in the sequence increases, the value of v increases. It can be seen that the material close to the equator moves faster than at other latitudes. Furthermore, v remains almost zero at the center and on the poles of the star.

A possible way to see how the metric potentials change, is by creating 3d plots for their values with respect to s and μ. However, as it can be seen from figure 5.2.3 that the 3d graph has a "lasagna" form, so it is not clear how potentials change. Instead of that, we plot the potentials with respect to s. We can not do the same for μ, as the potentials overlap. Fortunately, we can see the angle dependency of the potentials through the surface that is been formed in the potential-s plane. In figure 5.2.4, we can see that for all the potentials λ, γ, α and ω the μ dependence increases with the frequency. This can be seen

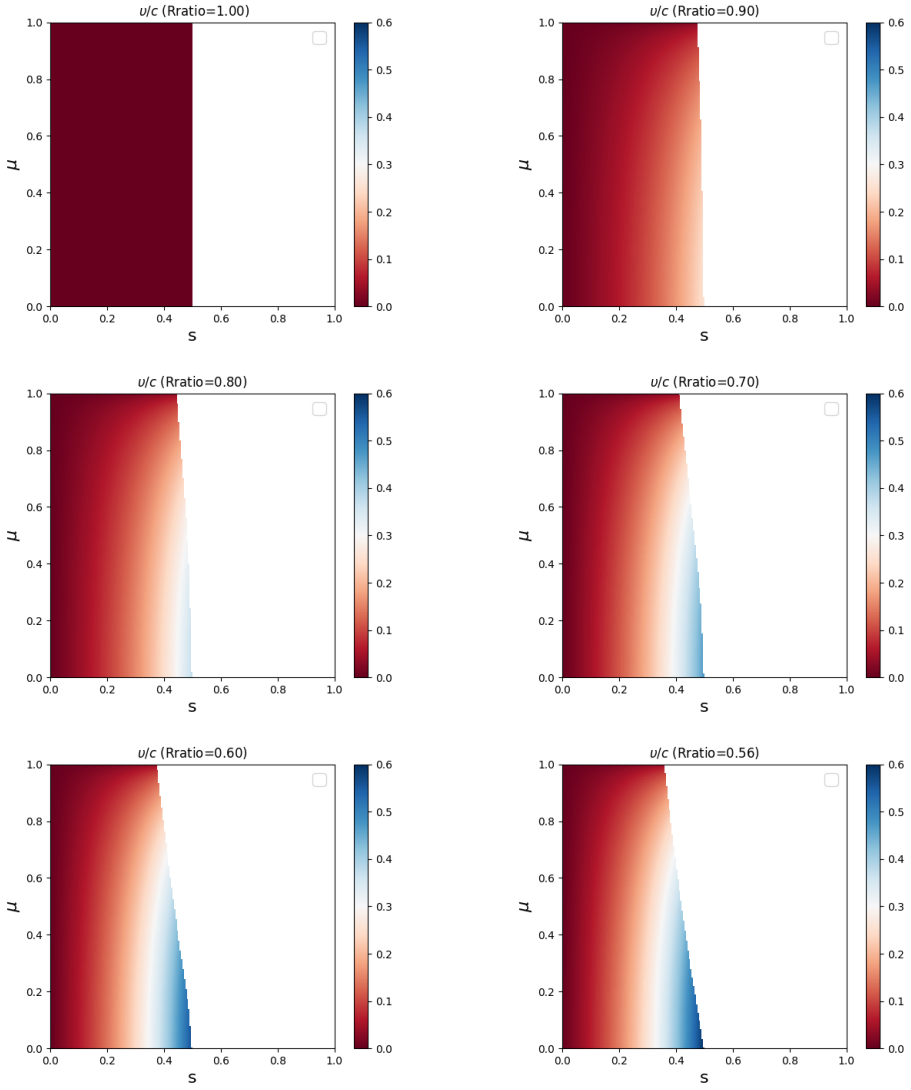

FIGURE 5.2.2: Velocity profile

from the change of the line thickness. The thickness becomes significant after the R_{ratio}=0.8 star.

Interestingly, we can see a very small change to the values of the λ, γ and α potentials for $0.8 \leq R_{ratio} \leq 1$. When R_{ratio} becomes larger than 0.8 we can see that their value change significantly. This is obvious if we compare the difference of the blue and orange line with the difference of the red and purple line.

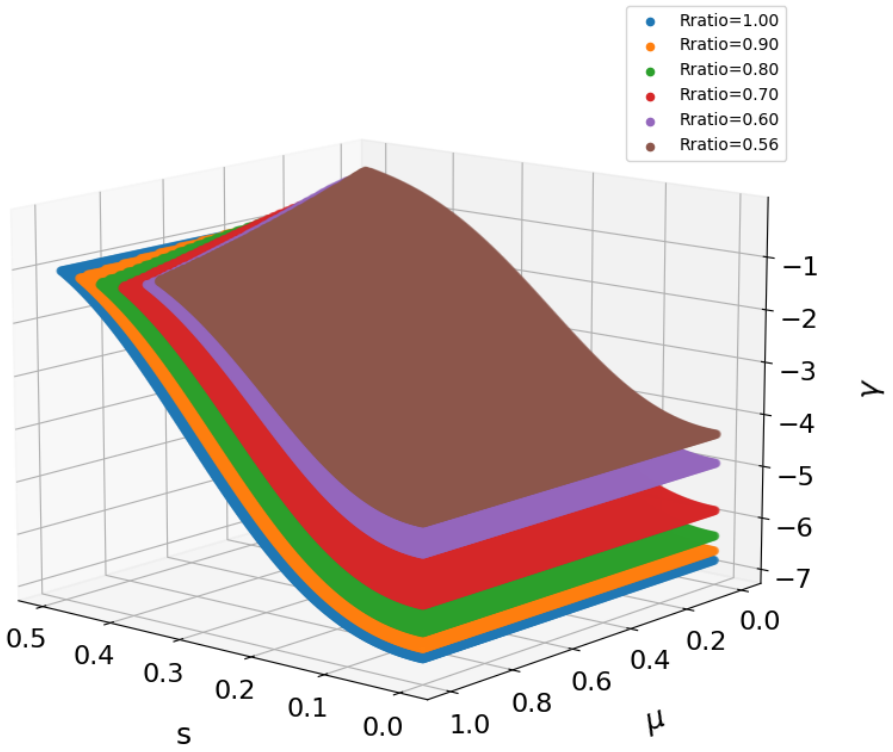

FIGURE 5.2.3: γ vs μ vs s

Now, let's see why the M/M_*, R_e/R_* and C_e are universal parameters. Let's start with M/M_*. Remember that:

$$M = \frac{4\pi\kappa^{1/2}c^2\bar{\mathrm{r}}_e^3}{G}\int_0^1 \frac{s^2ds}{(1-s)^4}\int_0^1 d\mu e^{2\alpha+\gamma}\{\frac{\bar{\epsilon}+\overline{\mathrm{P}}}{1-\upsilon^2} \\ [1+\upsilon^2+\frac{2s\upsilon}{1-s}(1-\mu^2)^{1/2}\hat{\omega}e^{-\lambda}]+2\overline{\mathrm{P}}\} \tag{5.2.1}$$

M_* is the total mass of the first star in a sequence. We said before that this star is a non-rotating star, therefore υ must be zero, so

$$M_* = \frac{4\pi\kappa^{1/2}c^2\bar{\mathrm{r}}_{e0}^3}{G}\int_0^1 \frac{s_0^2ds_0}{(1-s_0)^4}\int_0^1 d\mu_0 e^{2\alpha_0+\gamma_0}\{(\bar{\epsilon}_0+\overline{\mathrm{P}}_0)+2\overline{\mathrm{P}}_0\}. \tag{5.2.2}$$

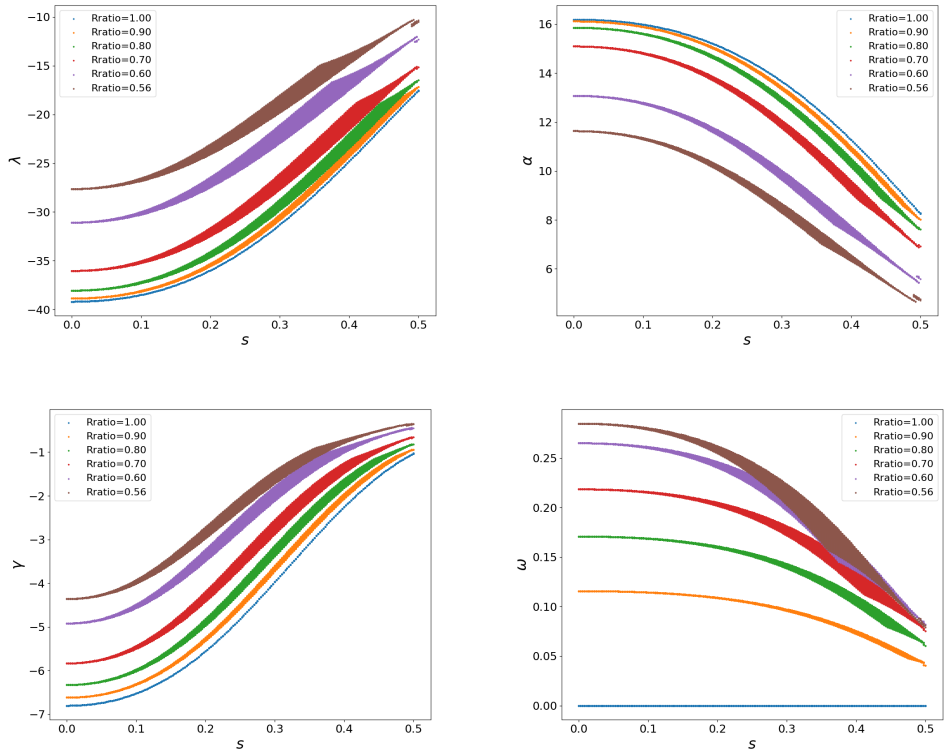

FIGURE 5.2.4: Metric potentials vs s

The zero number next to each parameter shows that we use the values for a non-rotating star. We write M/M_* as follows

$$M/M_* = \frac{\bar{\mathrm{r}}_e^3}{\bar{\mathrm{r}}_{e0}^3}[I_1 + I_2], \tag{5.2.3}$$

where

$$I_1 = \frac{\int dS \int_0^1 d\mu e^{2\alpha+\gamma}(\bar{\epsilon} + \overline{\mathrm{P}})\frac{1+v^2}{1-v^2} + 2\overline{\mathrm{P}}}{\int dS_0 \int_0^1 d\mu_0 e^{2\alpha_0+\gamma_0}\{(\bar{\epsilon}_0 + \overline{\mathrm{P}}_0) + 2\overline{\mathrm{P}}_0\}}, \tag{5.2.4}$$

$$I_2 = \frac{\int dS' \int_0^1 d\mu e^{2\alpha+\gamma}(\bar{\epsilon} + \overline{\mathrm{P}})\frac{2v}{1-v^2}(1-\mu^2)^{1/2}\hat{\omega}e^{-\lambda}}{\int dS_0 \int_0^1 d\mu_0 e^{2\alpha_0+\gamma_0}\{(\bar{\epsilon}_0 + \overline{\mathrm{P}}_0) + 2\overline{\mathrm{P}}_0\}}, \tag{5.2.5}$$

and $\int dS = \int_0^1 \frac{s^2 ds}{(1-s)^4}$ and $\int dS' = \int_0^1 \frac{s^3 ds}{(1-s)^5}$

It can be seen that the quantity I_2 is strongly related to the rotational kinetic energy of the system. Figure 4.8.1 shows that T is an order of magnitude less than the total mass. For this reason, we are going to focus only on the change of quantity I_1.

We saw in the previous subsection that the $\bar{\epsilon}$, $\overline{\mathrm{P}}$, α, γ and υ change significantly when the frequency in a sequence becomes larger than 70% Ω_K. Therefore, the properties of the EOS that can affect the I_1 numerator will be almost cancel out from the denominator. This makes I_1 a universal quantity for the NSs.

Now, let's see why $\frac{\bar{\mathrm{r}}_e^3}{\bar{\mathrm{r}}_{e0}^3}$ is also universal. To give an answer to that we have to take a look to the hydrostatic equilibrium equation on the surface. For a non-rotating NS we have

$$\frac{dP}{dr}|_{r_e} = -\frac{G(\epsilon(r_e)c^2 + P(r_e))(m(r_e) + 4\pi r_e^3 P(r_e)/c^2)}{rc^2[r - 2Gm(r_e)/c^2]}. \tag{5.2.6}$$

But $P(r_e)$ and $\epsilon(r_e)$ are simply the crust values of P and ϵ

$$\frac{dP_{crust}}{dr}|_{r_e} = -\frac{G(\epsilon_{crust}(r_e)c^2 + P_{crust}(r_e))(m(r_e) + 4\pi r_e^3 P_{crust}(r_e)/c^2)}{rc^2[r - 2Gm(r_e)/c^2]}. \tag{5.2.7}$$

As the crust is similar (and in some case the same) for different EOSs, the equatorial radius depends only on the mass that is included on a spherical radius r_e. The same thing stands for the case where the star rotates. By using equation 2.4.20 at the equator we have

$$h(\overline{\mathrm{P}}_e) - h_p = \frac{1}{2}[\gamma_p + \lambda_p - \gamma_e - \lambda_e - ln(1 - \upsilon_e^2)]. \tag{5.2.8}$$

Again, equation 5.2.8 depends on the low density region properties. By dividing r_e with its initial value r_{e0}, we make the quantity $\frac{r_e^3}{r_{e0}^3}$ normalized and universal.

For the same reason R_e/R_* will be also universal, since

$$R_e/R_* = \frac{\bar{\mathrm{r}}_e e^{[\gamma_e - \lambda_e]/2}}{\bar{\mathrm{r}}_{e0} e^{[\gamma_{e0} - \lambda_{e0}]/2}}, \tag{5.2.9}$$

and the potentials don't really change until we get close to the Kepler frequency.

Finally, it makes sense to say that the quotient of two universal parameters will create another universal quantity. For this reason, MR_*/M_*R_e will be also universal.

Chapter 6

Conclusions

The study of rotating neutron stars is a fascinating but at the same time a very complicated part of physics. Our inability to find analytic solutions for the general relativistic equations makes the development of empirical approximations essential.

In this project, we have created sequences of rotating neutron stars with constant central energy density by the use of the RNS code. The two equation of state families that have been used for the creation of these sequences, were the speed of sound model and the piecewise polytropes.

Based on the outputs we were able to find a new approximation for the Kepler frequency which can describe the data with a deviation less than 1.60%. Moreover, we observed that along a sequence the compactness remains almost constant and drops for sequences with smaller central energy densities. Therefore, we concluded that the compactness of a neutron star is strongly related to the value of the central energy density. Furthermore, we developed empirical relations for the spin corrections for M/M_*, R_e/R_* and C_e, for given values of the normalized frequency Ω_n and the initial compactness C_* (the best fit equations are valid for $0.014 \leq C_* \leq 0.22$). The deviation from the data is less than 4.6%, 1.5% and 2.8% respectively for most of the frequencies.

The relatively small deviation of these three quantities yields the fact that the spin corrections are almost independent to the choice of the EOS and therefore universal. This has been double checked as our best fit relations can also describe the spin corrections to stars that have been created by the use of some other EOSs.

These best-fit equations can be used for a quick estimate of the mass and radius changes, instead of running the RNS code. Also, by the use of similar best-fit equations and for given M, R_e and Ω of a rotating NS, we can find mass and radius of the non-rotating NS with the same central energy density. This means that rotating NSs can provide us information for the M-R curve of the non-rotating NSs

Unfortunately, our telescopes can not directly measure the radius of a NS. The indirect methods for determining neutron star radii used today are not very precise. We expect that the next generation of X-ray telescopes with larger collecting areas will allow us to measure the radius of the rapidly rotating neutron stars precisely. The formulae developed in this thesis can then be used with the mass and radius measurements to infer the properties of equation of state of matter at high densities.

Bibliography

Abbott, B., Abbott, R., Abbott, T., et al. 2017, Physical Review Letters, 119, doi: 10.1103/physrevlett.119.161101

Abbott, B. P., Abbott, R., Abbott, T. D., et al. 2016, Phys. Rev. Lett., 116, 061102, doi: 10.1103/PhysRevLett.116.061102

Akmal, A., Pandharipande, V. R., & Ravenhall, D. G. 1998, Phys. Rev. C, 58, 1804, doi: 10.1103/PhysRevC.58.1804

Alcock, C., Farhi, E., & Olinto, A. 1986, ApJ, 310, 261, doi: 10.1086/164679

Alford, M., Braby, M., Paris, M., & Reddy, S. 2005, The Astrophysical Journal, 629, 969–978, doi: 10.1086/430902

Ambartsumyan, V. A., & Saakyan, G. S. 1960, Soviet Astronomy, 4, 187

Baade, W., & Zwicky, F. 1934, Proceedings of the National Academy of Science, 20, 254, doi: 10.1073/pnas.20.5.254

Baldo, M., Bombaci, I., & Burgio, G. F. 1997, AAP, 328, 274. https://arxiv.org/abs/astro-ph/9707277

Baym, G., & Pethick, C. 1991, Landau Fermi-Liquid Theory and Low Temperature Properties of Normal Liquid 3He (John Wiley Sons, Ltd), 1–121, doi: https://doi.org/10.1002/9783527617159.ch1

Baym, G., Pethick, C., & Sutherland, P. 1971, ApJ, 170, 299, doi: 10.1086/151216

Becker, W., Weisskopf, M. C., Tennant, A. F., et al. 2004, The Astrophysical Journal, 615, 908, doi: 10.1086/424498

Bedaque, P., & Steiner, A. W. 2015, Phys. Rev. Lett., 114, 031103, doi: 10.1103/PhysRevLett.114.031103

Bhattacharyya, S. 2021, Monthly Notices of the Royal Astronomical Society: Letters, 502, L45–L49, doi: 10.1093/mnrasl/slab001

Bogdanov, S. 2012, The Astrophysical Journal, 762, 96, doi: 10.1088/0004-637x/762/2/96

Bogdanov, S., Lamb, F. K., Mahmoodifar, S., et al. 2019, ApJL, 887, L26, doi: 10.3847/2041-8213/ab5968

Börner, G. 1978, Europhys. News, 9, 5, doi: 10.1051/epn/19780905005

Breu, C., & Rezzolla, L. 2016, MNRAS,, 459, 646, doi: 10.1093/mnras/stw575

Brown, E. F., & Bildsten, L. 1998, The Astrophysical Journal, 496, 915, doi: 10.1086/305419

Burgio, G. F., Baldo, M., Sahu, P. K., & Schulze, H.-J. 2002, Phys. Rev. C, 66, 025802, doi: 10.1103/PhysRevC.66.025802

Calderon Noguez, J. 2019, Effect of spin on mass and radius of neutron stars (University of Alberta), doi: https://doi.org/10.7939/r3-1vg8-9553

Cameron, A. G. 1959, ApJ, 130, 884, doi: 10.1086/146780

Chandrasekhar, S. 1969, Ellipsoidal figures of equilibrium (Yale University Press). https://books.google.ca/books?id=z4LBjgEACAAJ

Cook, G. B., Shapiro, S. L., & Teukolsky, S. A. 1992, ApJ, 398, 203, doi: 10.1086/171849

—. 1994, ApJ, 424, 823, doi: 10.1086/173934

Foglizzo, T., Kazeroni, R., Guilet, J., et al. 2015, Publications of the Astronomical Society of Australia, 32, e009, doi: 10.1017/pasa.2015.9

Fonseca, E., Cromartie, H. T., Pennucci, T. T., et al. 2021, ApJL, 915, L12, doi: 10.3847/2041-8213/ac03b8

Friedman, J. L., Ipser, J. R., & Parker, L. 1989, PRL, 62, 3015, doi: 10.1103/PhysRevLett.62.3015

Friedman, J. L., Ipser, J. R., & Sorkin, R. D. 1988, ApJ, 325, 722, doi: 10.1086/166043

Gendreau, K. C., Arzoumanian, Z., Adkins, P. W., et al. 2016, in Society of Photo-Optical Instrumentation Engineers (SPIE) Conference Series, Vol. 9905, Space Telescopes and Instrumentation 2016: Ultraviolet to Gamma Ray, ed. J.-W. A. den Herder, T. Takahashi, & M. Bautz, 99051H, doi: 10.1117/12.2231304

Giacconi, R., Gursky, H., Kellogg, E., Schreier, E., & Tananbaum, H. 1971, ApJL, 167, L67, doi: 10.1086/180762

Giacconi, R., Gursky, H., & Waters, J. R. 1964, Nature, 204, 981, doi: 10.1038/204981a0

Glendenning, N. 1997, Compact Stars (Springer, New York, NY), 288–290, doi: 10.1007/978-1-4684-0491-3_6

Gotthelf, E. V., Tomsick, J. A., Halpern, J. P., et al. 2014, ApJ, 788, 155, doi: 10.1088/0004-637X/788/2/155

Greif, S. K., Raaijmakers, G., Hebeler, K., Schwenk, A., & Watts, A. L. 2019, Monthly Notices of the Royal Astronomical Society, 485, 5363–5376, doi: 10.1093/mnras/stz654

Haensel, P., Potekhin, A. Y., & Yakovlev, D. G. 2007, Neutron stars 1: Equation of state and structure, Vol. 326 (New York, USA: Springer), 1–8 and 34–40, doi: 10.1007/978-0-387-47301-7

Harrison, F. A., Craig, W. W., Christensen, F. E., et al. 2013, The Astrophysical Journal, 770, 103, doi: 10.1088/0004-637x/770/2/103

Hebeler, K., Lattimer, J. M., Pethick, C. J., & Schwenk, A. 2013, ApJ, 773, 11, doi: 10.1088/0004-637X/773/1/11

Heinke, C. O., Cohn, H. N., Lugger, P. M., et al. 2014, Monthly Notices of the Royal Astronomical Society, 444, 443, doi: 10.1093/mnras/stu1449

Hessels, J. W. T., Ransom, S. M., Stairs, I. H., et al. 2006, Science, 311, 1901, doi: 10.1126/science.1123430

Horvath, J. E., Rocha, L. S., Bernardo, A. L. C., de Avellar, M. G. B., & Valentim, R. 2020, Birth events, masses and the maximum mass of Compact Stars. https://arxiv.org/abs/2011.08157

Hulse, R. A., & Taylor, J. H. 1975, APJL, 195, L51, doi: 10.1086/181708

Janka, H.-T. 2017, in Handbook of Supernovae (Springer International Publishing), 1575–1604, doi: 10.1007/978-3-319-21846-5_4

Jansen, F., Lumb, D., Altieri, B., et al. 2001, AAP, 365, L1, doi: 10.1051/0004-6361:20000036

J.E Ventura, D. P. 1991, Neutron Stars: Theory and Observation, Vol. 344 (Springer Netherlands), 245–247, doi: 10.1007/978-94-011-3536-8

Kaplan, J. D., Ott, C. D., O'Connor, E. P., et al. 2014, ApJ, 790, 19, doi: 10.1088/0004-637X/790/1/19

Kojo, T., Baym, G., & Hatsuda, T. 2021. https://arxiv.org/abs/2111.11919

Komatsu, H., Eriguchi, Y., & Hachisu, I. 1989, MNRAS, 237, 355, doi: 10.1093/mnras/237.2.355

Kutschera, M. 1998, Neutron stars: formation and structure

Lasota, J.-P., Haensel, P., & Abramowicz, M. A. 1996, ApJ, 456, 300, doi: 10.1086/176650

Lattimer, J. M., & Prakash, M. 2001, ApJ, 550, 426, doi: 10.1086/319702

Lorenz, C. P., Ravenhall, D. G., & Pethick, C. J. 1993, Phys. Rev. Lett., 70, 379, doi: 10.1103/PhysRevLett.70.379

Marsh, T. R., Gänsicke, B. T., Hümmerich, S., et al. 2016, Nature, 537, 374, doi: 10.1038/nature18620

Miller, M. C., Chirenti, C., & Lamb, F. K. 2020, ApJ, 888, 12, doi: 10.3847/1538-4357/ab4ef9

Miller, M. C., Lamb, F. K., Dittmann, A. J., et al. 2019, The Astrophysical Journal, 887, L24, doi: 10.3847/2041-8213/ab50c5

Morrison, I. A., Baumgarte, T. W., Shapiro, S. L., & Pandharipande, V. R. 2004, The Astrophysical Journal, 617, L135, doi: 10.1086/427235

Morsink, S. M., Leahy, D. A., Cadeau, C., & Braga, J. 2007, ApJ, 663, 1244, doi: 10.1086/518648

Negele, J. W., & Vautherin, D. 1973, Nuclear Physics A, 207, 298, doi: 10.1016/0375-9474(73)90349-7

Nelson, L. A., & Rappaport, S. 2003, ApJ, 598, 431, doi: 10.1086/378798

Oppenheimer, J. R., & Volkoff, G. M. 1939, Phys. Rev., 55, 374, doi: 10.1103/PhysRev.55.374

Pandharipande, V., & Smith, R. 1975, Nuclear Physics A, 237, 507, doi: https://doi.org/10.1016/0375-9474(75)90415-7

Pechenick, K. R., Ftaclas, C., & Cohen, J. M. 1983, ApJ, 274, 846, doi: 10.1086/161498

Potekhin, A. Y. 2010, Physics-Uspekhi, 53, 1235–1256, doi: 10.3367/ufne.0180.201012c.1279

Prakash, M., Lattimer, J., Pons, J., Steiner, A., & Reddy, S. 2000, 1–5

Ravenhall, D. G., & Pethick, C. J. 1994, ApJ, 424, 846, doi: 10.1086/173935

Ray, P. S., Arzoumanian, Z., Ballantyne, D., et al. 2019, arXiv e-prints, arXiv:1903.03035. https://arxiv.org/abs/1903.03035

Read, J. S., Lackey, B. D., Owen, B. J., & Friedman, J. L. 2009, Physical Review D, 79, doi: 10.1103/physrevd.79.124032

Rhoades, C. E., & Ruffini, R. 1974, PRL, 32, 324, doi: 10.1103/PhysRevLett.32.324

Riley, T. E., Watts, A. L., Bogdanov, S., et al. 2019, ApJL, 887, L21, doi: 10.3847/2041-8213/ab481c

Riley, T. E., Watts, A. L., Bogdanov, S., et al. 2019, The Astrophysical Journal, 887, L21, doi: 10.3847/2041-8213/ab481c

Santangelo, A., del Sordo, S., Segreto, A., et al. 1998, AAP, 340, L55

Schutz, B. 2009, A First Course in General Relativity, 2nd edn. (Cambridge University Press), 100–104 and 258–266, doi: 10.1017/CBO9780511984181

Schwenk, A., Friman, B., & Brown, G. E. 2003, Nuclear Physics A, 713, 191, doi: https://doi.org/10.1016/S0375-9474(02)01290-3

Shaw, A. W., Heinke, C. O., Steiner, A. W., et al. 2018, MNRAS, 476, 4713, doi: 10.1093/mnras/sty582

Stergioulas, N., & Friedman, J. L. 1995, ApJ, 444, 306, doi: 10.1086/175605

Taylor, J. H., Fowler, L. A., & McCulloch, P. M. 1979, NATURE, 277, 437, doi: 10.1038/277437a0

Tsuji, N., Uchiyama, Y., Aharonian, F., et al. 2019, The Astrophysical Journal, 877, 96, doi: 10.3847/1538-4357/ab1b29

Vidaña, I. 2016, Journal of Physics: Conference Series, 668, 012031, doi: 10.1088/1742-6596/668/1/012031

Weisskopf, M. C., Tananbaum, H. D., Speybroeck, L. P. V., & O'Dell, S. L. 2000, in SPIE Proceedings, ed. J. E. Truemper & B. Aschenbach (SPIE), doi: 10.1117/12.391545

Witten, E. 1984, Phys. Rev. D, 30, 272, doi: 10.1103/PhysRevD.30.272

Yagi, K., & Yunes, N. 2013, Science, 341, 365, doi: 10.1126/science.1236462

Zavlin, V. E., & Pavlov, G. G. 2002, doi: 10.48550/ARXIV.ASTRO-PH/0206025

Zdunik, J. L., & Haensel, P. 2013, Astronomy &amp Astrophysics, 551, A61, doi: 10.1051/0004-6361/201220697

Zeldovich. 1961, Journal of Experimental and Theoretical Physics, 41, 1609

Özel, F., & Freire, P. 2016, Annual Review of Astronomy and Astrophysics, 54, 429, doi: 10.1146/annurev-astro-081915-023322

Appendix A

Tables

TABLE A.0.1: PP EOS properties

Polytropes					
EOS	ϵ_c **for** M_{max} $(10^{15}$ **g/c**$m^3)$	M_{max} $(\mathbf{M}\odot)$	**Radius for** M_{max}**(km)**	ϵ_c **for** $R_{1.4}$ $(10^{15}$ **g/c**$m^3)$	$R_{1.4}(km)$
EOS PP0	2.05954	2.4177	11.6194	0.645	13.14462
EOS PP1	2.74468	2.08675	10.2294	0.935	11.97620
EOS PP2	2.06436	2.20625	11.6892	0.75	12.66363
EOS PP3	2.66948	2.13168	10.3705	0.905	12.07525
EOS PP4	1.79879	2.54859	12.4515	0.548	13.68696
EOS PP5	2.26074	2.38	11.1862	0.72	12.79479
EOS PP6	1.75407	2.6027	12.6202	0.475	14.41601
EOS PP7	2.72281	1.98615	10.3285	0.97	11.91771
EOS PP8	1.36081	2.87851	14.2703	0.464	14.24289
EOS PP9	2.90151	1.98231	10.1331	1.047	11.62949
EOS PP10	1.83953	2.12658	12.2014	0.7205	12.78293
EOS PP11	2.13547	2.05594	11.3234	0.9363	11.58549
EOS PP12	2.53598	2.14666	10.4004	0.8595	11.34843
EOS PP13	2.40429	2.17098	10.5372	0.8345	11.21152
EOS PP14	2.52533	2.17843	10.2705	0.989	10.91808
EOS PP15	1.31001	2.77458	14.2351	0.4655	14.22713
EOS PP16	1.4324	2.86801	13.7366	0.4098	14.66706
EOS PP17	1.55035	2.70123	13.216	0.518	13.86354
EOS PP18	1.51305	2.27518	13.1886	0.583	13.47389

Information for Polytropes								
EOS	**log(P_0) log(dyne/cm^2)**	**ρ_0(g/cm^3)**	**Γ_1**	**Γ_2**	**Γ_3**	**ρ_1(g/cm^3)**	**ρ_2(g/cm^3)**	**Crust EOS**
EOS PP0	32.9354	1.5548e+14	3.30516	2.81827	2.50487	7.22702e+14	1.39021e+15	eosNV
EOS PP1	32.9354	1.5548e+14	2.93164	3.10635	2.5707	1.47686e+15	1.50893e+15	eosNV
EOS PP2	32.9354	1.5548e+14	3.13074	3.04963	1.14979	8.19238e+14	1.13188e+15	eosNV
EOS PP3	32.9354	1.5548e+14	2.95725	2.98906	2.04683	8.67388e+14	1.66012e+15	eosNV
EOS PP4	32.9354	1.5548e+14	3.54898	2.71203	1.64651	5.96421e+14	1.19792e+15	eosNV
EOS PP5	32.9354	1.5548e+14	3.17501	2.03076	2.5902	1.29921e+15	1.33942e+15	eosNV
EOS PP6	32.9354	1.5548e+14	4.06053	2.81974	2.7824	3.50711e+14	1.14831e+15	eosNV
EOS PP7	32.9354	1.5548e+14	2.92319	2.75347	1.79942	6.5451e+14	1.61116e+15	eosNV
EOS PP8	32.9354	1.5548e+14	3.87465	1.86897	0.517175	6.80115e+14	8.05338e+14	eosNV
EOS PP9	32.9354	1.5548e+14	2.84787	3.18683	1.06003	1.41965e+15	1.71782e+15	eosNV
EOS PP10	32.9354	1.5548e+14	3.17075	2.44494	0.696782	9.43276e+14	9.97547e+14	eosNV
EOS PP11	32.9354	1.5548e+14	2.78092	4.23643	0.511191	6.82396e+14	1.08212e+15	eosNV
EOS PP12	32.9354	1.5548e+14	2.31192	5.01666	2.59543	5.0226e+14	7.9526e+14	eosNV
EOS PP13	32.9354	1.5548e+14	1.97068	5.58393	2.50977	4.71362e+14	7.8891e+14	eosNV
EOS PP14	32.9354	1.5548e+14	2.19965	4.43449	2.52436	5.05475e+14	1.04488e+15	eosNV
EOS PP15	32.9354	1.5548e+14	3.86494	3.49939	0.991998	5.47209e+14	6.95931e+14	eosNV
EOS PP16	32.9354	1.5548e+14	4.20408	3.03407	2.61427	3.8685e+14	6.75015e+14	eosNV
EOS PP17	32.9354	1.5548e+14	3.64449	1.94988	2.01376	7.43387e+14	9.06511e+14	eosNV
EOS PP18	32.9354	1.5548e+14	3.4467	2.02142	0.647275	7.08159e+14	8.73534e+14	eosNV

TABLE A.0.2: PP EOS parameters

TABLE A.0.3: c_s EOS properties

Greif's Prescription					
EOS	ϵ_c **for** M_{max} $(10^{15}$ **g/c**$m^3)$	M_{max} **(M**$\odot$**)**	**Radius for** M_{max}**(km)**	ϵ_c **for** $R_{1.4}$ $(10^{15}$ **g/c**$m^3)$	$R_{1.4}(km)$
EOS c_s0	2.92396	2.0529	9.95608	1.015	11.90245
EOS c_s1	1.93827	2.52407	11.6122	0.674	12.49347
EOS c_s2	2.80474	2.08229	10.0054	1.011	11.42718
EOS c_s3	2.41673	2.15847	10.8271	0.82	12.41309
EOS c_s4	2.9148	2.01246	9.88853	1.15	11.33979
EOS c_s5	2.24358	2.21145	11.1881	0.766	12.58356
EOS c_s6	2.57415	2.11412	10.5363	0.864	12.30228
EOS c_s7	1.84654	2.29408	12.0885	0.688	12.78610
EOS c_s8	2.89235	1.98973	9.86927	1.046	11.34445
EOS c_s9	2.47182	1.97957	10.525	1.01	11.24795
EOS c_s10	2.25932	2.27669	11.1269	0.751	12.63494
EOS c_s11	1.6483	2.01099	12.2521	0.651	12.56330
EOS c_s12	2.62952	1.98693	10.0718	1.2	10.25369

TABLE A.0.4: c_s EOS parameters

c_s **EOS Information**								
EOS	**a1**	**a2**	**a3**	**a4**	**a5**	**a6**	**cEFT**	**Crust**
EOS c_s0	1.13326	3.64489	4.84797	5.71515	0.898815	-0.957613	stiff	eosBPS
EOS c_s1	0.80546	4.50618	5.49548	1.91	0.612625	-1.22891	soft	eosBPS
EOS c_s2	1.07202	3.76314	4.58081	5.47436	0.765409	-0.918366	soft	eosBPS
EOS c_s3	1.11525	6.22776	4.28874	12.6135	0.280804	-0.529332	stiff	eosBPS
EOS c_s4	0.536138	7.11362	2.21716	3.12908	0.854708	-0.0144199	stiff	eosBPS
EOS c_s5	0.822325	4.81481	3.22364	6.50179	0.357524	-0.477352	stiff	eosBPS
EOS c_s6	1.04286	3.75254	4.45693	5.61644	0.639041	-0.888979	stiff	eosBPS
EOS c_s7	0.342192	3.34504	1.05392	1.78417	0.957062	-0.152893	stiff	eosBPS
EOS c_s8	1.41118	8.01655	6.34569	13.6166	0.404173	-0.756376	soft	eosBPS
EOS c_s9	0.561042	4.61444	1.70654	6.66794	0.863001	-0.0398646	soft	eosBPS
EOS c_s10	1.41302	6.19101	4.31591	11.4886	0.67495	-0.657166	stiff	eosBPS
EOS c_s11	0.379026	2.37536	0.722132	3.10699	0.788866	-0.130962	soft	eosBPS
EOS c_s12	0.83241	4.90886	0.976381	1.96747	0.18004	-0.227635	soft	eosBPS

TABLE A.0.5: Parameter values from our best fit equations

Ω_n	C_*	M/M_*	M/M_* error (%)	R_e/R_*	R_e/R_* error (%)	C_e	C_e error (%)
0.05644	0.007692	1.0	0.00098	1.001	0.0015	0.007692	0.0011
0.1693	0.007692	1.0	0.038	1.005	0.16	0.007687	0.38
0.5079	0.007692	1.002	0.46	1.049	0.95	0.007546	2.5
0.8465	0.007692	1.008	1.6	1.169	1.4	0.006832	3.1
0.9594	0.007692	1.012	2.1	1.295	7.2	0.006152	1e+01
0.05644	0.05303	1.0	0.0005	1.001	0.00081	0.05303	0.00079
0.1693	0.05303	1.003	0.24	1.005	0.086	0.05301	0.069
0.5079	0.05303	1.033	1.4	1.046	0.29	0.05259	1.0
0.8465	0.05303	1.121	3.0	1.16	0.77	0.05047	4.1
0.9594	0.05303	1.178	3.7	1.278	5.5	0.04845	9.6
0.05644	0.1097	1.0	0.00081	1.001	0.00085	0.1097	0.00085
0.1693	0.1097	1.004	0.13	1.005	0.11	0.1097	0.1
0.5079	0.1097	1.044	0.79	1.046	0.35	0.1094	0.93
0.8465	0.1097	1.162	2.5	1.159	0.9	0.1079	3.1
0.9594	0.1097	1.238	3.4	1.277	3.2	0.1064	9.4
0.05644	0.155	1.0	0.0011	1.0	0.00087	0.155	0.00079
0.1693	0.155	1.004	0.14	1.004	0.077	0.155	0.13
0.5079	0.155	1.04	0.8	1.039	0.33	0.1547	0.99
0.8465	0.155	1.149	2.1	1.136	1.2	0.1533	3.3
0.9594	0.155	1.219	3.6	1.237	3.2	0.1519	7.9
0.05644	0.2117	1.0	0.034	1.0	0.011	0.2117	0.023
0.1693	0.2117	1.003	0.13	1.003	0.064	0.2117	0.13
0.5079	0.2117	1.032	0.4	1.028	0.48	0.2115	0.73
0.8465	0.2117	1.117	0.74	1.095	1.5	0.2106	1.9
0.9594	0.2117	1.172	1.6	1.166	2.5	0.2098	5.1

TABLE A.0.6: A summary of our best fit equations

Equation's name	Equations with Ω, R_*, M_* and C_* as free parameters
Equation 1	$\Omega_K(empirical) \approx \sqrt{\frac{GM_*}{R_*^3}} \times(a_1C_*^4 + a_2C_*^3 + a_3C_*^2 + a_4C_* + a_5)$
Equation 2	$\mathrm{M/M_*} \approx 1 + (e^{a_0\Omega_n^2} - 1) \times (a_1 + a_2C_* + a_3C_*^2 + a_4C_*^3 + a_5C_*^4)$
Equation 3	$\mathrm{M/M_*}\big\vert_K \approx a_1C_*^3 + a_2C_*^2 + a_3C_* + a_4$
Equation 4	$\mathrm{R_e/R_*} \approx 1 + (e^{a_1\Omega_n^2} - 1 - a_2[ln(1 - (\frac{\Omega_n}{1.1})^4)]^2) \times(1 + a_3C_* + a_4C_*^2 + a_5C_*^3 + a_6C_*^4 + a_7C_*^5)$
Equation 5	$\mathrm{R/R_*}\big\vert_K \approx a_1C_*^5 + a_2C_*^4 + a_3C_*^3 + a_4C_*^2 + a_5C_* + a_6$
Equation 6	$\mathrm{C_e} \approx C_* + ln(1 - (\frac{\Omega_n}{1.1})^3) \times (a_1C_* + a_2C_*^2 + a_3C_*^3 + a_4C_*^4)$
Equation 7	$\mathrm{R}_{ratio} = 1 + (a_1\Omega_n^2 + a_2ln(1 - (\Omega_n/1.1)^2)) \times (1 + a_3C_* + a_4C_*^2)$
Equation 8	$\mathrm{R}_{ratio}\_S = 1 + (a_1\Omega_n^2 + a_2ln(1 - (\Omega_n/1.1)^2)) \times (1 + a_3C_* + a_4C_*^2)$
Equation's name	Equations with Ω, R_e, M and C_e as free parameters
Equation 9	$\Omega_K(empirical) \approx \sqrt{\frac{GM}{R_e^3}} \times(a_1C_e^4 + a_2C_e^3 + a_3C_e^2 + a_4C_e + a_5)$
Equation 10	$\mathrm{M/M_*} \approx 1 + (\Omega_{n2} + a_1\Omega_{n2}^2 + a_2\Omega_{n2}^3 + a_3\Omega_{n2}^4) \times (a_4C_e + a_5C_e^2 + a_6C_e^3 + a_7C_e^4)$
Equation 11	$\mathrm{R_e/R_*} \approx 1 + (e^{a_1\Omega_{n2}^2} - 1 - a_2[ln(1 - (\frac{\Omega_{n2}}{1.1})^4)]^2) \times(1 + a_3C_e + a_4C_e^2 + a_5C_e^3 + a_6C_e^4 + a_7C_e^5)$

(*) Ω_n is the frequency Ω divided by the Ω_K that comes from the Equation 1.
(**) Ω_{n2} is the frequency Ω divided by the Ω_K that comes from the Equation 9.

TABLE A.0.7: The coefficients of our best fit equations

Equation's name	a_1	a_2	a_3	a_4	a_5	a_6	a_7	R^2
Equation 1	-326.48	180.61	-35.211	3.304	0.552	-	-	0.9895
Equation 2	1.127	-0.0160	3.123	-20.721	41.202	-6.464	-	0.9808
Equation 3	71.388	-39.568	6.271	0.9662	-	-	-	0.8698
Equation 4	0.203	-0.1611	-15.496	442.60	-4945.62	23458.06	-40544.25	0.9939
Equation 5	-6706.60	4228.02	-983.53	97.212	-4.145	1.479	-	0.9820
Equation 6	0.209	-3.449	21.215	-44.427	-	-	-	0.9986
Equation 7	-0.134	0.0778	8.054	-27.495	-	-	-	0.9962
Equation 8	-0.137	0.0771	6.481	-28.830	-	-	-	0.9950
Equation 9	79.377	-17.907	-2.328	0.4183	0.9933	-	-	0.9121
Equation 10	-2.924	15.305	-9.908	1.765	-10.985	11.069	34.996	0.9722
Equation 11	0.39998	0.0058314	-8.8981	216.845	-2298.43	10211.98	-16587.60	0.9980

Appendix B

Additional plots

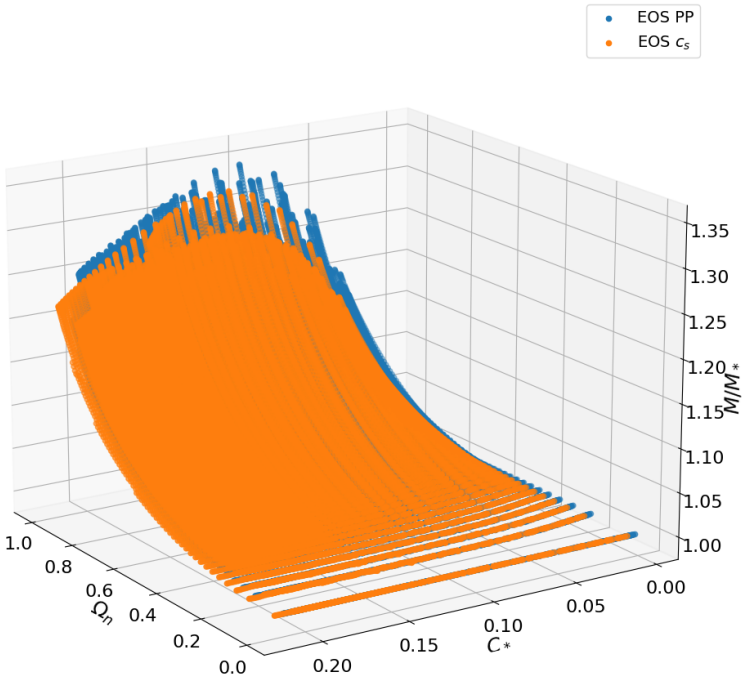

FIGURE B.0.1: M/M_* vs C_* vs Ω_n

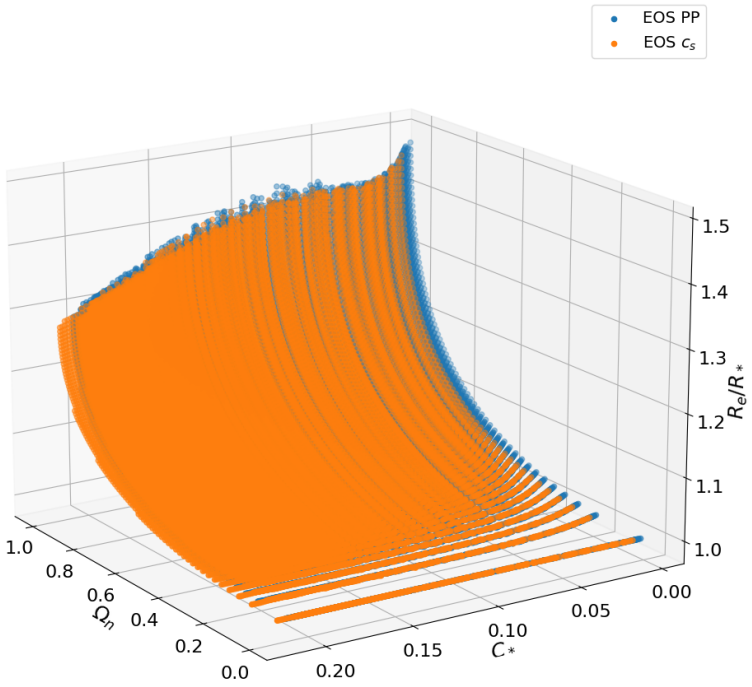

FIGURE B.0.2: R_e/R_* vs C_* vs Ω_n

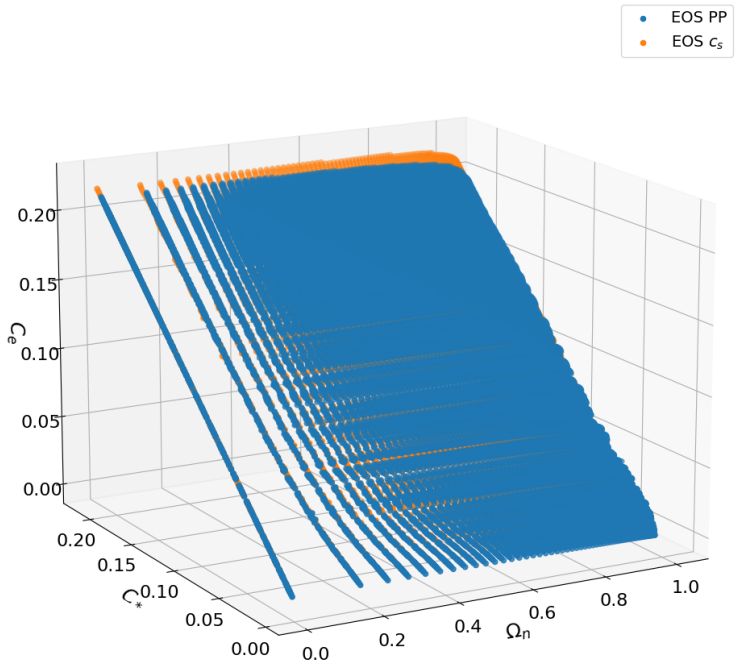

FIGURE B.0.3: C_e vs C_* vs Ω_n for all EOS

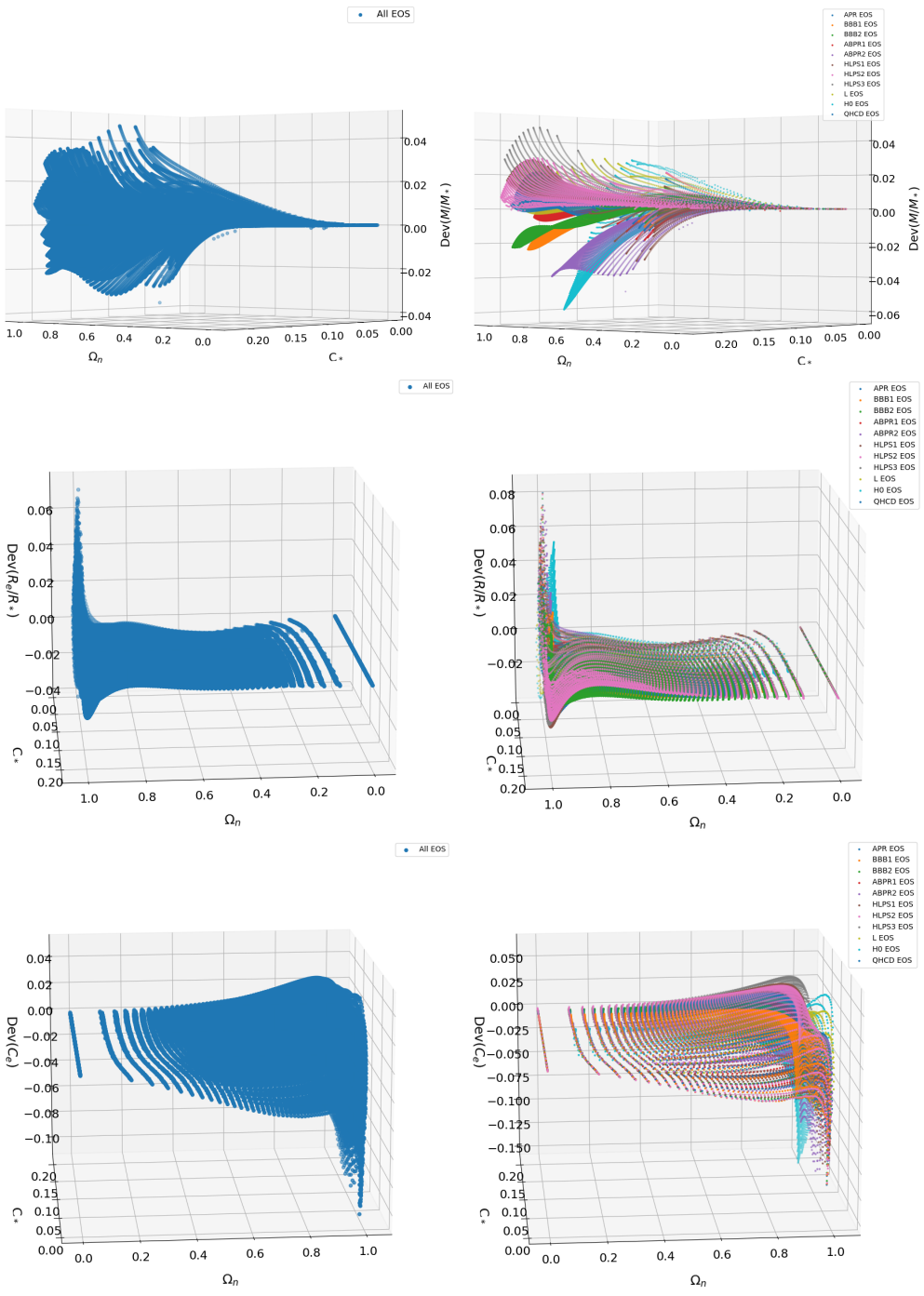

FIGURE B.0.4: M/M_*, R_e/R_* and C_e deviation of our data (left) and the other hadronic and hybrid EOSs (right) from our best fit surfaces

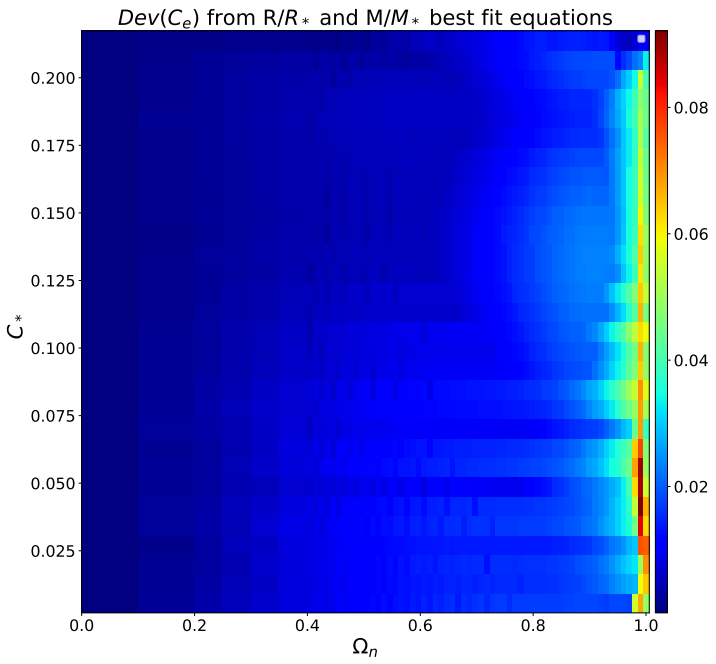

FIGURE B.0.5: Compactness Deviation by using M/M_* and R_e/R_* best fit equations. Each bin represents the maximum value of the divergence inside it.